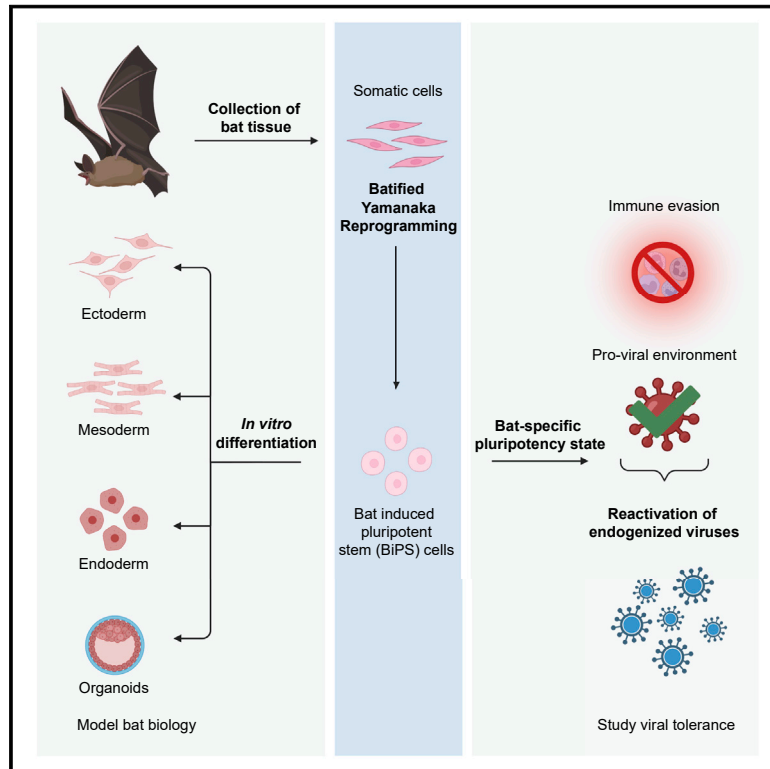


# Bat pluripotent stem cells reveal unusual entanglement between host and viruses

## Graphical abstract



## Authors

Marion Déjosez, Arturo Marin, Graham M. Hughes, ..., Emma C. Teeling, Adolfo García-Sastre, Thomas P. Zwaka

## Correspondence

emma.teeling@ucd.ie (E.C.T.),  
adolfo.garcia-sastre@mssm.edu (A.G.-S.),  
thomas.zwaka@mssm.edu (T.P.Z.)

## In brief

Generation of induced pluripotent stem cells from two diverse bat species opens the door to functional studies of bat cell biology, including the question of why they are distinctively able to harbor viruses of importance to human health.

## Highlights

- Understanding of bat biology has been limited by lack of cellular models
- Induced pluripotent stem cells are produced from two evolutionarily distant bat species
- The core pluripotency expression profile resembles that of cells attacked by viruses
- Bat stem cells accommodate a substantial load of endogenous viral sequences

Article

# Bat pluripotent stem cells reveal unusual entanglement between host and viruses

Marion Déjosez,<sup>1,2,3</sup> Arturo Marin,<sup>4,5,21</sup> Graham M. Hughes,<sup>6,21</sup> Ariadna E. Morales,<sup>8,9,21</sup> Carlos Godoy-Parejo,<sup>1,2</sup> Jonathan L. Gray,<sup>1,2</sup> Yiren Qin,<sup>1,2</sup> Arun A. Singh,<sup>1,2</sup> Hui Xu,<sup>1,2</sup> Javier Juste,<sup>10,11</sup> Carlos Ibáñez,<sup>10</sup> Kris M. White,<sup>4,5</sup> Romel Rosales,<sup>4,5</sup> Nancy J. Francoeur,<sup>12</sup> Robert P. Sebra,<sup>13,14</sup> Dominic Alcock,<sup>6</sup> Thomas L. Volkert,<sup>3</sup> Sébastien J. Puechmaile,<sup>15</sup> Andrzej Pastusiak,<sup>16</sup> Simon D.W. Frost,<sup>16,17</sup> Michael Hiller,<sup>7,8,9</sup> Richard A. Young,<sup>18</sup> Emma C. Teeling,<sup>6,\*</sup> Adolfo García-Sastre,<sup>4,5,19,20,\*</sup> and Thomas P. Zwaka<sup>1,2,3,22,\*</sup>

<sup>1</sup>Huffington Center for Cell-Based Research in Parkinson's disease, Icahn School of Medicine at Mount Sinai, New York, NY 10502, USA

<sup>2</sup>Department of Cell, Developmental, and Regenerative Biology, and Black Family Stem Cell Institute, Icahn School of Medicine at Mount Sinai, New York, NY 10502, USA

<sup>3</sup>Paratus Sciences, 430 East 29th Street, Suite 600, New York, NY 10016, USA

<sup>4</sup>Department of Microbiology, Icahn School of Medicine at Mount Sinai, New York, NY, USA

<sup>5</sup>Global Health and Emerging Pathogens Institute, Icahn School of Medicine at Mount Sinai, New York, NY 10029, USA

<sup>6</sup>School of Biology and Environmental Science, University College Dublin, Ireland

<sup>7</sup>LOEWE Centre for Translational Biodiversity Genomics, Senckenberganlage 25, 60325 Frankfurt, Germany

<sup>8</sup>Senckenberg Research Institute, Senckenberganlage 25, 60325 Frankfurt, Germany

<sup>9</sup>Faculty of Biosciences, Goethe University, Max-von-Laue-Str, 60438 Frankfurt, Germany

<sup>10</sup>Estación biológica de doñana (CSIC), Avda. Américo Vespucio 26, Seville 41092, Spain

<sup>11</sup>CIBER Epidemiology and Public Health, CIBERESP, Madrid, Spain

<sup>12</sup>Pacific Biosciences, Menlo Park, CA, USA

<sup>13</sup>Department of Genetics and Genomic Sciences, Icahn School of Medicine at Mount Sinai, New York, NY, USA

<sup>14</sup>Icahn Institute for Genomics, New York, NY, USA

<sup>15</sup>SEM, University of Montpellier, Montpellier, France

<sup>16</sup>Microsoft Premonition, Microsoft Building 99, 14820 NE 36th Street, Redmond, WA 98052, USA

<sup>17</sup>Department of Infectious Disease Epidemiology, London School of Hygiene and Tropical Medicine, Keppel Street, London WC1E 7HT, UK

<sup>18</sup>Whitehead Institute for Biomedical Research, Department of Biology, Massachusetts Institute of Technology, Cambridge, MA 02142, USA

<sup>19</sup>The Tisch Cancer Institute, Icahn School of Medicine at Mount Sinai, New York, NY 10029, USA

<sup>20</sup>Department of Pathology, Molecular and Cell-Based Medicine and the Department of Medicine, Division of Infectious Diseases, Icahn School of Medicine at Mount Sinai, New York, NY 10029, USA

<sup>21</sup>These authors contributed equally

<sup>22</sup>Lead contact

\*Correspondence: [emma.teeling@ucd.ie](mailto:emma.teeling@ucd.ie) (E.C.T.), [adolfo.garcia-sastre@mssm.edu](mailto:adolfo.garcia-sastre@mssm.edu) (A.G.-S.), [thomas.zwaka@mssm.edu](mailto:thomas.zwaka@mssm.edu) (T.P.Z.)

<https://doi.org/10.1016/j.cell.2023.01.011>

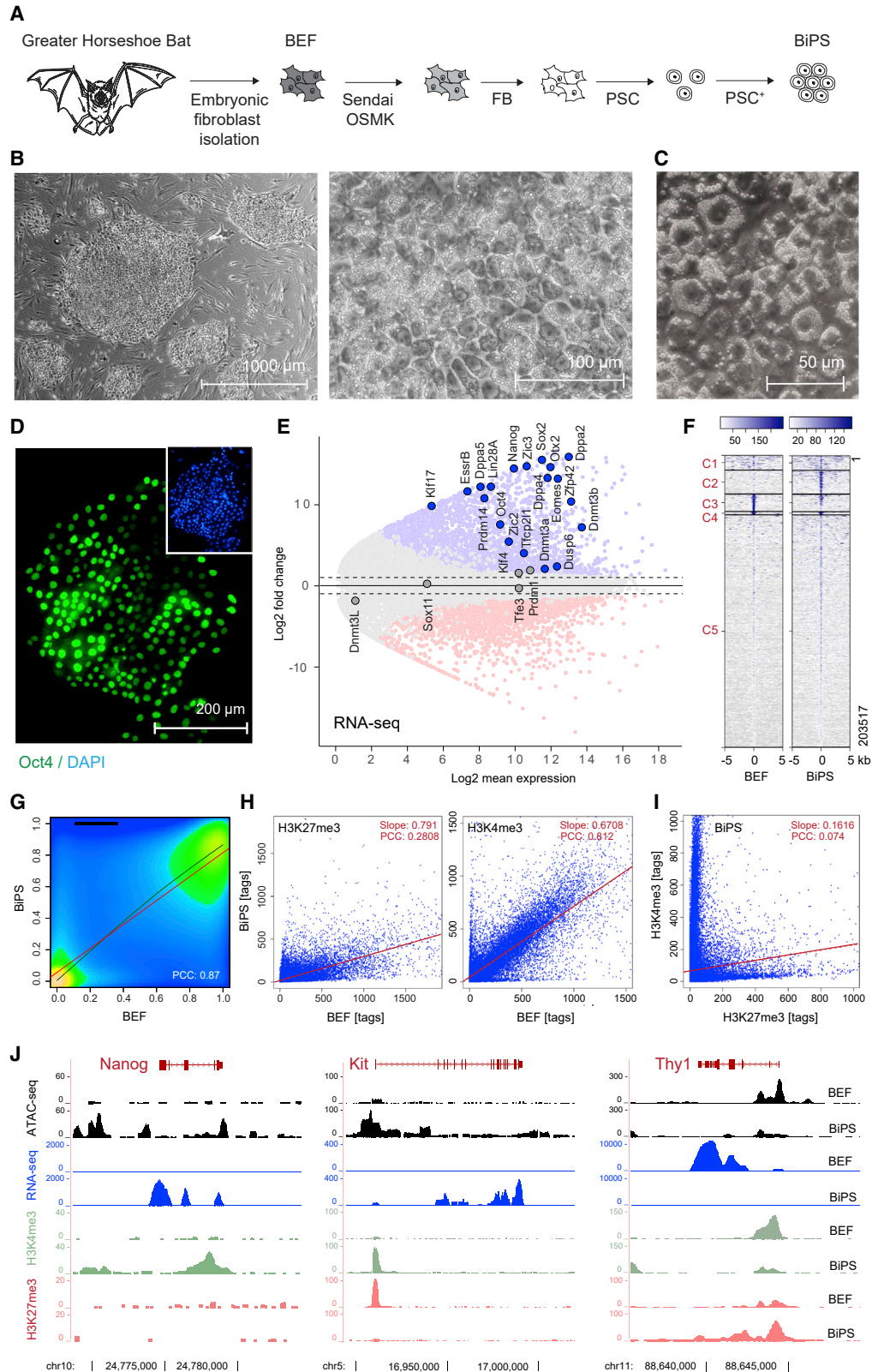
## SUMMARY

Bats are distinctive among mammals due to their ability to fly, use laryngeal echolocation, and tolerate viruses. However, there are currently no reliable cellular models for studying bat biology or their response to viral infections. Here, we created induced pluripotent stem cells (iPSCs) from two species of bats: the wild greater horseshoe bat (*Rhinolophus ferrumequinum*) and the greater mouse-eared bat (*Myotis myotis*). The iPSCs from both bat species showed similar characteristics and had a gene expression profile resembling that of cells attacked by viruses. They also had a high number of endogenous viral sequences, particularly retroviruses. These results suggest that bats have evolved mechanisms to tolerate a large load of viral sequences and may have a more intertwined relationship with viruses than previously thought. Further study of bat iPSCs and their differentiated progeny will provide insights into bat biology, virus host relationships, and the molecular basis of bats' special traits.

## INTRODUCTION

It has been an age-old question: what makes bats so fascinating to humans? Bats account for one-fifth of all living mammalian species ( $n = 1,456$ ),<sup>1</sup> inhabiting diverse ecological niches, feeding on arthropods, fruit, nectar, leaves, fish, blood, and small

vertebrates.<sup>2–5</sup> They are the only mammals to have evolved true, self-powered flight and can use laryngeal echolocation to orient in complete darkness.<sup>4,6</sup> They are found throughout the globe, absent only from extreme polar regions.<sup>4,6,7</sup> Many bat species studied exhibit an extremely long lifespan relative to body size and a suspected low tumorigenesis rate.<sup>8,9</sup> Still, what makes



(legend on next page)

bats most distinctive is that many species (e.g., rhinolophids, hipposiderids, pteropodids) have been shown to tolerate and survive many viruses that have high mortality rates in humans,<sup>10–12</sup> such as SARS-CoV, SARS-CoV-2, MERS-CoV, Marburg, and henipaviruses.<sup>12–18</sup> This is potentially due to a modulation of their innate immune response rendering them as asymptomatic and tolerant viral hosts.<sup>19–22</sup> Also, despite being among the smallest mammalian genomes, bat genomes contain the highest diversity of ancient and contemporary viral insertions of retroviral and non-retroviral origin,<sup>23–27</sup> suggesting that bats have a long and tolerant evolutionary history with their viral pathogens. As some of the integrated retroviral sequences are full length and even of non-bat origin, sequencing bat genomes provides insights into the bat virosphere and the potential for zoonotic spillover,<sup>15,28–30</sup> but also uncovers mechanisms of viral persistence.<sup>26</sup> To date, how bats deal with viruses is still poorly understood, with only a limited number of immune cells documented and characterized in a few bat species (e.g., *Pteropus alecto*, *Eonycteris spelaea*, *Myotis lucifugus*, *Eptesicus fuscus*).<sup>31–33</sup> Further, developing cellular resources and assays is required to uncover and validate the molecular adaptations that have evolved in bats to tolerate these viral pathogens.<sup>25,31–33</sup> The prevailing hypothesis supported by recent comparative genomic analyses of multiple bat families<sup>34</sup> is that viral tolerance results from specific adaptations of their innate immune system. Accordingly, bats mount an inaugural antiviral reaction after viral inoculation—like all mammals—but then quickly “dampen” this very response before it becomes overly pathological.<sup>25,35,36</sup> Critically, this unusual way to deal with viruses could be caused in part by molecular adaptations that stifle canonical virus sensing and the subsequent inflammatory response,<sup>18,19,37,38</sup> such as the cGAS-STING, OAS-RNASE L, and NLRP3 systems.<sup>39–43</sup>

It is striking how closely the aforementioned genomic adaptations to the bat immune system mirror how viruses themselves typically dismantle the host response.<sup>44</sup> Yet, viruses do not just use countermeasures against detection and quench inflammation. Viruses are also infinite masters of tweaking cell processes to their advantage to convert host cells into virus-producing fac-

ories. Hence, we wondered whether, in addition to the immune evasion strategies of viruses, bats also harbor the blueprints for productive viral replication, given the evolutionary maintenance of many intact and full-length viral elements in one of the smallest mammalian genomes and the potential evolutionary advantage gained from such a symbiosis.<sup>45,46</sup>

Here, we sought to test empirically the idea that bats genetically simulate the viral ploy for immune evasion and promote notably fertile ground for virus production. We conjectured that pluripotent stem cells would be an ideal experimental system for addressing this question. Given that pluripotent stem cells are the founding cells of the entire embryo, their cellular ground state provides an exclusive reference point for comparative studies, as all mammals must complete this stage in a similar manner.<sup>47</sup> Importantly, the global epigenetic resetting that occurs as cells reprogram to pluripotency causes the transcriptional reactivation of endogenous viruses.<sup>48–51</sup> As such, it would present a distinctive window into the abundant endogenized viral diversity within bat genomes, allowing the broad cataloging of active viruses and, in turn, the study of how viruses interface with host cell programs.

## RESULTS

### Bat Yamanaka reprogramming

Given the importance of bats as an emerging model system in multiple areas and the need to study their special biology and potential role in pandemics, we sought to develop an effective strategy to produce bat pluripotent stem cells (Figure 1A). Despite numerous attempts by different groups,<sup>36,52</sup> and some initial success in partial reprogramming,<sup>53</sup> robust pluripotent stem cell lines from bat species with globally repeatable protocols have not been previously reported.

We first focused on the original Yamanaka reprogramming paradigm, based on four reprogramming factors (Oct4, Sox2, Klf4, and cMyc), because it provides the most direct way to generate pluripotent stem cells in most species.<sup>54</sup> As a starting point, we used bat embryonic fibroblast (BEF) cells isolated from wild-caught greater horseshoe bats (*Rhinolophus*

### Figure 1. Derivation of pluripotent *Rhinolophus ferrumequinum* bat stem cells

- (A) Illustration of the bat pluripotent stem cell derivation strategy. BEF, embryonic fibroblasts; OSMK, Oct4, Sox2, cMyc, Klf4; FB, fibroblast medium; PSC, pluripotent stem cell medium; PSC+, PSC with additives.
- (B) Microscopic images of bat pluripotent stem cells at different magnifications showing morphology of established BiPS cell colonies grown on mouse embryonic fibroblasts.
- (C) Differential interference contrast microscopy image of BiPS cells highlighting prominent cytoplasmic vesicles.
- (D) Immunofluorescent detection of Oct4 in BiPS cells.
- (E) MA plot of RNA-seq data illustrating the transcriptional differences between bat embryonic fibroblast (BEF) and pluripotent stem cells (BiPS). Shown is the mean average of each gene from three replicates per cell type (n = 3). Selected genes with known functions in the establishment or maintenance of pluripotency are highlighted.
- (F) Kmean cluster analysis of ATAC-seq signals obtained from BEF or BiPS cells. Shown is the representative result of one of two replicates per cell type. C, cluster.
- (G) Density plot of RRBS results obtained from BEF and BiPS cells. Shown is the representative result of one of two replicates per cell type. PCC, Pearson correlation coefficient.
- (H) Scatter plots of histone 3 methylation status at K4 (activating chromatin modification) or K27 (repressing chromatin modification) after ChIP-seq from BEF or BiPS cells, as indicated. Shown are the results of one sample for each chromatin mark.
- (I) Scatter plot correlation of H3K4me3 and H3K27me3 in BiPS cells illustrating the occurrence of bivalent chromatin sites in BiPS cells.
- (J) RNA-seq, ATAC-seq, and H3K4me3 or H3K27me3 ChIP-seq signals of selected genes with known roles in reprogramming that are activated (Nanog, Kit) or repressed (Thy1) in BiPS when compared with BEF cells. Shown are tracks of one representative sample.

See also Figure S1 and Table S1.

*ferrumequinum*). Strikingly, the standard protocol<sup>55</sup> that is highly effective in mice, and after adjustments in humans and other mammalian species (e.g., domestic dog [*Canis familiaris*], domestic pig [*Sus scrofa*], common marmoset [*Callithrix jacchus*]), failed in bats. Even though the standard reprogramming protocol failed, it provided us with a crucial insight: the Yamanaka factors triggered the formation of rudimentary stem cell-like colonies even though they ceased to expand. This observation prompted us to suspect that the core pluripotency network might be conserved in bats, whereas the signaling cascades that usually shield this network from differentiation cues may differ. We therefore empirically altered the ratios and amounts of the reprogramming factors and, through a combinatorial approach, activated and blocked various cellular signaling pathways to ascertain whether they enabled stem cell reprogramming in bats. To this end, we identified that a specific ratio of reprogramming factors, and the addition of Lif, Scf, the Pka activator forskolin,<sup>56</sup> and Fgf2 to the culture medium, allowed for the uninterrupted growth of bat pluripotent stem cells (Figure 1A, detailed in the STAR methods section). Under these adjusted conditions, bat stem cell colonies typically appeared after 14–16 days of culture. These initial stem cell colonies were, however, not readily pickable and expandable using conventional EDTA (Versene)-, collagenase-, or trypsin-based methods that are normally used to passage pluripotent stem cells from other species. The only effective method seemed to be lightly flushing the cells off the feeder cell layer after gentle treatment with low concentrations of EDTA.

### Bat pluripotent stem cells

Bat induced pluripotent stem cell (iPSC) colonies appeared tight and homogeneous. The cells had a large, apparent nucleus with one or two prominent nucleoli and were filled with tiny vesicles not seen in other mammalian pluripotent stem cells (Figures 1B, 1C, and S1A). Bat iPSC cells expressed the pluripotency factor Oct4 as demonstrated by immunostaining (Figure 1D), and their proliferation rate was similar to human pluripotent cells. The cells retained a normal karyotype, with most cells containing 58 chromosomes (Figure S1B) and replicated in the absence of the exogenous reprogramming factors (Figure S1C), for now more than 100 passages without a change in morphology. RNA sequencing (RNA-seq) analyses (at passage 22) revealed the induced endogenous expression of canonical pluripotency-associated genes such as Oct4, Sox2 and Nanog (Figure 1E; Table S1A).

Next, we checked the effects of our reprogramming approach on the bat chromatin and epigenetic structures. A global epigenetic landscape survey using the assay for transposase-accessible chromatin with sequencing (ATAC-seq) revealed substantial chromatin configuration changes when bat fibroblasts transitioned into the pluripotent state (Figure 1F). Similarly, mapping the DNA methylome by reduced-representation bisulfite sequencing (RRBS) exposed major CpG methylation changes across the genome (Figures 1G, S1D; Tables S1C and S1D) after reprogramming. Finally, chromatin immunoprecipitation sequencing (ChIP-seq) for histone marks associated with active (H3K4me<sub>3</sub>) and developmentally repressed genes (H3K27me<sub>3</sub>) showed many changes (Figures 1H, 1I; Table S1E)

which were also associated with pluripotency genes (Figures 1J and 2A). Approximately 18.2% of the bat stem cell genes were associated with a “bivalent” domain (H3K4me<sub>3</sub> and H3K27me<sub>3</sub>; Figure S1E; Table S1F), a pluripotency chromatin hallmark initially found in human and mouse pluripotent cells.<sup>57</sup> Interestingly, while there was an overlap between human<sup>58</sup> and bat bivalency genes there were also some bat- or human-specific genes. Generally, there were strict correlations between an increase in gene expression and newly opened sites showing increased ATAC-seq signals and H3K4 trimethylation, along with decreased H3K27 trimethylation and DNA methylation in their promoters. Conversely, closed regions and gene shutdowns during the reprogramming process also corresponded to the absence of activating marks and presence of histone modifications, respectively (Figures 1J, 2A, and S1F–S1H). However, there were instances when we saw transcription and simultaneously active and repressive epigenetic marks, most likely as a result of spontaneous differentiation in our cultures (Figure 2A). Collectively, our results establish that our BiPS cells are reprogrammed, both transcriptionally and epigenetically. However, closer data inspection revealed that the expression and chromatin modification profiles (Figures 1J, 2A and 2B) did not fully match a single known pluripotency state. Instead, we saw factors indicative of the naive pluripotent state (e.g., Klf4, Klf17, Essrb, Tfcp2l1, Tfe3, Dppa, and Dusp6) expressed alongside genes typically found in the more advanced primed pluripotent cells (e.g., Otx2, Zic2), a phenomenon previously described for human cells under certain culture conditions, as it particularly pertains to lipid metabolism and the expression of Dusp6.<sup>59</sup> Indeed, double immunostainings detecting four of the most commonly used primed/naive factors, Otx2/Tfe3 and Tfcp2l1/Zic2, respectively, show the co-expression of naive and primed markers in most cells (Figure 2C). In contrast, germ cell factors such as Dnmt3l and Dazl were absent (Table S1). Thus, while cellular heterogeneity might be at play, their uniform appearance makes it most likely that bat stem cells might correspond to the formative state of pluripotency<sup>60</sup> or occupy a different, yet-to-be-characterized pluripotent default state.

The transcriptional and epigenetic changes mentioned above suggest, but are not definitive proof of, developmental pluripotency. To obtain functional evidence, we subjected the bat stem cells to protocols optimized for directed differentiation into ectodermal, mesodermal, and endodermal fates (Figure S2A). In each case, the cells responded to the altered culture conditions by shifting their morphology profoundly and turned positive for Pax6 (a marker for ectoderm), T (mesoderm), or AFP (endoderm), respectively (Figure 3A). Because the cells used in this experiment were at an advanced passage (passage 37, an equivalent of about 6 months of continuous culture), the results also suggest that pluripotency can be maintained long term. We next probed the developmental plasticity of bat stem cells by subjecting them to embryoid body (EB) differentiation, another classical *in vitro* pluripotency assay.<sup>61</sup> Again, the BiPS cells (referring to iPSC cells derived from *Rhinolophus ferrumequinum*) differentiated and formed spherical arrangements typical for EBs (Figure S2B), which subsequently matured into elaborate three-dimensional structures positive for all three germ layer markers (Figure 3B). RNA-seq analyses of RNA isolated from

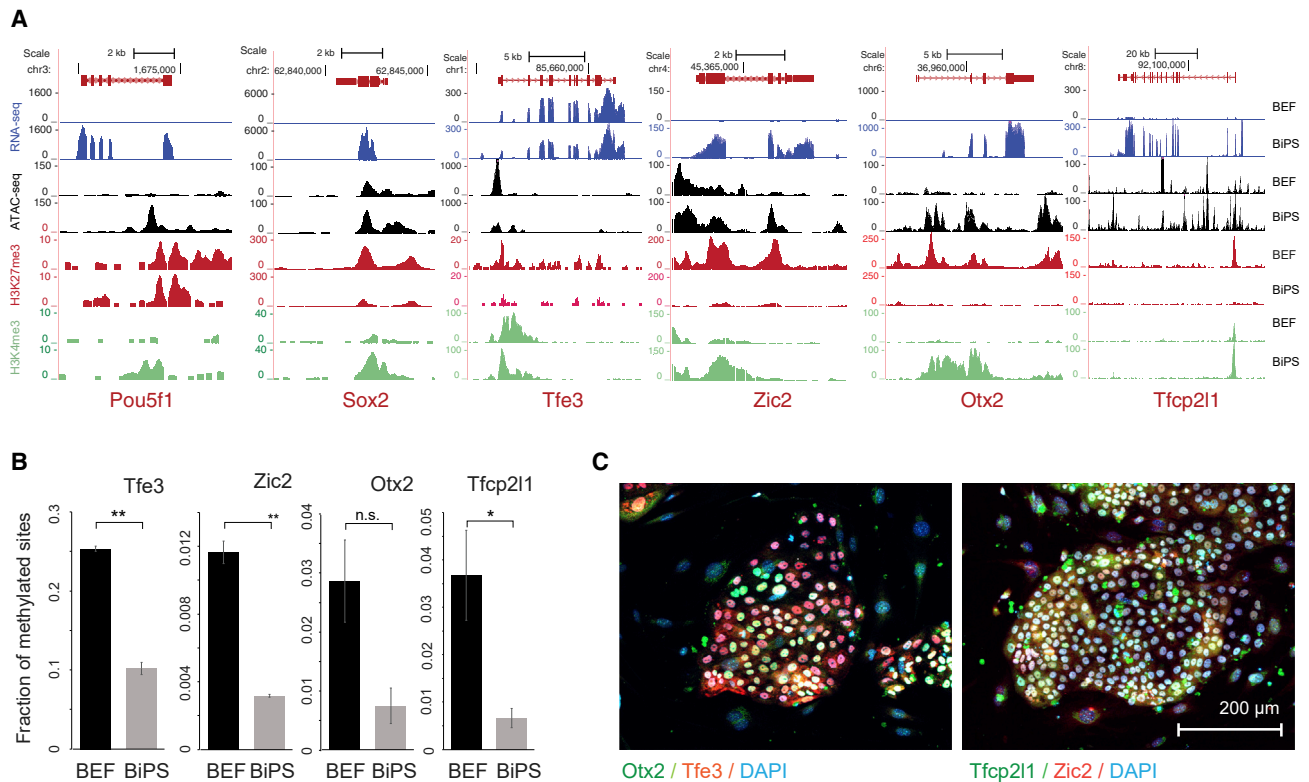


**Figure 2. Characteristics of pluripotency markers in pluripotent stem cells generated from *Rhinolophus ferrumequinum* fibroblasts**

(A) Sequencing tracks showing expression, ATAC-seq signal, histone H3K27 trimethylation (H3K27me3), and histone H3K4 trimethylation (H3K4me3) status of pluripotency markers Oct4 and Sox2 in bat embryonic fibroblasts (BEF) or induced pluripotent stem cells (BiPS).

(B) Fraction of methylated sites in promoters of pluripotency genes that did show promoter methylation. Data are shown as mean  $\pm$  SD of two replicates; p values were determined by t test:  $p = 0.0015$ ,  $0.0031$ ,  $0.0059$ , and  $0.0481$  from left to right. n.s., not significant. Note that we did not detect methylation in the promoters of Nanog, Pou5f1, or Sox2, which might be related to under-annotation of the *R. ferrumequinum* genome at present.

(C) Immunofluorescence images of bat pluripotent stem cells after staining of markers of naive (Tfe3 and Tfcp2l1) or primed pluripotency (Zic2 and Otx2).

See also Table S1.

the cells following monolayer differentiation and EB formation confirmed the respective cell fate changes (Figures 3C, and S2C and S2D; Table S2).

Next, we injected the *R. ferrumequinum* BiPS cells into immunocompromised mice because pluripotent stem cells typically form a particular tumor (teratoma) at the injection site,<sup>62</sup> composed of ectodermal, mesodermal, and endodermal cells arranged in a semi-chaotic fashion. Although it took substantially longer than usual for pluripotent cells derived from other species, BiPS cells eventually formed a similar type of tumor after four to five months, albeit infrequently (33%) and relatively small (2–4 mm). The tumors consisted of immature tissue with epithelial, neural, and stromal characteristics (Figure 3D). The transcriptional profile of pivotal genes (Table S1A) previously reported critical for teratoma formation<sup>63,64</sup> revealed that while some genes are downregulated in bat iPS cells in comparison with mouse iPS cells (like Eras), other genes like the hyaluronidases (HAS) and ADP ribosylation factors (ARFs) are indistinguishable between the experimental groups, making it likely that the anti-tumor effect seen in the rudimentary teratomas is a complex phenomenon. Although the host mice were severely immuno-

compromised and we had no access to immune-related tissues, the immaturity and delay in growth may suggest a yet-to-be-characterized anti-tumorigenic property of bat stem cells similar to, for instance, naked mole rats (*Heterocephalus glaber*),<sup>63,64</sup> and which could also underlie the extended health span and cancer resistance reported in many bats.<sup>8,9</sup> Finally, we created embryo-like structures from bat stem cells using a modified blastoid protocol.<sup>65</sup> These bat blastoids recapitulated critical aspects of preimplantation embryos, including an Oct4-positive inner cell mass, the cystic cavity, and a bilayered epithelium (Figure 3E) consisting of a trophoblast that stained positive for Cdx2 (Figure S2E) and yolk sac cells. Replating these embryo structures resulted in their attachment with a flattened trophoblastic epithelium outgrowth and an expansion of the inner cell mass (Figure 3F). Our differentiation studies exemplify the potential of pluripotent bat stem cells to study important developmental events and serve as a powerful model to study the exceptional physiological adaptations of bats, including their reduced cancer phenotype. Finally, to see whether our protocol is broadly applicable to bats, we created primary *Myotis* fibroblast cells from 3 mm uropatagium (tail) biopsies of wild-caught adult bats.

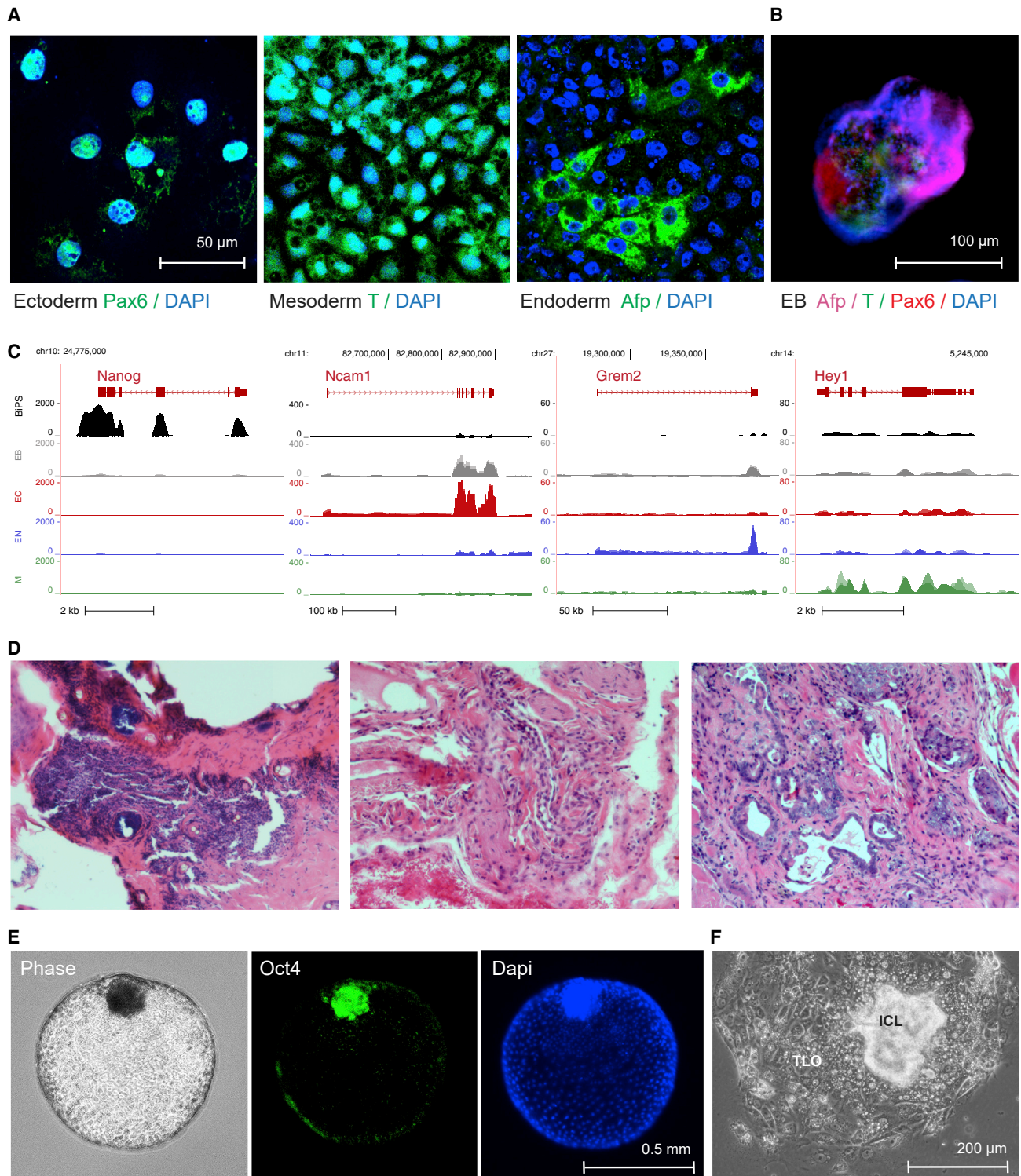


**Figure 3. Differentiation potential of *R. ferrumequinum* bat pluripotent stem cells.**

(A) Immunofluorescence microscopy images after staining with antibodies detecting the expression of lineage-specific markers Pax6, Afp, or brachyury (T) following specific directed differentiation into ectoderm, endoderm, or mesoderm, respectively.

(B) Immunofluorescence images of embryonic bodies (EB) that formed after 3D-differentiation of BiPS cells and were stained with antibodies to detect markers specific to all three germ layers as in (A).

(legend continued on next page)

These fibroblasts were readily reprogrammable using our “bati-fied” Yamanaka protocol and yielded bat iPS cells with a similar morphology that were Oct4 positive in immunostaining (Figures 4A and 4B). Importantly, they also showed co-expression of naive and primed pluripotency markers (Figure 4C) in most cells and differentiated into all three germ layers (Figure 4D). This suggests that our protocol is applicable across the deepest basal divergencies in bats.

### Comparative transcriptomics

Next, we investigated whether our stem cell model could be used to gain insights into the distinctive evolutionary adaptations of bats. Phenotypic differences among species can be driven by evolutionary changes in gene expression.<sup>66</sup> Therefore, given the special adaptations of bats, we should detect bat-specific gene expression patterns in bat stem cells, allowing us to compare the transcriptomic ground state across species, which is one of the earliest ontogenic comparisons possible. We collected transcriptome profiles of pluripotent stem cells from phylogenetically divergent mammal species (*Mus musculus* [mouse], *Homo sapiens* [human], *Canis familiaris* [dog], *Sus scrofa* [pig], and *Calithrix jacchus* [marmoset]) to compare them with our greater horseshoe bat (*Rhinolophus ferrumequinum*) data. Principal component analyses were performed to obtain a high-level overview of the number of commonalities and differences between bats and other mammals (Figure 5A). Remarkably, and supportive of our suspicion that bats are different, all other mammals grouped together in the PCA plot, while our bat stem cells formed a separate distinctive group, despite including other related laurasiatherian mammals.<sup>25</sup>

We then determined the gene signature that contributed the most to the bat-specific gene expression profile. Specifically, we extracted the “leading edge,” corresponding to the top 5% of the genes that fortified the difference in principal component 1 (Figure 5B; Table S3A) when comparing bat with mouse pluripotent stem cells. The list covered genes belonging to a broad spectrum of transcription factors, kinases, and metabolic and homeostatic enzymes. For instance, it included Hmg-CoA synthase *Hmgs2*, apolipoprotein *Apoa1*, cyclin *Ccnt1*, plasminogen *PLG*, pluripotency factors *Oct4* and *Nanog*, *Tmprss2* (required for SARS-CoV-2 entry in humans), and the ubiquitin ligase *Nedd4*, among many other genes. Given the broad spectrum of categories, we next asked whether the leading-edge genes were enriched for any particular biological pathway in gene ontology analyses (Figure 5C; Table S3B). We expected the genes to primarily encode developmental controllers and, indeed, some of the genes belonged to this class, but the vast

majority fell into rather unexpected categories. Among the enriched functional families were proteins targeting membranes, including the endoplasmic reticulum, lipid and cholesterol biosynthesis, and fibrinogen production. However, the most prominent groups were viral gene expression, viral transcription, and many sets activated or suppressed after viral infection (Figure 5D; Table S3B). “Coronavirus disease” was by far the most significantly enriched category in any KEGG pathway (Figure S5D; Table S3C). These results suggest that bat stem cells execute a program that in other mammalian cells is activated only after viral infection.

Interestingly, out of the set of leading-edge genes, only a total of eight genes showed significant evidence of positive selection in *R. ferrumequinum* (Figure 5E; Tables S3D and S3E). Two of these genes, *Col3a1*, and *Muc1*, have roles in collagen formation in connective tissues,<sup>67</sup> protect against pathogen infections,<sup>67</sup> and show evidence of selection in another bat species, suggesting discrete, bat-specific adaptations in these genes. Our results might indicate that the distinctive bat signature is likely the consequence of the presence of viral sequences triggering the expression of antiviral cellular programs and that most of the coding leading-edge genes are not under positive selection pressure.

### Endogenous viruses in bat stem cells

Throughout their evolution, bats have integrated diverse viral sequences into their genomes.<sup>21,27</sup> This is in line with our findings that multiple virus-infection-related gene categories are highly enriched in bat stem cells (Figure 5; Table S3). Because endogenized viral sequences are often awakened in the developmental *tabula rasa* state of pluripotency in humans and mice,<sup>48</sup> we hypothesized that our bat pluripotent stem cells would display a particularly rich set of expressed endogenized viral sequences and antigens compared with other mammals.

To advance the hypothesis, which that a particularly broad array of endogenized viral sequences would be re-activated in bat pluripotent stem cells to test, we looked first at endogenous retroviruses, which are abundant and diverse in bat genomes.<sup>24,25,27,68</sup> As a starting point, we picked anchor points of retroviral sequences, and mapping our RNA-seq from both *R. ferrumequinum* and *M. myotis* bat iPS cells revealed the expression of a markedly diverse set of retroviral families in bat pluripotent stem cells when compared with fibroblasts (Figures 6A and S3; Tables S4A and S4B). Focusing on *R. ferrumequinum* iPS cells, we detected not only previously characterized full-length bat retroviruses (Figure S4A) but also thus-far-unknown ones (e.g., RFe-V-MD1) that are transcriptionally activated

(C) RNA-seq signals of selected lineage-specific marker genes in BiPS cells that underwent monolayer differentiation as in (A) or embryonic body differentiation as in (B). Shown is one representative sequencing track ( $n = 3$ ) per condition. EB, embryonic body differentiation, EC, human ectoderm differentiation protocol; EN, human endoderm differentiation protocol; M, human mesoderm differentiation protocol.

(D) Microscopic images of hematoxylin-eosin-stained sections of tumor tissue after injection of BiPS cells into immunocompromised mice exhibiting ectodermal (left), mesodermal (middle), and endodermal (right) features.

(E) Images of floating blastoids that were obtained from BiPS cells after exposure to *Bmp4* to capture their morphology by phase-contrast microscopy (left) and to detect Oct4 expression in inner-cell mass-like cell clusters after immunofluorescence staining (middle, right).

(F) Phase-contrast microscopy image of a typical blastocyst-outgrowth-like cell cluster that formed after the attachment of blastoids to the cell culture vessel surface during *Bmp4*-induced differentiation as in (E). ICL, inner cell mass-like; TLO, trophoblast-like outgrowth.

See also Figure S2 and Table S2.

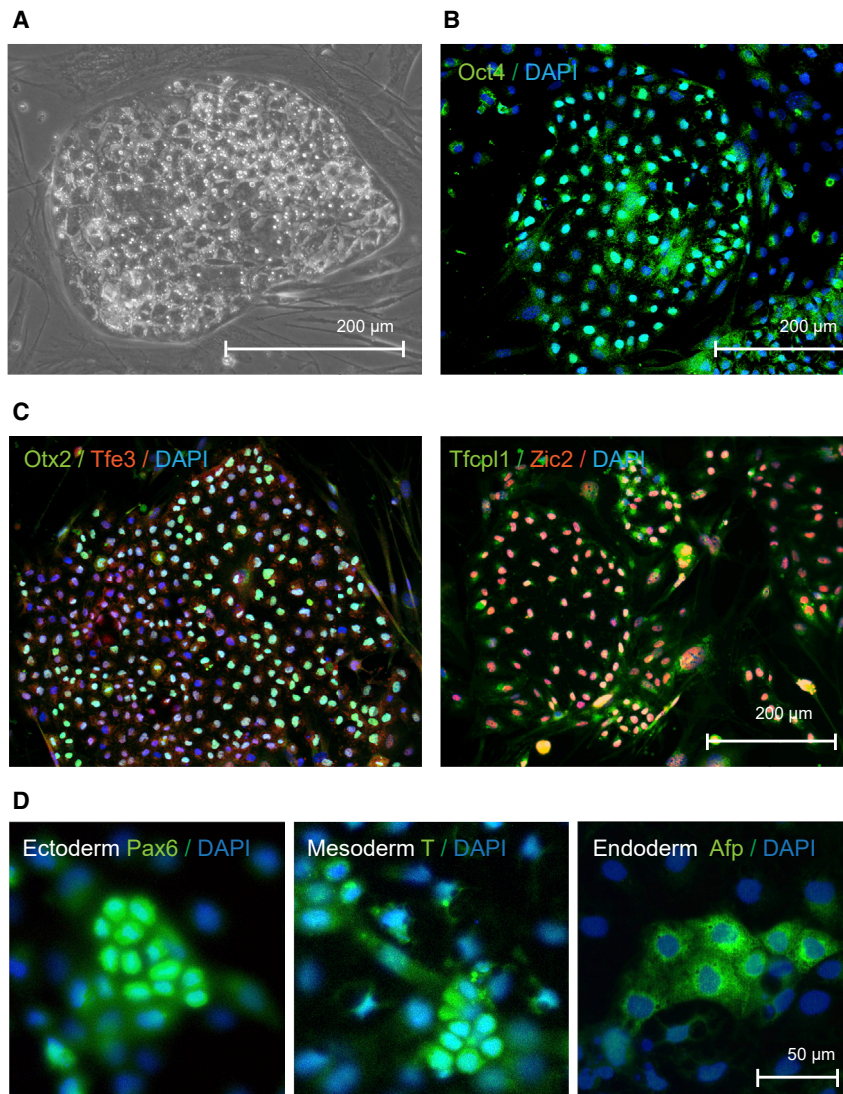


**Figure 4. Characterization of induced pluripotent stem cells derived *Myotis myotis* uropatagium fibroblasts**

(A) Phase contrast image of *Myotis myotis* iPS cells. (B) Microscopic image of *Myotis myotis* iPS cells after immunostaining to detect pluripotency marker Oct4.

(C) Immunofluorescence images of *Myotis myotis* pluripotent stem cells after staining of markers of naive (Tfe3 and Tfcp2l1) or primed pluripotency (Zic2 and Otx2).

(D) Microscopic images of *Myotis myotis* iPS cells that underwent differentiation and immunostaining to detect Pax6, brachyury (T) and Afp as markers for ectoderm, mesoderm, and endoderm, respectively.

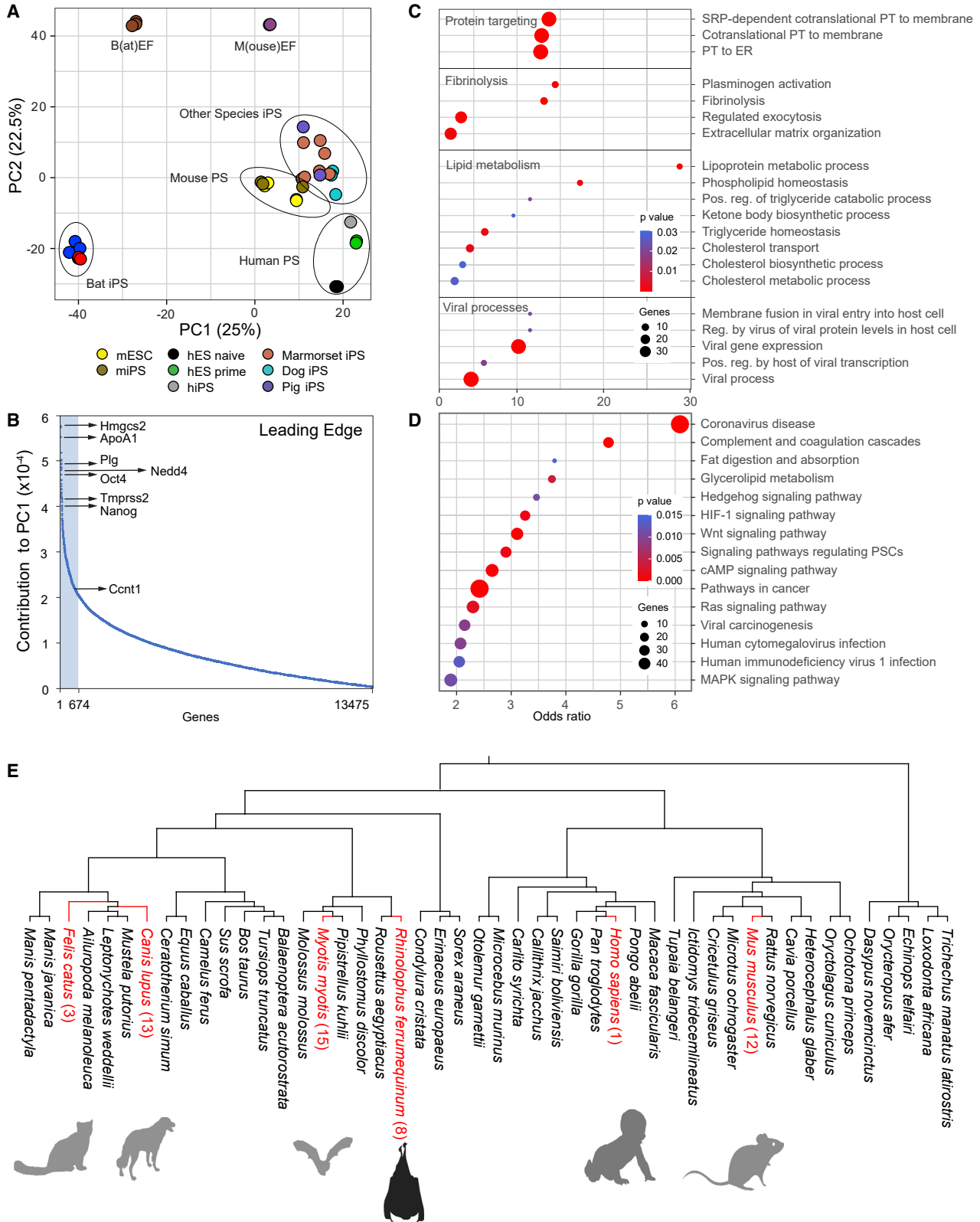
cles per ml, as determined in a retroviral assay and 0.3 ng/well in a direct reverse transcriptase assay). However, when we inoculated Vero cells with the supernatant of our bat iPS cells in plaque assays, we did not detect any measurable cytotoxic effects, in contrast to the acute infectious virus particles that served as positive controls (Figure S4C). These findings imply that bat cells produce ERV antigen and, in some instances, possibly active endogenous viral-like assemblies at an unusual scale compared with other mammals.

In addition to ERVs, bat genomes have also assimilated a substantial number and diversity of endogenous viral elements (EVE).<sup>25</sup> Hence, we attempted to obtain a broader portrait of integrated and expressed viral sequences. We developed pipelines based on the metagenomic classification of the stem cell RNA-seq data, using either Kraken2 or Microsoft Premonition (Figure S5; Tables S5 and S6), which included a series of strict classification

during reprogramming (Figure 6B; Table S4C). Importantly, chromatin in the vicinity of the expressed endogenous retroviruses opened up epigenetically during reprogramming, confirming our suspicion that the reprogramming process was responsible for revealing the diverse set of endogenous retroviruses (ERVs) sequences in our bat stem cells (Figure S4B).

To determine whether the transcript-based findings indeed hold true at the protein level, we then determined whether the ERV antigen was present in our bat stem cells. Indeed, western blotting and immunostaining revealed high levels of ERV antigen in the bat stem cells of both species, which were not detected in human or mouse stem cells or fibroblasts (Figures 6C and 6D). Additionally, transmission electron microscopy (TEM) revealed electron-dense particles with lucent cores, ranging in size from 50 to 100 nm, which in some instances resembled previously reported viral-like particles (VLPs) (Figure 6E).<sup>48</sup> Although the exact nature of these particles needs to be explored further, virus-like activity was detectable in the supernatant ( $1.21 \times 10^{10}$  viral parti-

(using the k-mer-based Kraken2 and the alignment-based Microsoft Premonition) and curation steps (*de novo* assembly of putative viral contigs and genome mapping) to identify true viral reads (Figures S6A and S6B; STAR methods). The analyses revealed that bat pluripotent stem cells display a variety of virus-associated endogenized sequences. For instance, Blast analysis of selected suspected viral Iso-seq reads, as identified by our metagenomics method, showed an unexpected region in the first intron of the Xpa gene (DNA damage and repair factor) on chromosome 12 (Figure S6C). The region showed homology to two human herpesvirus 4 isolates (HKD40 and HKNPC60), the human respiratory syncytial virus (Kilifi isolate), and a fragment of about 500 bp that was identified at the end of a SARS-CoV2 isolate from an infected patient (Figure S6D; Table S7A). We also found a nearly 50% identical sequence to either *Scotophilus* bat coronavirus 512 (Tables S7A and S7B) or *RaTG13* coronavirus (one of the bat coronaviruses most closely resembling SARS-CoV-2), covering most of the spike encoding sequences



(legend on next page)

(Tables S7A and S7C). Phylogenetic analysis revealed that these genomic sequences resembled the spike encoding genomic portion of viruses, such as the human coronavirus 229E and human coronavirus OC43, respectively (Figure S6E). Interestingly, these regions are flanked by LINE-1 sequences (Figure S6F). This suggests the possibility that LINE elements are directly involved in the homing of viral RNA, a possibility that was also explored recently in the context of SARS-CoV-2.<sup>69</sup> Systematically scanning for expressed viral elements in our RNA we then assembled contigs and aligned them to viral and mammalian genomes using BLAST (Figure S5) and employing highly stringent parameters (Figures S6A and S6B; STAR methods). This procedure allowed us to identify previously unknown viral sequences and integration sites (Tables S6 and S7). Although many of the viral alignments were difficult to distinguish from cellular genes (e.g., oncogenes), especially in pipelines that did not include genome mapping steps, we detected what appeared to be *bona fide* purely viral-like elements that were integrated in the bat genome and induced in our pluripotent stem cells.

We identified numerous predicted and so-far-unknown retroviral integrations with homologies to the Koala retrovirus (Table S6), Mason-Pfizer monkey virus (Tables S7A and S7D), Jaagsiekte sheep retrovirus, or Ovine enzootic nasal tumor virus (Table S7A and S7E), to name a few. Translations of the extended regions covered by mapped RNA-seq reads using BLASTX revealed similarities to the Jaagsiekte sheep reverse transcriptase (Table S7E) and other known retroviral gag, pro, and pol proteins (Table S7). An example of an integrated DNA virus sequence is a region within scaffold\_m29\_p\_1 of the *R. ferrumequinum* genome, which shows homologies to the Volepox, Variola, Squirrelpox, and Monkeypox viruses (Figure S7D). Here, translation of the extended region with mapped RNA-seq reads uncovered homologies with the cowpox protein CPXV051 and the monkeypox C10L protein (Tables S7A and S7G). Another region that is worth noting is located within scaffold\_m29\_p\_20. We first identified this region through a short sequence homology with the SARS-related coronavirus isolate Rs7907, coding for an N-terminal fragment of a double-stranded RNA (dsRNA)-binding protein (Table S6N; Figure S7E). When extending this region to cover all mapped RNA-seq reads in the vicinity, a BLAST search identified several longer homologies with the White spot syndrome virus (Figure S7F; Tables S7A and S7H). Interestingly, we find mapped RNA-seq reads in fibroblasts and iPS cells and that the genomic location borders a

“gap” region in the genome, indicating that even more of this non-mammalian virus might be present in the bat genome. Notably, a comparison of the metagenomic diversity, as determined by Kraken2 using RNA-seq data from BEFs and from human ES cells (Tables S5B and S5C), yielded some viral sequences, albeit to a much lesser degree (Figure S6A). In summary, we conclude that, while confounding effects including genomic contaminations can affect the metagenomic classification process, it is highly likely that a sizable body of proviral sequences and sequence fragments inhabit BiPS cells.

To support our transcriptomics-based findings, we next looked for antigen markers linked with the RNA virus lifestyle because bats have traditionally shown an extreme affinity for RNA viruses and, in some cases, coronaviruses.<sup>70</sup> We first stained our bat iPS cells with an antibody detecting a corona-virus antigen. This was based on the fact that bats are known to host coronaviruses, and early during the SARS-CoV-2 pandemic *Rhinolophidae sp.* were considered as a host for SARS-CoV2, and our discovery of sequences that resemble corona-viruses (Figure S6; Table S7). Indeed, we found the BiPS cells to be positive in immunofluorescence and western blot analyses when compared with fibroblasts and pluripotent stem cells from other species (Figures 7A and 7B). Super-resolution microscopy showed clustered localization within the cytoplasm (Figure 7C). We then looked for the presence of dsRNA in immunostaining which is thought to be a sign of replicative genomes from both positive-strand dsRNA and DNA viruses (Figure 7D). Super-resolution imaging (Figure 7E) showed that the dsRNA was present in micron-order-sized aggregates throughout the cytoplasm but essentially absent from the nucleus. Further, ImageStream analysis revealed an overlap between the dsRNA signal and the distinctive intracellular vesicles found in bat stem cells (Figures 7F and 7G). However, the precise involvement of these vesicles in viral activities needs to be further investigated. Finally, in line with the pro-viral environment on a transcriptional level, we found that bat stem cells infected with an exogenous Metapneumovirus (MPV) revealed a particularly permissive environment for viral persistence when compared with mouse stem cells, further underscoring the supportive nature of bat stem cells for viruses (Figures S7G and S7H).

## DISCUSSION

Bats have evolved an unusual lifestyle among mammals as they fly, use echolocation, and have a curious affinity for viruses. One

### Figure 5. Distinct characteristics of bat pluripotent stem cells

(A) Principal component analysis of *R. ferrumequinum* induced pluripotent bat stem cells (BiPS) in comparison to those derived from other species. h, human; m, mouse. PS, pluripotent stem cells; iPS, induced pluripotent stem cells; ES, embryonic stem cells; EF, embryonic fibroblasts. Each dot represents one dataset. (B) Plot of genes that contribute to the differences of pluripotent bat and mouse stem cells as part of principal component 1 (PC1). Highlighted in light blue is the “leading edge” comprised of the top 5% of PC1-contributing genes. (C) Selected GO and (D) KEGG pathways identified to be significantly enriched among the top 5% of PC1-contributing genes/leading-edge genes defined in (B) were plotted by their odds ratio, with the color of each circle indicating the enrichment p value and the size indicating the number of genes present in the respective category (see Data Tables S3B and S3C for a full list of enriched gene sets). ER, endoplasmic reticulum; PT, protein targeting; Pos, positive; Reg, regulation. (D) Selection analyses of leading-edge genes by comparative genomics of the *R. ferrumequinum* lineage identified only eight genes (AARD, COL3A1, FAM111A, LAMB3, MUC1\*, NES\*, RGS5, RSPH1\*) with significant evidence of positive selection, five of which showed at least one highly probable BEB site with no visual issues in the alignment region, while three genes (designated with \*) did not (see Table S5E). Additional lineages and the number of leading-edge genes with significant evidence of positive selection found in them are highlighted in red. See also Table S3.

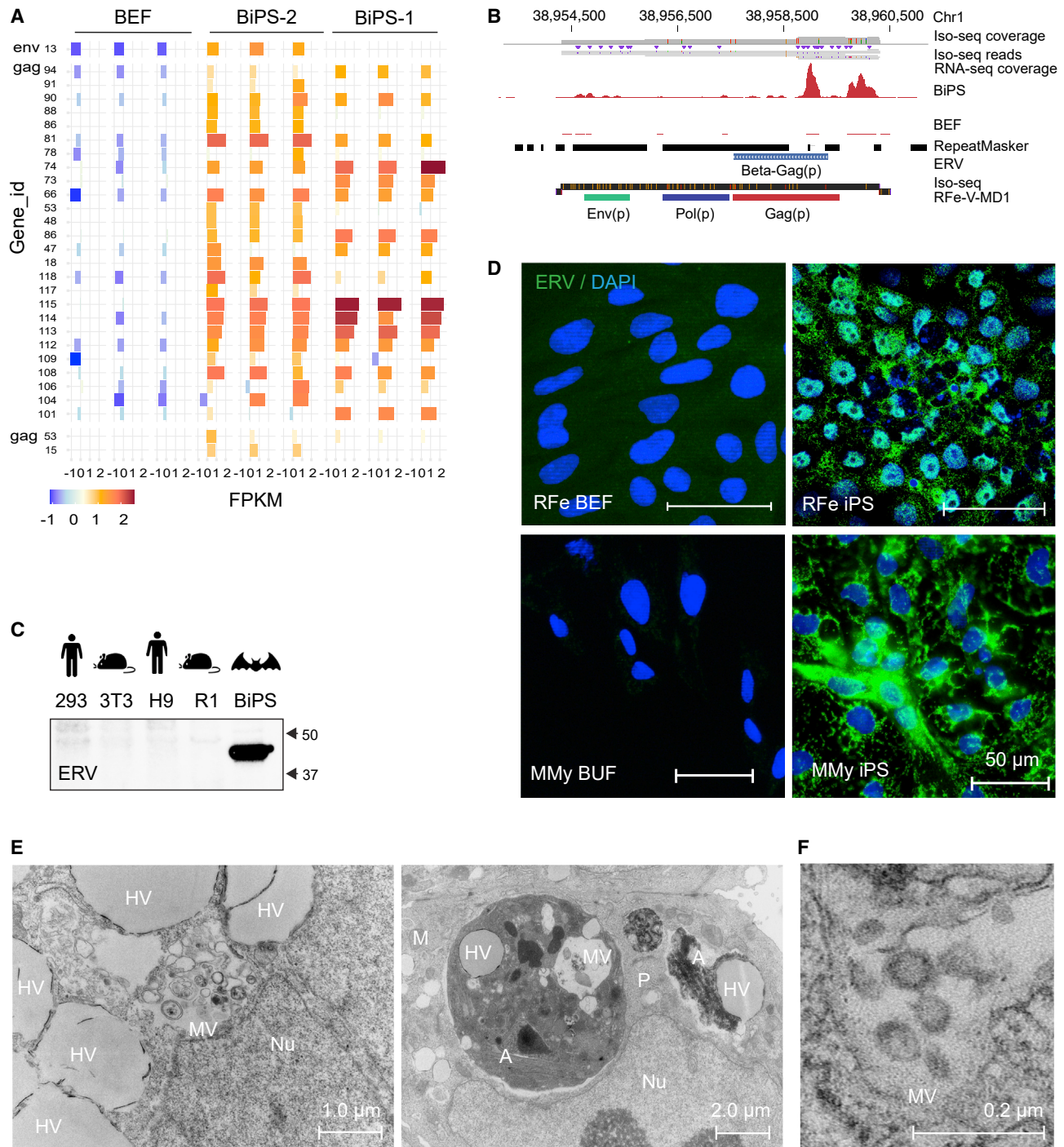


**Figure 6. Reactivation of endogenized retroviral elements in bat induced pluripotent stem cells.**

(A) Expression of indicated ERV elements in *R. ferrumequinum* bat embryonic fibroblasts (BEF) and iPS cells (BiPS), as determined by extracting the overlap between RNA-seq reads mapped to the *R. ferrumequinum* genome and known mapped ERV elements. Shown are the elements with the most evident differences (see Data Table S4A for a full list of expression data). All replicates (n = 3) per cell type are shown.

(B) RNA and Iso-seq sequencing tracks for an identified full-length retrovirus sequence, RFe-V-MD1, aligned to the *R. ferrumequinum* genome. The Iso-seq fragment represents a 6,088 bp-long transcript (ID: 39584940).

(C) Western blotting of protein lysates from human 293FT (kidney tumor cells) and human embryonic stem cells (H9), mouse 3T3 (fibroblasts) and mouse embryonic stem cells (R1), and *R. ferrumequinum* bat induced pluripotent stem cells (BiPS) with the endogenous retrovirus (ERV)-specific HERV K Cap antibody.

(legend continued on next page)

possibility is that bats evolved a tolerance for viruses by evolving changes in their innate immunity resembling the virus evasion mechanisms of the mammalian immune response. Another possibility is that bats evolved mechanisms for a cellular program to support viral replication and persistence, comparable to how viruses manipulate the host cell. Our results support both perspectives.

Indeed, our results show that a potentially significant contingent of endogenous and exogenous viral products is present in bat pluripotent stem cells without severely compromising their ability to proliferate and grow and that this goes beyond how other pluripotent stem cells react to viruses. Viruses typically adapt their replication cycles to a particular cell type. Thus, one would not expect the pluripotent stem cell state to align with viruses' often specialized requirements.<sup>49</sup> Nevertheless, our data suggest that in bats the pluripotent state serves as an "umbrella" host for a highly divergent viral contingent. We propose that our culture model can help to carefully dissect the necessary balance for tolerance of viral infections. Our bat stem cell system will also provide insights into bats' potential role as virus reservoirs and the relationship between bats and viruses. *In vitro* differentiation into immune cells and tissues, such as lung or gut epithelium, will illuminate emerging viruses, develop bats as new model study systems, provide new insights into how bats tolerate viral infections, and, in turn, allow us to better prepare for future pandemics.

Careful cataloging of acute exogenous bat viruses, tissue infection, persistent viruses, and endogenized viruses in geographically relevant regions<sup>71,72</sup> will reveal members of diverse retroviral and non-retroviral sequences, potentially impacting the host and emerging viruses. It will also uncover rationales for virus persistence, including immune-modulatory strategies,<sup>3</sup> symbiotic protection against other pathogens,<sup>73–75</sup> biological warfare that bats use to deploy viruses,<sup>18</sup> mammalian adaptive piRNA or CRISPR-like systems,<sup>76</sup> and the augmentation of evolutionary processes.<sup>77</sup> Although the events we specifically study in pluripotent stem cells do not directly impact those occurring in specific adult cells, we propose that pluripotent stem cells are, in their own right, an important cell system in the study of native immunity and viruses. They share a highly conserved<sup>78</sup> and immunologically relevant common genetic program with somatic cells.<sup>79</sup> Pluripotent stem cells in the embryo and the related trophoblastic tissue must establish their immunological barrier against the maternal tissue and are subject to viral infection, as also noted in bats.<sup>80</sup> Furthermore, as some fundamental cell biological properties might be shared between stem cells,<sup>81,82</sup> the finding may also extend to other stem cells often at risk of infection, such as hematopoietic stem cells,<sup>83</sup> neural stem cells,<sup>84,85</sup> and early human embryos where, for instance, the rubella virus can destroy the conceptus or cause

severe congenital defects.<sup>86</sup> Also, most basic native immunity systems with pathogen pattern sensing and inflammatory responses, including inflammasome, NF $\kappa$ B, and interferon, are basic tools largely present in their most ancient ancestors and broadly shared between species and cell types.<sup>87,88</sup> Finally, viral RNA products present in bat cells might also represent a potential source for RNA recombination upon infection with exogenous homologous viruses, which could be a driver for viral evolution in bats.

Our bat stem cell system may also provide a much-needed experimental substrate to parse the tantalizing hypothesis that viruses and hosts are more entangled than previously thought and that viruses are fully competent agents and editors of host biology.<sup>46</sup> Therefore, viruses must be rich sources of evolutionary instructions, especially given their extreme genetic adaptability and ability to transition between the living and chemical worlds.<sup>45,89</sup> Allowing viral evolutionary processes to unfold in our bat cell lines and mapping out changes to the host transcriptome will be critical steps toward understanding host-virus editing interactions.

The results of our study provide proof-of-concept evidence that bat stem cells include a remarkable variety of sequences that are similar to viral genomic sequences. Additionally, our findings indicate that retroviruses, and parts of endogenous viruses other than retroviruses, are produced and active on a scale that is not generally seen in tumor or stem cell lines that originate from other animals or humans studied so far. We conclude that the transcriptionally permissive state of pluripotency can be exploited to discover bat viruses and derivative sequences that likely play an essential role in bat physiology and their ability to host viruses.

Bats are a critically needed model organism to better understand disease tolerance, but limited access to animal and cell models has hindered their study.<sup>36,90</sup> Bat breeding colonies for some species are notoriously challenging to establish; most bat species are protected worldwide, and primary bat cell lines typically have a limited *in vitro* lifespan.<sup>36</sup> Therefore, pluripotent stem cells offer a research tool that is a *sine qua non* for bat research. Once established, pluripotent stem cells divide indefinitely in culture and are very amenable to gene editing and molecular studies.<sup>91</sup> Most importantly, pluripotent stem cells retain the ability to differentiate into any cell type in the body and are often used as a springboard for sophisticated tissue culture models<sup>92</sup> and, more recently, virus studies.<sup>93,94</sup> Future research on bat stem cells will directly impact every aspect of understanding bat biology, including bats' amazing adaptations of flight, echolocation, extreme longevity, and unusual immunity. Although bat genomes are the natural starting point for studying such adaptations and are being generated by the Bat1K consortium,<sup>4,5</sup> our pluripotent stem cell system will enable specific

(D) Immunofluorescence images of *R. ferrumequinum* (RFe) bat embryonic fibroblasts (BEFs) and iPS cells from (top) and *M. myotis* (MMY) bat uropatagium fibroblasts (BUF) and iPS cells (bottom) after detection of the endogenous retrovirus (ERV) HERV K Cap protein (green); DAPI (blue).

(E) Overview of transmission electron microscopy of *R. ferrumequinum* bat pluripotent stem cells. MV, vesicles filled with multimembrane structures; HV, other vesicle structures filled with homogenous content; Nu, Nucleus; A, autophagosome; M, mitochondria; P, phagosome.

(F) Higher magnification of electron microscopy images as in (E) showing the presence of aggregates that are morphologically compatible with the appearance of endogenous retrovirus-like particles.

See also [Figure S3](#) and [Table S4](#).

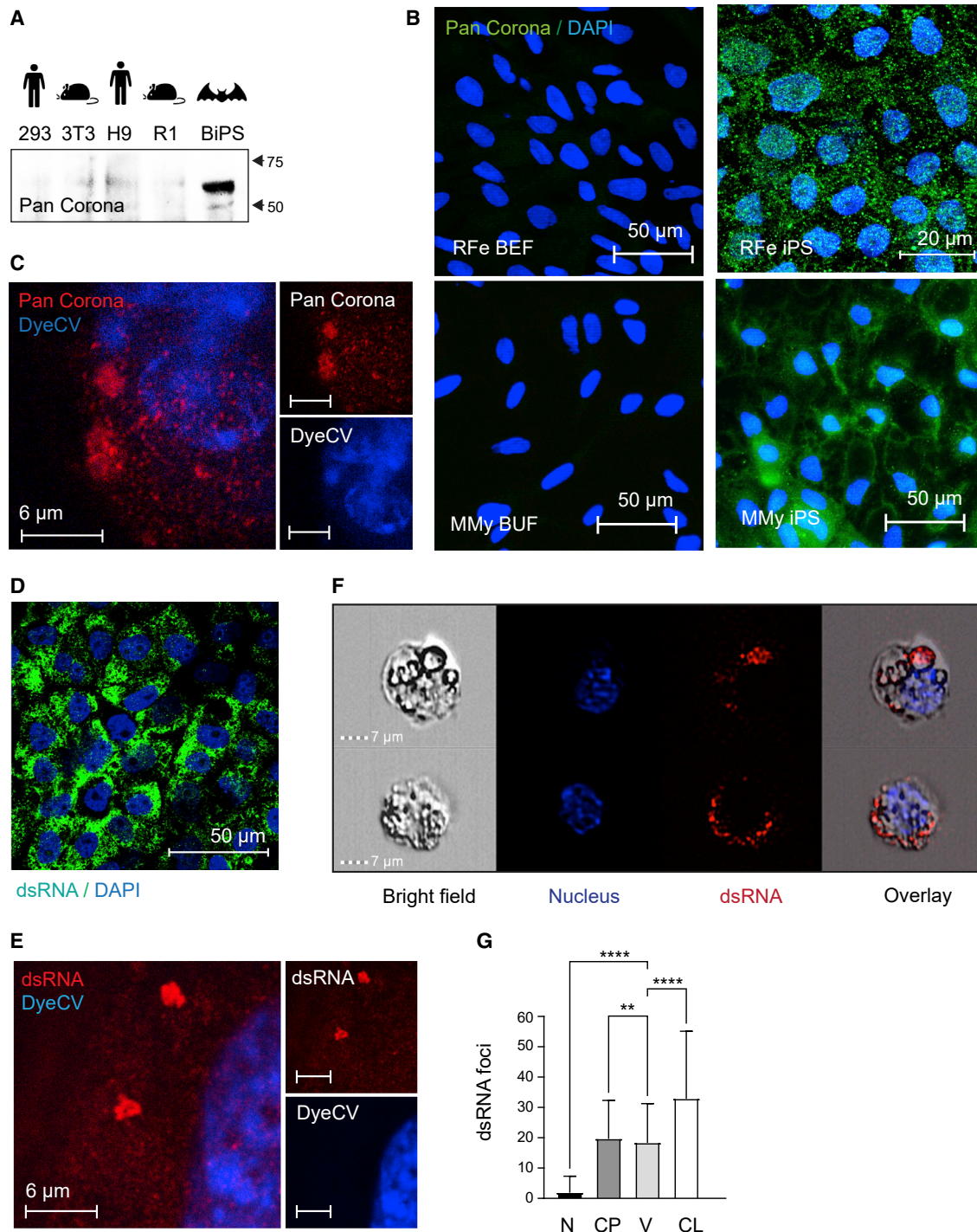


**Figure 7. Reactivation of endogenized viral elements in bat pluripotent stem cells**

(A) Western blotting of protein lysates isolated from human 293FT and H9, mouse 3T3 and R1, and *R. ferrumequinum* BiPS cells with a pan coronavirus antibody known to be specific for the nucleocapsid; its reactivity includes, but might not be limited to, feline infectious peritonitis virus type 1 and 2, canine coronavirus (CCV), pig coronavirus transmissible gastroenteritis virus (TGEV), and ferret coronavirus.

(B) Immunofluorescence images of *R. ferrumequinum* (RFe) bat embryonic fibroblasts (BEFs) and iPS cells from (top) and *M. myotis* (MMy) bat uropatagium fibroblasts (BUF) and iPS cells (bottom) after detection of the pan coronavirus antigen (green); DAPI (blue).

(legend continued on next page)

bat tissue studies, and organoids will let us test more complex relationships, gene editing, and specific evolutionary hypotheses. Bat stem cell lines and differentiated progeny will help address tantalizing physiology questions, provide the required tools for validation, and utilize the genomic basis of rare adaptations found in bats.

### Limitations of the study

Currently, viral metagenomic classification of only recently assembled diverse non-model mammalian genomes and transcriptomes, such as those in bats, is still limited, given the lack of viral comparative studies and knowledge of these key taxa. These results will need further verification at the protein level and using future curated assemblies. Obtaining wild lethal and non-lethal bat samples can be a challenge, and the derived cell lines may not capture population-level diversity in ERV and other viruses. However, our results are a solid starting point to carefully revisit the plethora of genomic and expressed bat viral sequences and to test whether they are integrated sequences to defend against viruses and microbes and encode viral proteins in a self-vaccination scheme or are near full-length viruses to manipulate host physiology. While at this point it is not feasible to perform comprehensive quantitative comparative studies of viral-like sequences between species with any degree of certainty, mainly because the number of characterized human viruses vastly exceeds those of other species based on the bias toward human viral research, we hope that our study will serve as the foundation for such tool development. Also, the reactivation of endogenized virus fragments exposes only part of the host tissue response and needs to be investigated in other cell types and acute viruses. Furthermore, how closely our pluripotent stem cell lines resemble different inner cell mass (ICM) states, and the impact of our tissue culture protocol, will only be ascertained by comparing them to bat ICM cells and the generation of bat chimeras. This current proof-of-concept study establishes bat stem cells in particular, and bats in general, as tantalizing model systems, allowing us to both elucidate the diversity of viruses that bats can survive and the molecular adaptations that enable bats to asymptotically tolerate these viruses, thus providing important insights into both disease surveillance and future therapeutics.

### STAR★METHODS

Detailed methods are provided in the online version of this paper and include the following:

- **KEY RESOURCES TABLE**

- **RESOURCE AVAILABILITY**

- Lead contact
- Materials availability
- Data and code availability

- **EXPERIMENTAL MODEL AND SUBJECT DETAILS**

- Bats

- **METHOD DETAILS**

- Reprogramming of bat fibroblasts
- Karyotyping
- RT-PCR
- Immunofluorescence staining
- RNA-seq, differential expression analyses and visualization
- MA plot
- Heatmap
- ATAC-seq
- Reduced representation bisulfite sequencing (RRBS)
- Chromatin immunoprecipitation sequencing (ChIP-seq)
- Three germ layer differentiation
- Embryonic body differentiation
- Blastoid differentiation
- Teratoma formation
- Western blot analyses
- Principal component analysis (PCA)
- Evolutionary selection analysis
- Gene ontology and KEGG pathway analyses
- Protein interaction network analysis
- Electron microscopy
- Image-based flow cytometry (ImageStream)
- Retrovirus assay
- Reverse transcriptase assay
- Plaque assay
- Metapneumovirus (MPV) infection of BiPS and mES cells
- Iso-Seq library preparation and sequencing
- Identification and illustration of viral sequences in the bat pluripotent stem cell transcriptome
- Mapping of RNA-seq reads to bat genomes and quantifying expression of ERVs
- *De novo* assembly of potential virus-derived RNA-seq
- Mapping transcripts to viral and mammalian databases

- **QUANTIFICATION AND STATISTICAL ANALYSIS**

### SUPPLEMENTAL INFORMATION

Supplemental information can be found online at <https://doi.org/10.1016/j.cell.2023.01.011>.

(C) Representative STED microscopy image of *R. ferrumequinum* iPS cells after detecting the Corona antigen as in (B) and DyeCycle Violet (DyeCV) nuclear counter stain (blue).

(D) Immunofluorescence images of *R. ferrumequinum* BiPS cells after detection of double-stranded RNA (green) characteristic of RNA viruses; DAPI (blue).

(E) Representative STED microscopy image of *R. ferrumequinum* iPS cells after immunofluorescence staining of double-stranded RNA (dsRNA) as in (D).

(F) ImageStream analysis after immunofluorescence staining of BiPS cells as in (D and E). A brightfield image, DyeCycle Violet nuclear staining (blue), dsRNA staining (red), and an overlay is shown for each representative cell.

(G) Quantification of dsRNA foci by ImageStream in *R. ferrumequinum* iPS cells show in (F). Data are presented as mean  $\pm$  SD;  $n = 1,846$  cells.  $**p < 0.01$ ,  $****p < 0.0001$  by one-way ANOVA with Bonferroni's multiple comparisons test. RFe, *Rhinolophus ferrumequinum*; BEF, bat embryonic fibroblasts; CP, cytoplasm; CL, cell; iPS, induced pluripotent stem cells; MMy, Myotis myotis; N, nucleus; V, vesicle; BUF, bat uropatagium fibroblasts.

See also [Figures S4–S7](#) and [Tables S5, S6, and S7](#).

## ACKNOWLEDGMENTS

We thank Prof. Eloy Revilla Ebd-CSIC's director, the EBD-CSIC's Bio-Ethical Committee, the CABIMER, the Consejería de Medio-Ambiente of the Junta de Andalucía and the Subdirección General de Acuerdos Sanitarios y Control en Frontera of the Spanish Ministry of Agricultura, Pesca y Alimentación, for their support and help in obtaining the export permits in record time and many other people for making the shipment and delivery of the *Rhinolophus* samples from Seville, Spain, to New York, USA, under the COVID-19 pandemic's most arduous conditions possible. We thank the members of Bretagne Vivante, local volunteers, and students from University College Dublin for their help in sample collection and the owners/local authorities for allowing access to the sites to collect *Myotis* samples in France. We also thank Michael Schotsaert and Carles Martinez for helping with the bat tissue import, Allison Sova and Bill Williams from the Microscopy Core and Advanced Bioimaging Center at the Icahn School of Medicine for preparing the cells for the electron microscopy and imaging, as well as Glenn Doherty and Nikolas Tzavaras for their assistance with the confocal microscopy. We also thank the Genomics and the Biorepository and Pathology Core Facility members at the Icahn School of Medicine at Mount Sinai for performing the RNA-seq and histology, respectively. This work was supported in part by the computational resources and staff expertise provided by Scientific Computing at the Icahn School of Medicine at Mount Sinai. E.C.T. is supported by Irish Research Council Laureate Award IRCLA/2017/58 and Science Foundation Ireland Future Frontiers 19/FFP/6790. G.M.H. is funded by a University College Dublin Ad Astra Fellowship. M.D. and T.P.Z. are supported by the Huffington Foundation. T.P.Z. is supported by NIH GM129329 and HD100518. A.G.S. is supported by HR0011-19-2-0020, awarded by DARPA, and grant No. W81XWH-20-1-0270, awarded by the Department of Defense (DoD). This work was also partially supported by NIAID grant U19AI135972 and by CRIPT (Center for Research on Influenza Pathogenesis and Response), a NIAID-supported Center of Excellence for Influenza Research and Response (CEIRR, contract #75N93019R00028) to A.G.S. and by grant 2021-244135(5384) from the Open Philanthropy Project Fund to A.G.S. and T.P.Z., while J.J. and C.I. are supported by the Spanish Ministerio de Ciencia e Innovación (SAF2017-89355-P). R.A.Y. is supported by NIH R35 GM144283. A.E.M. and M.H. are supported by the LOEWE-Centre for Translational Biodiversity Genomics (TBG). The graphical abstract was created with [BioRender.com](https://BioRender.com).

## AUTHOR CONTRIBUTIONS

Conceptualization, M.D., R.A.Y., E.C.T., A.G.S., and T.P.Z.; methodology, M.D.; formal analysis, M.D., A.M., G.M.H., A.E.M., C.G.P., J.L.G., Y.Q., A.A.S., R.R., A.P., and M.H.; investigation, M.D., C.G.P., Y.Q., A.A.S., H.X., and R.R.; resources, J.J., C.I., D.A., E.C.T., A.P., and S.D.W.F.; data curation, M.D.; writing – original draft, M.D., R.A.Y., and T.P.Z.; writing – review & editing, M.D., E.C.T., A.G.S., R.A.Y., T.P.Z., and S.D.W.F.; visualization, M.D.; supervision, M.D. and T.P.Z.; project administration, M.D., K.M.W., N.J.F., R.P.S., T.L.V., S.J.P., S.D.W.F., and T.P.Z.; funding acquisition, M.D., R.A.Y., E.C.T., A.G.S., and T.P.Z.

## DECLARATION OF INTERESTS

T.P.Z., M.D., and A.G.S. are inventors on patents and patent applications on the use of bat iPS cells, owned by the Icahn School of Medicine at Mount Sinai, New York. T.P.Z. and R.A.Y. are founders and shareholders of Paratus Sciences, and R.A.Y. is a founder and shareholder of Syros Pharmaceuticals, Camp4 Therapeutics, Omega Therapeutics, and Dewpoint Therapeutics. The A.G.S. laboratory has received research support from Pfizer, Senhwa Biosciences, Kenall Manufacturing, Avimex, Johnson & Johnson, Dynavax, 7Hills Pharma, Pharmamar, ImmunityBio, Accurius, Nanocomposix, Hexamer, N-Fold LLC, Model Medicines, and Merck, outside of the reported work. A.G.S. has consulting agreements for the following companies involving cash and/or stock: Vivaldi Biosciences, Contrafact, 7Hills Pharma, Avimex, Vaxalto, Pagoda, Accurius, Esperovax, Farmak, Applied Biological Laboratories, and Pfizer, outside of the reported work. A.G.S. is inventor on patents and patent applications on the use of antivirals and vaccines for the treatment

and prevention of virus infections and cancer, owned by the Icahn School of Medicine at Mount Sinai, New York, outside of the reported work. A.M. is the creator of Omics Bioinformatics and owns all the stocks of this company. R.P.S. has a consulting agreement with Sema4 involving cash and is also a stockholder of this company. A.P. and S.D.W.F. are employees of Microsoft Corporation. S.D.W.F. is co-founder of DIOSynVax, Ltd. and an inventor on patent applications on the design of vaccine immunogens for the prevention of virus infections, outside of the reported work.

## INCLUSION AND DIVERSITY

We support the inclusive, diverse, and equitable conduct of research.

Received: September 23, 2022

Revised: December 6, 2022

Accepted: January 9, 2023

Published: February 21, 2023

## REFERENCES

1. Simmons, N., and Cirranello, A. (2020). Bat species of the world: a taxonomic and geographic database. <https://batnames.org/>.
2. Allen, G. (1939). *Bats* (Harvard University Press).
3. Nagel, T. (1974). What is it like to be a bat. *The Philosophical Review* **83**, 159–168.
4. Teeling, E., Dool, S., and Springer, M. (2012). Phylogenies, fossils and functional genes: the evolution of echolocation in bats. *Evol. Hist. Bats Fossils Mol. Morphol.*, 1–22.
5. Teeling, E.C., Vernes, S.C., Dávalos, L.M., Ray, D.A., Gilbert, M.T.P., and Myers, E.; Bat1K Consortium (2018). Bat biology, genomes, and the Bat1K project: to generate chromosome-level genomes for all living bat species. *Annu. Rev. Anim. Biosci.* **6**, 23–46.
6. Teeling, E.C., Springer, M.S., Madsen, O., Bates, P., O'Brien, S.J., and Murphy, W.J. (2005). A molecular phylogeny for bats illuminates biogeography and the fossil record. *Science* **307**, 580–584.
7. Altringham, J.D. (2011). *Bats: from evolution to conservation* (Oxford University Press).
8. Munshi-South, J., and Wilkinson, G.S. (2010). Bats and birds: exceptional longevity despite high metabolic rates. *Ageing Res. Rev.* **9**, 12–19.
9. Wilkinson, G.S., and Adams, D.M. (2019). Recurrent evolution of extreme longevity in bats. *Biol. Lett.* **15**, 20180860.
10. Hermida Lorenzo, R.J., Cadar, D., Koundouno, F.R., Juste, J., Bialonski, A., Baum, H., Garcia-Mudarra, J.L., Hakamaki, H., Bencsik, A., Nelson, E.V., et al. (2021). Metagenomic snapshots of viral components in Guinean bats. *Microorganisms* **9**, 599.
11. Luis, A.D., Hayman, D.T., O'Shea, T.J., Cryan, P.M., Gilbert, A.T., Pulliam, J.R., Mills, J.N., Timonin, M.E., Willis, C.K., Cunningham, A.A., et al. (2013). A comparison of bats and rodents as reservoirs of zoonotic viruses: are bats special? *Proc. R. Soc. Lond. B* **280**, 20122753.
12. Olival, K.J., Hosseini, P.R., Zambrana-Torrel, C., Ross, N., Bogich, T.L., and Daszak, P. (2017). Host and viral traits predict zoonotic spillover from mammals. *Nature* **546**, 646–650.
13. Anthony, S.J., Johnson, C.K., Greig, D.J., Kramer, S., Che, X., Wells, H., Hicks, A.L., Joly, D.O., Wolfe, N.D., Daszak, P., et al. (2017). Global patterns in coronavirus diversity. *Virus Evol.* **3**, vex012.
14. Brook, C.E., and Dobson, A.P. (2015). Bats as 'special' reservoirs for emerging zoonotic pathogens. *Trends Microbiol.* **23**, 172–180.
15. Drexler, J.F., Corman, V.M., Müller, M.A., Maganga, G.D., Vallo, P., Binger, T., Gloza-Rausch, F., Cottontail, V.M., Rasche, A., Yordanov, S., et al. (2012). Bats host major mammalian paramyxoviruses. *Nat. Commun.* **3**, 796.
16. O'Shea, T.J., Cryan, P.M., Cunningham, A.A., Fooks, A.R., Hayman, D.T., Luis, A.D., Peel, A.J., Plowright, R.K., and Wood, J.L. (2014). Bat flight and zoonotic viruses. *Emerg. Infect. Dis.* **20**, 741–745.

17. Van Brussel, K., and Holmes, E.C. (2022). Zoonotic disease and virome diversity in bats. *Curr. Opin. Virol.* *52*, 192–202.
18. Wang, L.F., Walker, P.J., and Poon, L.L. (2011). Mass extinctions, biodiversity and mitochondrial function: are bats 'special' as reservoirs for emerging viruses? *Curr. Opin. Virol.* *1*, 649–657.
19. Banerjee, A., Baker, M.L., Kulcsar, K., Misra, V., Plowright, R., and Mossman, K. (2020). Novel insights into immune systems of bats. *Front. Immunol.* *11*, 26.
20. Brook, C.E., Boots, M., Chandran, K., Dobson, A.P., Drosten, C., Graham, A.L., Grenfell, B.T., Müller, M.A., Ng, M., Wang, L.F., and Leeuwen, A.v. (2020). Accelerated viral dynamics in bat cell lines, with implications for zoonotic emergence. *eLife* *9*, e48401.
21. Pourrut, X., Souris, M., Towner, J.S., Rollin, P.E., Nichol, S.T., Gonzalez, J.P., and Leroy, E. (2009). Large serological survey showing cocirculation of Ebola and Marburg viruses in Gabonese bat populations, and a high seroprevalence of both viruses in *Rousettus aegyptiacus*. *BMC Infect. Dis.* *9*, 159.
22. Yob, J.M., Field, H., Rashdi, A.M., Morrissy, C., van der Heide, B., Rota, P., bin Adzhar, A., White, J., Daniels, P., Jamaluddin, A., and Ksiazek, T. (2001). Nipah virus infection in bats (order Chiroptera) in peninsular Malaysia. *Emerging infectious diseases* *7*, 439–41.
23. Cui, J., Tachedjian, M., Wang, L., Tachedjian, G., Wang, L.F., and Zhang, S. (2012). Discovery of retroviral homologs in bats: implications for the origin of mammalian gammaretroviruses. *J. Virol.* *86*, 4288–4293.
24. Hayward, J.A., Tachedjian, M., Cui, J., Cheng, A.Z., Johnson, A., Baker, M.L., Harris, R.S., Wang, L.F., and Tachedjian, G. (2018). Differential evolution of antiretroviral restriction factors in pteropid bats as revealed by APOBEC3 gene complexity. *Mol. Biol. Evol.* *35*, 1626–1637.
25. Jebb, D., Huang, Z., Pippel, M., Hughes, G.M., Lavrichenko, K., Devanna, P., Winkler, S., Jermini, L.S., Skirmuntt, E.C., Katzourakis, A., et al. (2020). Six reference-quality genomes reveal evolution of bat adaptations. *Nature* *583*, 578–584.
26. Skirmuntt, E.C., Escalera-Zamudio, M., Teeling, E.C., Smith, A., and Katzourakis, A. (2020). The potential role of endogenous viral elements in the evolution of bats as reservoirs for zoonotic viruses. *Annu. Rev. Virol.* *7*, 103–119.
27. Skirmuntt, E.C., and Katzourakis, A. (2019). The evolution of endogenous retroviral envelope genes in bats and their potential contribution to host biology. *Virus Res.* *270*, 197645.
28. Cui, J., Tachedjian, G., and Wang, L.F. (2015). Bats and rodents shape mammalian retroviral phylogeny. *Sci. Rep.* *5*, 16561.
29. Escalera-Zamudio, M., Rojas-Anaya, E., Kolokotronis, S.O., Taboada, B., Loza-Rubio, E., Méndez-Ojeda, M.L., Arias, C.F., Osterrieder, N., and Greenwood, A.D. (2016). Bats, primates, and the evolutionary origins and diversification of mammalian gammaherpesviruses. *mBio* *7*, e01425-01416.
30. Hayman, D.T., Bowen, R.A., Cryan, P.M., McCracken, G.F., O'Shea, T.J., Peel, A.J., Gilbert, A., Webb, C.T., and Wood, J.L. (2013). Ecology of zoonotic infectious diseases in bats: current knowledge and future directions. *Zoonoses Public Health* *60*, 2–21.
31. Middleton, D.J., Morrissy, C.J., Van Der Heide, B.M., Russell, G.M., Braun, M.A., Westbury, H.A., Halpin, K., and Daniels, P.W. (2007). Experimental Nipah virus infection in pteropid bats (*Pteropus poliocephalus*). *J. Comp. Pathol.* *136*, 266–272.
32. Swanepoel, R., Leman, P.A., Burt, F.J., Zachariades, N.A., Braack, L.E., Ksiazek, T.G., Rollin, P.E., Zaki, S.R., and Peters, C.J. (1996). Experimental inoculation of plants and animals with Ebola virus. *Emerg. Inf. Dis.* *2*, 321–325.
33. Watanabe, S., Masangkay, J.S., Nagata, N., Morikawa, S., Mizutani, T., Fukushi, S., Alviola, P., Omatsu, T., Ueda, N., Iha, K., et al. (2010). Bat coronaviruses and experimental infection of bats, the Philippines. *Emerg. Inf. Dis.* *16*, 1217–1223.
34. Moreno Santillán, D.D., Lama, T.M., Gutierrez Guerrero, Y.T., Brown, A.M., Donat, P., Zhao, H., Rossiter, S.J., Yohe, L.R., Potter, J.H., Teeling, E.C., et al. (2021). Large-scale genome sampling reveals unique immunity and metabolic adaptations in bats. *Mol. Ecol.* *30*, 6449–6467.
35. Kacprzyk, J., Hughes, G.M., Palsson-McDermott, E.M., Quinn, S.R., Puechmaile, S.J., O'Neill, L.A.J., and Teeling, E.C. (2017). A potent anti-inflammatory response in bat macrophages may be linked to extended longevity and viral tolerance. *Acta Chiropterol.* *19*, 219–228.
36. Wang, L.F., Gamage, A.M., Chan, W.O.Y., Hiller, M., and Teeling, E.C. (2021). Decoding bat immunity: the need for a coordinated research approach. *Nat. Rev. Immunol.* *21*, 269–271.
37. Baker, M.L., Schountz, T., and Wang, L.F. (2013). Antiviral immune responses of bats: a review. *Zoonoses Public Health* *60*, 104–116.
38. Irving, A.T., Ahn, M., Goh, G., Anderson, D.E., and Wang, L.F. (2021). Lessons from the host defences of bats, a unique viral reservoir. *Nature* *589*, 363–370. <https://doi.org/10.1038/s41586-020-03128-0>.
39. Ahn, M., Anderson, D.E., Zhang, Q., Tan, C.W., Lim, B.L., Luko, K., Wen, M., Chia, W.N., Mani, S., Wang, L.C., et al. (2019). Dampened NLRP3-mediated inflammation in bats and implications for a special viral reservoir host. *Nat. Microbiol.* *4*, 789–799.
40. Goh, G., Ahn, M., Zhu, F., Lee, L.B., Luo, D., Irving, A.T., and Wang, L.F. (2020). Complementary regulation of caspase-1 and IL-1 $\beta$  reveals additional mechanisms of dampened inflammation in bats. *Proc. Natl. Acad. Sci. USA* *117*, 28939–28949.
41. Mozzi, A., Pontremoli, C., Forni, D., Clerici, M., Pozzoli, U., Bresolin, N., Cagliani, R., and Sironi, M. (2015). OASes and STING: adaptive evolution in concert. *Genome Biol. Evol.* *7*, 1016–1032.
42. Pavlovich, S.S., Lovett, S.P., Koroleva, G., Guito, J.C., Arnold, C.E., Nangle, E.R., Kulcsar, K., Lee, A., Thibaud-Nissen, F., Hume, A.J., et al. (2018). The Egyptian rousette genome reveals unexpected features of bat antiviral immunity. *Cell* *173*, 1098–1110.e18.
43. Xie, J., Li, Y., Shen, X., Goh, G., Zhu, Y., Cui, J., Wang, L.F., Shi, Z.L., and Zhou, P. (2018). Dampened STING-dependent interferon activation in bats. *Cell Host Microbe* *23*, 297–301.e4.
44. Garcia-Sastre, A. (2017). Ten strategies of interferon evasion by viruses. *Cell Host Microbe* *22*, 176–184.
45. Villarreal, L.P., Defilippis, V.R., and Gottlieb, K.A. (2000). Acute and persistent viral life strategies and their relationship to emerging diseases. *Virology* *272*, 1–6.
46. Witzany, G. (2010). Biocommunication and natural genome editing. *World J. Biol. Chem.* *1*, 348–352.
47. Wray, J., Kalkan, T., and Smith, A.G. (2010). The ground state of pluripotency. *Biochem. Soc. Trans.* *38*, 1027–1032.
48. Grow, E.J., Flynn, R.A., Chavez, S.L., Bayless, N.L., Wossidlo, M., Wessche, D.J., Martin, L., Ware, C.B., Blish, C.A., Chang, H.Y., et al. (2015). Intrinsic retroviral reactivation in human preimplantation embryos and pluripotent cells. *Nature* *522*, 221–225.
49. Macfarlan, T.S., Gifford, W.D., Driscoll, S., Lettieri, K., Rowe, H.M., Bonanomi, D., Firth, A., Singer, O., Trono, D., and Pfaff, S.L. (2012). Embryonic stem cell potency fluctuates with endogenous retrovirus activity. *Nature* *487*, 57–63.
50. Rowe, H.M., and Trono, D. (2011). Dynamic control of endogenous retroviruses during development. *Virology* *411*, 273–287.
51. Wang, J., Xie, G., Singh, M., Ghanbarian, A.T., Raskó, T., Szvetnik, A., Cai, H., Besser, D., Prigione, A., Fuchs, N.V., et al. (2014). Primate-specific endogenous retrovirus-driven transcription defines naive-like stem cells. *Nature* *516*, 405–409.
52. Mo, X., Li, N., and Wu, S. (2014). Generation and characterization of bat-induced pluripotent stem cells. *Theriogenology* *82*, 283–293.
53. Aurine, N., Baquerre, C., Gaudino, M., Jean, C., Dumont, C., Rival-Gervier, S., Kress, C., Horvat, B., and Pain, B. (2021). Reprogrammed Pteropus Bat stem cells as A model to study Host-Pathogen Interaction during Henipavirus Infection. *Microorganisms* *9*, 2567.

54. Takahashi, K., and Yamanaka, S. (2006). Induction of pluripotent stem cells from mouse embryonic and adult fibroblast cultures by defined factors. *Cell* 126, 663–676.
55. Hochedlinger, K., and Jaenisch, R. (2015). Induced pluripotency and epigenetic reprogramming. *Cold Spring Harb. Perspect. Biol.* 7, a019448.
56. Hanna, J., Cheng, A.W., Saha, K., Kim, J., Lengner, C.J., Soldner, F., Cassady, J.P., Muffat, J., Carey, B.W., and Jaenisch, R. (2010). Human embryonic stem cells with biological and epigenetic characteristics similar to those of mouse ESCs. *Proc. Natl. Acad. Sci. USA* 107, 9222–9227.
57. Bernstein, B.E., Mikkelsen, T.S., Xie, X., Kamal, M., Huebert, D.J., Cuff, J., Fry, B., Meissner, A., Wernig, M., Plath, K., et al. (2006). A bivalent chromatin structure marks key developmental genes in embryonic stem cells. *Cell* 125, 315–326.
58. Court, F., and Arnaud, P. (2017). An annotated list of bivalent chromatin regions in human ES cells: a new tool for cancer epigenetic research. *Oncotarget* 8, 4110–4124.
59. Cornacchia, D., Zhang, C., Zimmer, B., Chung, S.Y., Fan, Y., Soliman, M.A., Tchieu, J., Chambers, S.M., Shah, H., Paull, D., et al. (2019). Lipid deprivation induces a stable, naive-to-primed intermediate state of pluripotency in human PSCs. *Cell Stem Cell* 25, 120–136.e10.
60. Smith, A. (2017). Formative pluripotency: the executive phase in a developmental continuum. *Development* 144, 365–373.
61. Wiles, M.V., and Keller, G. (1991). Multiple hematopoietic lineages develop from embryonic stem (ES) cells in culture. *Development* 111, 259–267.
62. Damjanov, I., and Andrews, P.W. (2007). The terminology of teratocarcinomas and teratomas. *Nat. Biotechnol.* 25, 1212; discussion 1212.
63. Miyawaki, S., Kawamura, Y., Oiwa, Y., Shimizu, A., Hachiya, T., Bono, H., Koya, I., Okada, Y., Kimura, T., Tsuchiya, Y., et al. (2016). Tumour resistance in induced pluripotent stem cells derived from naked mole-rats. *Nat. Commun.* 7, 11471.
64. Tan, L., Ke, Z., Tomblin, G., Macoretta, N., Hayes, K., Tian, X., Lv, R., Ablaeva, J., Gilbert, M., Bhanu, N.V., et al. (2017). Naked mole rat cells have a stable epigenome that resists iPSC reprogramming. *Stem Cell Rep.* 9, 1721–1734.
65. Yu, L., Wei, Y., Duan, J., Schmitz, D.A., Sakurai, M., Wang, L., Wang, K., Zhao, S., Hon, G.C., and Wu, J. (2021). Blastocyst-like structures generated from human pluripotent stem cells. *Nature* 597, 620–626.
66. Romero, I.G., Ruvinsky, I., and Gilad, Y. (2012). Comparative studies of gene expression and the evolution of gene regulation. *Nat. Rev. Genet.* 13, 505–516.
67. Kuivaniemi, H., and Tromp, G. (2019). Type III collagen (COL3A1): gene and protein structure, tissue distribution, and associated diseases. *Gene* 707, 151–171.
68. Zhuo, X., Rho, M., and Feschotte, C. (2013). Genome-wide characterization of endogenous retroviruses in the bat *Myotis lucifugus* reveals recent and diverse infections. *J. Virol.* 87, 8493–8501.
69. Zhang, L., Richards, A., Barrasa, M.I., Hughes, S.H., Young, R.A., and Jaenisch, R. (2021). Reverse-transcribed SARS-CoV-2 RNA can integrate into the genome of cultured human cells and can be expressed in patient-derived tissues. *Proc. Natl. Acad. Sci. USA* 118, e2105968118.
70. Villarreal, L.P. (2009). Persistence pays: how viruses promote host group survival. *Curr. Opin. Microbiol.* 12, 467–472.
71. Wacharapluesadee, S., Tan, C.W., Maneeorn, P., Duengkae, P., Zhu, F., Joyjinda, Y., Kaewpom, T., Chia, W.N., Ampoot, W., Lim, B.L., et al. (2021). Evidence for SARS-CoV-2 related coronaviruses circulating in bats and pangolins in Southeast Asia. *Nat. Commun.* 12, 972.
72. Zhou, H., Ji, J., Chen, X., Bi, Y., Li, J., Wang, Q., Hu, T., Song, H., Zhao, R., Chen, Y., et al. (2021). Identification of novel bat coronaviruses sheds light on the evolutionary origins of SARS-CoV-2 and related viruses. *Cell* 184, 4380–4391.e14.
73. Barton, E.S., White, D.W., Cathelyn, J.S., Brett-McClellan, K.A., Engle, M., Diamond, M.S., Miller, V.L., and Virgin, H.W. (2007). Herpesvirus latency confers symbiotic protection from bacterial infection. *Nature* 447, 326–329.
74. Eaton, B.T., Broder, C.C., Middleton, D., and Wang, L.F. (2006). Hendra and Nipah viruses: different and dangerous. *Nat. Rev. Microbiol.* 4, 23–35.
75. Roossinck, M.J. (2011). The good viruses: viral mutualistic symbioses. *Nat. Rev. Microbiol.* 9, 99–108.
76. Ophinni, Y., Palatini, U., Hayashi, Y., and Parrish, N.F. (2019). piRNA-guided CRISPR-like immunity in eukaryotes. *Trends Immunol.* 40, 998–1010.
77. Feschotte, C., and Gilbert, C. (2012). Endogenous viruses: insights into viral evolution and impact on host biology. *Nat. Rev. Genet.* 13, 283–296.
78. Endo, Y., Kamei, K.I., and Inoue-Murayama, M. (2020). Genetic signatures of evolution of the pluripotency gene regulating network across mammals. *Genome Biol. Evol.* 12, 1806–1818.
79. Wu, X., Thi, V.L.D., Huang, Y., Billerbeck, E., Saha, D., Hoffmann, H.H., Wang, Y., Silva, L.A.V., Sarbanes, S., Sun, T., et al. (2018). Intrinsic immunity shapes viral resistance of stem cells. *Cell* 172, 423–438.e25.
80. Aikawa, H., Tamai, M., Mitamura, K., Itmainati, F., Barber, G.N., and Tagawa, Y.-i. (2014). Innate immunity in an in vitro murine blastocyst model using embryonic and trophoblast stem cells. *J. Biosci. Bioeng.* 117, 358–365.
81. Ivanova, N.B., Dimos, J.T., Schaniel, C., Hackney, J.A., Moore, K.A., and Lemischka, I.R. (2002). A stem cell molecular signature. *Science* 298, 601–604.
82. Ramalho-Santos, M., Yoon, S., Matsuzaki, Y., Mulligan, R.C., and Melton, D.A. (2002). "Stemness": transcriptional profiling of embryonic and adult stem cells. *Science* 298, 597–600.
83. Carter, C.C., McNamara, L.A., Onafuwa-Nuga, A., Shackleton, M., Riddell, J., Bixby, D., Savona, M.R., Morrison, S.J., and Collins, K.L. (2011). HIV-1 utilizes the CXCR4 chemokine receptor to infect multipotent hematopoietic stem and progenitor cells. *Cell Host Microbe* 9, 223–234.
84. Janssens, S., Schotsaert, M., Karnik, R., Balasubramaniam, V., Déjosez, S., Meissner, A., García-Sastre, A., and Zwaka, T.P. (2018). Zika virus alters DNA methylation of neural genes in an organoid model of the developing human brain. *mSystems* 3, e00219-00217.
85. Li, H., Saucedo-Cuevas, L., Regla-Nava, J.A., Chai, G., Sheets, N., Tang, W., Tersikh, A.V., Shresta, S., and Gleeson, J.G. (2016). Zika virus infects neural progenitors in the adult mouse brain and alters proliferation. *Cell Stem Cell* 19, 593–598.
86. Naeye, R.L., and Blanc, W. (1965). Pathogenesis of congenital rubella. *JAMA* 194, 1277–1283.
87. Daugherty, M.D., and Malik, H.S. (2012). Rules of engagement: molecular insights from host-virus arms races. *Annu. Rev. Genet.* 46, 677–700.
88. Siddle, K.J., and Quintana-Murci, L. (2014). The Red Queen's long race: human adaptation to pathogen pressure. *Curr. Opin. Genet. Dev.* 29, 31–38.
89. Villarreal, L.P. (2007). Review article virus-host symbiosis mediated by persistence. *Symbiosis*.
90. Rasweiler, J.J., Crettekos, C.J., and Behringer, R.R. (2009). Feeding short-tailed fruit bats (*Carollia perspicillata*). *Cold Spring Harb. Protoc.* 2009, pdb.prot5159.
91. Takahashi, K., and Yamanaka, S. (2016). A decade of transcription factor-mediated reprogramming to pluripotency. *Nat. Rev. Mol. Cell Biol.* 17, 183–193.
92. Lancaster, M.A., Renner, M., Martin, C.A., Wenzel, D., Bicknell, L.S., Hurles, M.E., Homfray, T., Penninger, J.M., Jackson, A.P., and Knoblich, J.A. (2013). Cerebral organoids model human brain development and microcephaly. *Nature* 501, 373–379.

93. White, K.M., Rosales, R., Yildiz, S., Kehrer, T., Miorin, L., Moreno, E., Jangra, S., Uccellini, M.B., Rathnasinghe, R., Coughlan, L., et al. (2021). Pli-tidepsin has potent preclinical efficacy against SARS-CoV-2 by targeting the host protein eEF1A. *Science* **371**, 926–931.
94. Yang, L., Han, Y., Nilsson-Payant, B.E., Gupta, V., Wang, P., Duan, X., Tang, X., Zhu, J., Zhao, Z., Jaffré, F., et al. (2020). A human pluripotent stem cell-based platform to study SARS-CoV-2 tropism and model virus infection in human cells and organoids. *Cell Stem Cell* **27**, 125–136.e7.
95. Yoshimatsu, M., Ohnishi, H., Zhao, C., Hayashi, Y., Kuwata, F., Kaba, S., Okuyama, H., Kawai, Y., Hiwatashi, N., Kishimoto, Y., et al. (2021). In vivo regeneration of rat laryngeal cartilage with mesenchymal stem cells derived from human induced pluripotent stem cells via neural crest cells. *Stem Cell Res.* **52**, 102233.
96. Carter, A.C., Davis-Dusenbery, B.N., Koszka, K., Ichida, J.K., and Eggan, K. (2014). Nanog-independent reprogramming to iPSCs with canonical factors. *Stem Cell Rep.* **2**, 119–126.
97. Io, S., Kabata, S., M., Iemura, Y., Semi, K., Morone, N., Minagawa, A., Wang, B., Okamoto, I., Nakamura, T., Kojima, Y., et al. (2021). Capturing human trophoblast development with naive pluripotent stem cells in vitro. *Cell Stem Cell* **28**, 1023–1039.e13.
98. Selmi, T., Hussain, S., Dietmann, S., Heiß, M., Borland, K., Flad, S., Carter, J.M., Dennison, R., Huang, Y.L., Kellner, S., et al. (2021). Sequence- and structure-specific cytosine-5 mRNA methylation by NSUN6. *Nucleic Acids Res.* **49**, 1006–1022.
99. Andrews, S., Krueger, F., Segonds-Pichon, A., Biggins, L., Krueger, C., and Wingett, S. (2010). FastQC. A Quality Control Tool for High Throughput Sequence Data370.
100. Bolger, A.M., Lohse, M., and Usadel, B. (2014). Trimmomatic: a flexible trimmer for Illumina sequence data. *Bioinformatics* **30**, 2114–2120.
101. Kim, D., Paggi, J.M., Park, C., Bennett, C., and Salzberg, S.L. (2019). Graph-based genome alignment and genotyping with HISAT2 and HISAT-genotype. *Nat. Biotechnol.* **37**, 907–915.
102. Li, H., Handsaker, B., Wysoker, A., Fennell, T., Ruan, J., Homer, N., Marth, G., Abecasis, G., and Durbin, R.; 1000 Genome Project Data Processing Subgroup (2009). The sequence alignment/map format and SAMtools. *Bioinformatics* **25**, 2078–2079.
103. Liao, Y., Smyth, G.K., and Shi, W. (2014). featureCounts: an efficient general purpose program for assigning sequence reads to genomic features. *Bioinformatics* **30**, 923–930.
104. Ramírez, F., Ryan, D.P., Grüning, B., Bhardwaj, V., Kilpert, F., Richter, A.S., Heyne, S., Dündar, F., and Manke, T. (2016). deepTools2: a next generation web server for deep-sequencing data analysis. *Nucleic Acids Res.* **44**, W160–W165.
105. Love, M.I., Huber, W., and Anders, S. (2014). Moderated estimation of fold change and dispersion for RNA-seq data with DESeq2. *Genome Biol.* **15**, 550.
106. Metsalu, T., and Vilo, J. (2015). ClustVis: a web tool for visualizing clustering of multivariate data using principal component analysis and heatmap. *Nucleic Acids Res.* **43**, W566–W570.
107. Wickham, H., and Grolemund, G. (2016). R for data science: import, tidy, transform, visualize, and model data ("O'Reilly Media, Inc.").
108. Yang, Z. (2007). PAML 4: phylogenetic analysis by maximum likelihood. *Mol. Biol. Evol.* **24**, 1586–1591.
109. Kent, W.J., Zweig, A.S., Barber, G., Hinrichs, A.S., and Karolchik, D. (2010). BigWig and BigBed: enabling browsing of large distributed datasets. *Bioinformatics* **26**, 2204–2207.
110. Xie, Z., Bailey, A., Kuleshov, M.V., Clarke, D.J.B., Evangelista, J.E., Jenkins, S.L., Lachmann, A., Wojciechowski, M.L., Kropiwnicki, E., Jagodnik, K.M., et al. (2021). Gene set knowledge discovery with enrichr. *Curr. Protoc.* **1**, e90.
111. Shannon, P., Markiel, A., Ozier, O., Baliga, N.S., Wang, J.T., Ramage, D., Amin, N., Schwikowski, B., and Ideker, T. (2003). Cytoscape: a software environment for integrated models of biomolecular interaction networks. *Genome Res.* **13**, 2498–2504.
112. Wood, D.E., Lu, J., and Langmead, B. (2019). Improved metagenomic analysis with Kraken 2. *Genome Biol.* **20**, 257.
113. Wu, T.D., and Nacu, S. (2010). Fast and SNP-tolerant detection of complex variants and splicing in short reads. *Bioinformatics* **26**, 873–881.
114. Krueger, F., and Andrews, S.R. (2012). Quality Control, Trimming and Alignment of Bisulfite-Seq Data (Prot 57) (Department of Medicine, Hematology and Oncology).
115. Pertea, M., Pertea, G.M., Antonescu, C.M., Chang, T.C., Mendell, J.T., and Salzberg, S.L. (2015). StringTie enables improved reconstruction of a transcriptome from RNA-seq reads. *Nat. Biotechnol.* **33**, 290–295.
116. Grabherr, M.G., Haas, B.J., Yassour, M., Levin, J.Z., Thompson, D.A., Amit, I., Adiconis, X., Fan, L., Raychowdhury, R., Zeng, Q., et al. (2011). Trinity: reconstructing a full-length transcriptome without a genome from RNA-Seq data. *Nat. Biotechnol.* **29**, 644–652.
117. Altschul, S.F., Gish, W., Miller, W., Myers, E.W., and Lipman, D.J. (1990). Basic local alignment search tool. *J. Mol. Biol.* **215**, 403–410.
118. Camacho, C., Coulouris, G., Avagyan, V., Ma, N., Papadopoulos, J., Bealer, K., and Madden, T.L. (2009). Blast+: architecture and applications. *BMC Bioinformatics* **10**, 421.
119. Huang, Z., Whelan, C.V., Foley, N.M., Jebb, D., Touzalin, F., Petit, E.J., Puechmaile, S.J., and Teeling, E.C. (2019). Longitudinal comparative transcriptomics reveals unique mechanisms underlying extended health-span in bats. *Nat. Ecol. Evol.* **3**, 1110–1120.
120. Ewels, P., Magnusson, M., Lundin, S., and Käller, M. (2016). MultiQC: summarize analysis results for multiple tools and samples in a single report. *Bioinformatics* **32**, 3047–3048.
121. Zhang, Y., Lin, Y.H., Johnson, T.D., Rozek, L.S., and Sartor, M.A. (2014). PePr: a peak-calling prioritization pipeline to identify consistent or differential peaks from replicated ChIP-Seq data. *Bioinformatics* **30**, 2568–2575.
122. Anders, S., and Huber, W. (2010). Differential expression analysis for sequence count data. *Genome Biol.* **11**, R106.
123. Carlson, C.J., Gibb, R.J., Albery, G.F., Brierley, L., Connor, R.P., Dallas, T.A., Eskew, E.A., Fagre, A.C., Farrell, M.J., Frank, H.K., et al. (2022). The Global Virome in One Network (virion): an atlas of vertebrate-virus associations. *mBio* **13**. e02985-02921.

## STAR★METHODS

### KEY RESOURCES TABLE

REAGENT or RESOURCE	SOURCE	IDENTIFIER
<b>Antibodies</b>		
anti-Afp	R&D Systems	AF1369; RRID:AB_354758
anti-Pax6	BioLegend	901301; RRID:AB_2565003
J2 anti-dsRNA	Scicons	10010200; RRID:AB_2651015
anti-(gag/pol)HERVK	Austrial Biological	HERM18315; RRID:AB_10890594
anti-Pan Corona FIPV3-70	Life Technologies	MA1-82189; RRID:AB_930177
anti-Oct3/4-AF488	Santa Cruz	sc-5279-AF488; RRID:AB_628051
anti-Brachyury	R&D Systems	IC2085G;RRID:AB_2933975
anti-Otx2	R&D Systems	AF1979; RRID:AB_2157172
anti-Zic2	Abcam	ab150404; RRID:AB_2868423
anti-Tfe3	Sigma Aldrich	HPA023881; RID:AB_1857931
anti-Tfcp2l1	R&D Systems	AF5726; RRID:AB_2202564
anti-Cdx2	Invitrogen	PA5-20891; RRID:AB_11155394
Donkey anti-chicken-Cy3	Millipore	AP194C; RRID:AB_92679
Goat anti-chicken-AF488	Invitrogen	A-11039; RRID:AB_2534096
Donkey anti-rabbit-AF647	Invitrogen	A-31573; RRID:AB_2536183
Goat anti-rabbit-AF488	Invitrogen	A-10034; RRID:AB_2576217
Goat anti-mouse-AF488	Invitrogen	A-11029; RRID:AB_2534088
Abberior Star 635P	Abberior	ST635P; RRID:AB_2893232
H3K4me3	Active Motif	39159; RRID:AB_2615077
H3K27me3	Active Motif	39155; RRID:AB_2561020
anti-mouse-HRP	Promega	W4021; RRID:AB_430834
<b>Bacterial and virus strains</b>		
SARS-CoV-2, isolate USA-WA1/2020	BEI Resources	NR-52281
Human Metapneumovirus MPV-GFP1	ViraTree	M121
<b>Chemicals, peptides, and recombinant proteins</b>		
DPBS (Life Technologies, 14190144),	Gibco	14190144
DPBS	Biowest	L0615-500
0.05% Trypsin	Gibco	25300054
DMEM	Gibco	10569010
DMEM	Gibco	11995065
Fetal bovine serum, FBS	Sigma-Aldrich	F4135
Fetal bovine serum, FBS	Gibco	10500064
MEM Non-essential amino	Gibco	11140050
GlutaMax Supplement	Gibco	35050061
Penicillin-Streptomycin solution	Gibco	15140122
Gelatin	Millipore	ES006B
Antibiotic-Antimycotic (100X)	Gibco	15240096
Collagenase type II	Gibco	17101015
Gentle Cell Dissociation Reagent	StemCell Technologies	07174
DMEM/F-12	Gibco	11330057
Knockout serum replacement	Gibco	10828-028
DMSO	Sigma-Aldrich	D8418-100ML
2-mercaptoethanol	Fluka	63689
FGF2	R&D Systems	233-FB

(Continued on next page)

**Continued**

REAGENT or RESOURCE	SOURCE	IDENTIFIER
Leukemia inhibitory factor	Millipore	ESG1107
SCF	R&D Systems	PHC2111
Forskolin	Sigma-Aldrich	F6886
KaryoMAX Colcemid Solution in HBSS	Gibco	15210040
Sodium Pyruvate, 100 mM	Gibco	11360070
Potassium chloride	Sigma-Aldrich	P9327
Glacial acetic	Fisher Scientific	A38-212
Methanol	Sigma-Aldrich	A412-4
KaryoMax Giemsa staining solution	Gibco	10092013
Gurr buffer tablets	Gibcco	10582013
Cytoseal 60	Thermo Scientific	23-244257
SuperScript IV VILO™ Master Mix	Invitrogen	11756050
GoTaq Green Polymerase	Promega	M7123
Cytofix/Cytoperm solution	Becton Dickinson	BDB554714
NucBlue Dapi stain	Invitrogen	R37606
Prolong Dimond antifade mounting medium	Invitrogen	P36965
DyeCycle Violet stain	Invitrogen	V35003
DNase	Qiagen	79254
Formaldehyde	Sigma-Aldrich	F8775
Sodium chloride solution, 5M	Sigma-Aldrich	S5150
EDTA (0.5 M), pH 8.0, RNase-free	Invitrogen	AM9260G
HEPES, 1M	Invitrogen	15630080
Glycine	Sigma-Aldrich	G8898
Igepal	Sigma-Aldrich	I3021
PMSF	Sigma-Aldrich	P7626
mTeSR medium	StemCell Technologies	85850
Vitronectin	StemCell Technologies	07180
BMP4	R&D Systems	314-BP-010
Versene	Gibco	15040066
10% Formalin	Fisher Scientific	SF1004
RIPA lysis and extraction buffer	Fisher Scientific	89900
Proteinase Inhibitor	Roche	45582400
BCA Protein assay kit	Pierce	23252
12% TGX Precast gel	Bio-Rad	4561044
TGS buffer	Bio-Rad	1610772
the Precision Plus Kaleidoscope Protein standard	Bio-Rad	161-3075
EveryBlot blocking buffer	Bio-Rad	12010020
Tris-buffered saline	Fisher Scientific	BP2471500
Tween 20	Bio-Rad	161-0781
Clarity Western ECL Substrate	Bio-Rad	170-5060
Paraformaldehyde	Electron Microscopy Sciences	19200
Glutaraldehyde	Electron Microscopy Sciences	16220
Sodium Cacodylate Buffer	Electron Microscopy Sciences	11652
Aqueous osmium tetroxide	Sigma-Aldrich	75633-2ML
2% aqueous uranyl acetate	Electron Microscopy Sciences	22400-2
Ethanol	Electron Microscopy Sciences	15055
Epoxy resin EMBED 812	Electron Microscopy Sciences	14900
Toluidine Blue	Electron Microscopy Sciences	26074-15
Lead citrate	Electron Microscopy Sciences	22410
Minimum Essential Medium	Gibco	11935046

(Continued on next page)

**Continued**

REAGENT or RESOURCE	SOURCE	IDENTIFIER
4 mM L-glutamine	Gibco	25030081
0.7% agar	Fisher Scientific	AAJ1090722
TrueBlue substrate	Seracare	5510-0030
Trizol reagent	Invitrogen	15596018
Bovine Serum Albumin	Sigma-Aldrich	A2153-50G

**Critical commercial assays**

CytoTune iPS 2.0, Invitrogen, A16517	Life Technologies	A16517
STEMdiff Trilineage differentiation kit	StemCell Technologies	05230
QuickTiter Retrovirus Quantitation Kit	Cell Biolabs	VPK-120
Colorimetric reverse transcriptase kit	Roche	11468120910
SMART-Seq v4 Ultra Low Input kit	Takara Bio	634888
Total RNA with Ribo-Zero Plus kit	Illumina	20040529
AllPrep DNA/RNA Mini Kit	Qiagen	80204
SMRTbell Express Template Preparation Kit v2.0	PacBio	100-938-900
NEBNext Single Cell/Low Input cDNA Synthesis & Amplification Module	New England Biolabs	E6421L
SMRTbell Enzyme Clean Up Kit	PacBio	101-746-400
RNeasy Mini Kit	Qiagen	74104

**Deposited data**

<i>Rhinolophus ferrumequinum</i> assembled and annotated by the Vertebrate Genomes Project	Vertebrate Genome Project	GCF_004115265.1
<i>Rhinolophus ferrumequinum</i> genome assembled and annotated by the Bat1K project	Bat1K	GCA_014108255.1
<i>Rhinolophus ferrumequinum</i> genome, Ensembl annotation version 102	Ensembl	GCA_004115265.2
Bat1K annotation of known endogenous retroviruses (ERVs) for <i>R. ferrumequinum</i>	<a href="https://genome.senckenberg.de/">https://genome.senckenberg.de/</a>	N/A
Bat1K annotation of known endogenous retroviruses (ERVs) for <i>Myotis myotis</i>	<a href="https://genome.senckenberg.de/">https://genome.senckenberg.de/</a>	N/A
RFe_BEF-R1_RNA: <i>R. ferrumequinum</i> fibroblasts RNA-seq replicate 1	This paper	GEO: GSE221965
RFe_BEF-R2_RNA: <i>R. ferrumequinum</i> fibroblasts RNA-seq replicate 2	This paper	GEO: GSE221965
RFe_BEF-R3_RNA: <i>R. ferrumequinum</i> fibroblasts RNA-seq replicate 3	This paper	GEO: GSE221965
RFe_BiPS1-R1_RNA: <i>R. ferrumequinum</i> iPS#1 RNA-seq replicate 1	This paper	GEO: GSE221965
RFe_BiPS1-R2_RNA: <i>R. ferrumequinum</i> iPS#1 RNA-seq replicate 2	This paper	GEO: GSE221965
RFe_BiPS1-R3_RNA: <i>R. ferrumequinum</i> iPS#1 RNA-seq replicate 3	This paper	GEO: GSE221965
RFe_BiPS2-R1_RNA: <i>R. ferrumequinum</i> iPS#2 RNA-seq replicate 1	This paper	GEO: GSE221965
RFe_BiPS2-R2_RNA: <i>R. ferrumequinum</i> iPS#2 RNA-seq replicate 2	This paper	GEO: GSE221965
RFe_BiPS2-R3_RNA: <i>R. ferrumequinum</i> iPS#2 RNA-seq replicate 3	This paper	GEO: GSE221965
RFe_BiPS2-EB-R1_RNA: <i>R. ferrumequinum</i> EB RNA-seq replicate 1	This paper	GEO: GSE221965
RFe_BiPS2-EB-R2_RNA: <i>R. ferrumequinum</i> EB RNA-seq replicate 2	This paper	GEO: GSE221965

(Continued on next page)

**Continued**

REAGENT or RESOURCE	SOURCE	IDENTIFIER
RFe_BiPS2-EB-R3_RNA: <i>R. ferrumequinum</i> EB RNA-seq replicate 3	This paper	GEO: GSE221965
RFe_BiPS2-EN-R1_RNA: <i>R. ferrumequinum</i> Endoderm RNA-seq replicate 1	This paper	GEO: GSE221965
RFe_BiPS2-EN-R2_RNA: <i>R. ferrumequinum</i> Endoderm RNA-seq replicate 2	This paper	GEO: GSE221965
RFe_BiPS2-EN-R3_RNA: <i>R. ferrumequinum</i> Endoderm RNA-seq replicate 3	This paper	GEO: GSE221965
RFe_BiPS2-ME-R1_RNA: <i>R. ferrumequinum</i> Mesoderm RNA-seq replicate 1	This paper	GEO: GSE221965
RFe_BiPS2-MS-R2_RNA: <i>R. ferrumequinum</i> Mesoderm RNA-seq replicate 2	This paper	GEO: GSE221965
RFe_BiPS2-MS-R3_RNA: <i>R. ferrumequinum</i> Mesoderm RNA-seq replicate 3	This paper	GEO: GSE221965
RFe_BiPS2-EC-R1_RNA: <i>R. ferrumequinum</i> Ectoderm RNA-seq replicate 1	This paper	GEO: GSE221965
RFe_BiPS2-EC-R2_RNA: <i>R. ferrumequinum</i> Ectoderm RNA-seq replicate 2	This paper	GEO: GSE221965
RFe_BiPS2-EC-R3_RNA: <i>R. ferrumequinum</i> Ectoderm RNA-seq replicate 3	This paper	GEO: GSE221965
RFe_BEF-R1_ATAC: <i>R. ferrumequinum</i> fibroblasts ATAC-seq replicate 1	This paper	GEO: GSE221965
RFe_BEF-R2_ATAC: <i>R. ferrumequinum</i> fibroblasts ATAC-seq replicate 2	This paper	GEO: GSE221965
RFe_BiPS2-R1_ATAC: <i>R. ferrumequinum</i> iPS#2 ATAC-seq replicate 1	This paper	GEO: GSE221965
RFe_BiPS2-R2_ATAC: <i>R. ferrumequinum</i> iPS #2 ATAC-seq replicate 2	This paper	GEO: GSE221965
RFe_BEF_H3K4: <i>R. ferrumequinum</i> fibroblasts H3K4me3 ChIP-seq	This paper	GEO: GSE221965
RFe_BiPS2_H3K4: <i>R. ferrumequinum</i> iPS H3K4me3 ChIP-seq	This paper	GEO: GSE221965
RFe_BEF_H3K27: <i>R. ferrumequinum</i> fibroblasts H3K4me3 ChIP-seq	This paper	GEO: GSE221965
RFe_BiPS2_H3K27: <i>R. ferrumequinum</i> iPS#2 H3K4me3 ChIP-seq	This paper	GEO: GSE221965
RFe_BEF-R1: RRBS: <i>R. ferrumequinum</i> fibroblasts RRBS replicate 1	This paper	GEO: GSE221965
RFe_BEF-R2: RRBS: <i>R. ferrumequinum</i> fibroblasts RRBS replicate 2	This paper	GEO: GSE221965
RFe_BiPS2-R1_RRBS: <i>R. ferrumequinum</i> iPS#2 RRBS replicate 1	This paper	GEO: GSE221965
RFe_BiPS2-R2_RRBS: <i>R. ferrumequinum</i> iPS#2 RRBS replicate 2	This paper	GEO: GSE221965
Dog iPS RNAseq: K9_1_iPS_P9	GSE152493 <sup>95</sup>	GEO: GSM4616525
Dog iPS RNAseq: K9_2_iPS_P8	GSE152493 <sup>95</sup>	GEO: GSM4616526
Dog iPS RNAseq: K9_3_iPS_P8	GSE152493 <sup>95</sup>	GEO: GSM4616527
Marmoset iPS RNAseq: CM421F_B0_12_iPS_P11	GSE152493 <sup>95</sup>	GEO: GSM4617887
Marmoset iPS RNAseq: CTXNS1_B1_iPS_P7	GSE152493 <sup>95</sup>	GEO: GSM4617889
Marmoset iPS RNAseq: CTXNS2_B1_iPS_P5	GSE152493 <sup>95</sup>	GEO: GSM4617890
Marmoset iPS RNAseq: E01F_A2_2_iPS_P10	GSE152493 <sup>95</sup>	GEO: GSM4617891
Marmoset iPS RNAseq: E02M_B0_7_iPS_P13	GSE152493 <sup>95</sup>	GEO: GSM4617895
Marmoset iPS RNAseq: I5061F_B3_15_iPS_P10	GSE152493 <sup>95</sup>	GEO: GSM4617900

(Continued on next page)

**Continued**

REAGENT or RESOURCE	SOURCE	IDENTIFIER
Marmoset iPS RNA-seq: I5061F_B3_3_iPS_P11	GSE152493 <sup>95</sup>	GEO: GSM4617901
Human iPS RNA-seq: BjiPS_P3	GSE152493 <sup>95</sup>	GEO: GSM4616532
Pig iPS cell RNA-seq: N01F_N1_iPS_P3	GSE152493 <sup>95</sup>	GEO: GSM4616535
Pig iPS cell RNA-seq: N01F_N2_iPS_P3	GSE152493 <sup>95</sup>	GEO: GSM4616536
Mouse ES cell RNA-seq: WT ESC -1	GSE53212 <sup>96</sup>	GEO: GSM1287734
Mouse ES cell RNA-seq: WT ESC -2	GSE53212 <sup>96</sup>	GEO: GSM1287735
Mouse ES cell RNA-seq: WT ESC -3	GSE53212 <sup>96</sup>	GEO: GSM1287745
Mouse ES cell RNA-seq: WT ESC -4	GSE53212 <sup>96</sup>	GEO: GSM1287746
Mouse ES cell RNA-seq: iPSC -1	GSE53212 <sup>96</sup>	GEO: GSM1287736
Mouse iPS cell RNA-seq: WT iPSC -2	GSE53212 <sup>96</sup>	GEO: GSM1287747
Mouse iPS cell RNA-seq: WT iPSC -3	GSE53212 <sup>96</sup>	GEO: GSM1287748
Mouse fibroblasts RNA-seq: WT MEFs -1	GSE53212 <sup>96</sup>	GEO: GSM1287749
Mouse fibroblasts RNA-seq: WT MEFs -2	GSE53212 <sup>96</sup>	GEO: GSM1287750
Human naïve ES cell RNA-seq: Naive_Ex1	GSE144994 <sup>97</sup>	GEO: GSM4303994
Human naïve ES cell RNA-seq: Naive_Ex2	GSE144994 <sup>97</sup>	GEO: GSM4303995
Human primed ES cell RNA-seq: Primed_Ex1	GSE144994 <sup>97</sup>	GEO: GSM4304018
Human primed ES cell RNA-seq: Primed_Ex2	GSE144994 <sup>97</sup>	GEO: GSM4304019
Human H9 ES cells RNA-seq: H9.WT.1.1_RNA-seq	GSE140997 <sup>98</sup>	GEO: GSM4192140
Human H9 ES cells RNA-seq: H9.WT.1.2_RNA-seq	GSE140997 <sup>98</sup>	GEO: GSM4192141

**Experimental models: Cell lines**

<i>Rhinolophus ferrumequinum</i> embryonic fibroblasts	This paper	BEF
<i>Rhinolophus ferrumequinum</i> induced pluripotent stem cells clone 1	This paper	RFe.iPS#1(BiPS1)
<i>Rhinolophus ferrumequinum</i> induced pluripotent stem cells clone 2	This paper	RFe.iPS2 (BiPS#2)
<i>Myotis myotis</i> uropatagium fibroblasts	This paper	MMy.BUF
<i>Myotis myotis</i> induced pluripotent stem cells	This paper	MMy.iPS
293FT cells	Life Technologies	R700-07
NIH/3T3 cells	ATCC	CRL-1658
R1 mouse ES cells	ATCC	SCRC-1011
H9 human ES cells	WiCell	WA09
Vero-E6	ATCC	CRL-1587
Irradiated CF1 mouse fibroblasts	Gibco	A34181

**Experimental models: Organisms/strains**

8-week-old male Fox Chase SCID Beige Mice	Charles River	250
---	---------------	-----

**Oligonucleotides**

SeV-F: GGATCACTAGGTGATATCGAGC	CytoTune 2.0	N/A
SeV-R: ACCAGACAAGAGTTTAAGAGATATGTATC	CytoTune 2.0	N/A
KOS-F: ATGCACCGCTACGACGTGAGCGC	CytoTune 2.0	N/A
KOS-R: ACCTTGACAATCCTGATGTGG	CytoTune 2.0	N/A
Klf4-F TTCCTGCATGCCAGAGGAGCCC	CytoTune 2.0	N/A
Klf4-R: AATGTATCGAAGGTGCTCAA	CytoTune 2.0	N/A
cMyc-F: TAACTGACTAGCAGGCTTGTCG	CytoTune 2.0	N/A
cMyc-R: TCCACATACAGTCCTGGATGATGATG	CytoTune 2.0	N/A
GAPDH_F1_GHB: TGGTGAAGGTCGGAGTGAAC	This paper	Z25-132
GAPDH_R1_GHB: GAAGGGGTCATTGATGGCGA	This paper	Z25-133

(Continued on next page)

**Continued**

REAGENT or RESOURCE	SOURCE	IDENTIFIER
<b>Software and algorithms</b>		
FastQC v0.11.9	Andrews et al. <sup>99</sup>	<a href="https://www.bioinformatics.babraham.ac.uk/projects/fastqc/">https://www.bioinformatics.babraham.ac.uk/projects/fastqc/</a>
Trimmomatic v0.39	Bolger et al. <sup>100</sup>	<a href="http://www.usadellab.org/cms/?page=trimmomatic">http://www.usadellab.org/cms/?page=trimmomatic</a>
HISAT2 v2.2.1	Kim et al. <sup>101</sup>	<a href="http://daehwankimlab.github.io/hisat2/">http://daehwankimlab.github.io/hisat2/</a>
SAMtools v1.10	Li et al. <sup>102</sup>	<a href="https://github.com/samtools/samtools/releases/">https://github.com/samtools/samtools/releases/</a>
featureCounts v2.0.1	Liao et al. <sup>103</sup>	<a href="https://subread.sourceforge.net/">https://subread.sourceforge.net/</a>
deepTools	Ramírez et al. <sup>104</sup>	<a href="https://deeptools.readthedocs.io/en/develop/content/tools/bamCoverage.html">https://deeptools.readthedocs.io/en/develop/content/tools/bamCoverage.html</a>
DESeq2 v1.10.1	Love et al. <sup>105</sup>	<a href="https://bioconductor.org/packages/release/bioc/html/DESeq2.html">https://bioconductor.org/packages/release/bioc/html/DESeq2.html</a>
ClustVis (Beta)	Metsalu and Vilo <sup>106</sup>	<a href="https://biit.cs.ut.ee/clustvis/">https://biit.cs.ut.ee/clustvis/</a>
R package ggpubr	Wickham and Grolemund <sup>107</sup>	<a href="https://cran.r-project.org/web/packages/ggpubr/index.html">https://cran.r-project.org/web/packages/ggpubr/index.html</a>
ggplot2	Wickham and Grolemund <sup>107</sup>	<a href="https://cran.r-project.org/web/packages/ggplot2/index.html">cran.r-project.org/web/packages/ggplot2/index.html</a>
ggmaplot	Wickham and Grolemund <sup>107</sup>	<a href="https://rpkgs.datanovia.com/ggpubr/reference/ggmaplot.html">https://rpkgs.datanovia.com/ggpubr/reference/ggmaplot.html</a>
ggscatter	Wickham and Grolemund <sup>107</sup>	<a href="https://rpkgs.datanovia.com/ggpubr/reference/ggscatter.html">https://rpkgs.datanovia.com/ggpubr/reference/ggscatter.html</a>
codeml package of the PAML suite software	Yang et al. <sup>108</sup>	<a href="http://abacus.gene.ucl.ac.uk/software/paml.html">http://abacus.gene.ucl.ac.uk/software/paml.html</a>
bedGraphToBigWig v4	Kent et al. <sup>109</sup>	<a href="https://www.encodeproject.org/software/bedgraph-tobigwig/">https://www.encodeproject.org/software/bedgraph-tobigwig/</a>
Enrichr	Xie et al. <sup>110</sup>	<a href="https://maayanlab.cloud/Enrichr/">maayanlab.cloud/Enrichr/</a>
Cytoscape Version 3.8.2	Shannon et al. <sup>111</sup>	<a href="https://cytoscape.org">https://cytoscape.org</a>
SMRTLink version 10.1	PacBio	<a href="https://www.pacb.com/support/software-downloads/">https://www.pacb.com/support/software-downloads/</a>
Kraken2 v2.1.2	Wood et al. <sup>112</sup>	<a href="https://github.com/DerrickWood/kraken2">https://github.com/DerrickWood/kraken2</a>
gmap/gsnap	Wu et al. <sup>113</sup>	<a href="http://research-pub.gene.com/gmap">http://research-pub.gene.com/gmap</a>
Trimmalore v0.6.6	GitHub, Open Source	<a href="https://github.com/FelixKrueger/TrimGalore">https://github.com/FelixKrueger/TrimGalore</a>
Cutadapt	Krueger n.d. Andrews <sup>114</sup>	<a href="https://github.com/marcelm/cutadapt">https://github.com/marcelm/cutadapt</a>
stringTie v2.2.1	Pertea et al. <sup>115</sup>	<a href="http://ccb.jhu.edu/software/stringtie/index.shtml?t=manual">http://ccb.jhu.edu/software/stringtie/index.shtml?t=manual</a>
Seqtk v1.3	GitHub, Open Source	<a href="https://github.com/lh3/seqtk">https://github.com/lh3/seqtk</a>
Trinity v2.12	Grabbherr et al. <sup>116</sup>	<a href="https://github.com/trinityrnaseq/trinityrnaseq/releases/tag/v2.12.0">https://github.com/trinityrnaseq/trinityrnaseq/releases/tag/v2.12.0</a>
BLAST	Altschul et al. <sup>117</sup> Camacho <sup>118</sup>	<a href="https://blast.ncbi.nlm.nih.gov/Blast.cgi">https://blast.ncbi.nlm.nih.gov/Blast.cgi</a>
SQUID	Eddy Lab, Harvard University	<a href="http://eddylib.org/software.html">http://eddylib.org/software.html</a>
INSPIRE 2.0	Luminex	<a href="https://www.luminexcorp.com">https://www.luminexcorp.com</a>
IDEAS 6.2	Luminex	<a href="https://www.luminexcorp.com">https://www.luminexcorp.com</a>
<b>Other</b>		
ATAC-seq service	Active Motif	25079
RRBS Service, Active Motif,	Active Motif	25069
HistoPath ChIP-seq service,	Active Motif	25001

## RESOURCE AVAILABILITY

### Lead contact

Further information and requests for resources and reagents should be directed to and will be fulfilled by the lead contact, Thomas P. Zwaka ([thomas.zwaka@mssm.edu](mailto:thomas.zwaka@mssm.edu)).

### Materials availability

All unique reagents in this study are available from the [Lead Contact](#) and will be provided upon request. There are restrictions to the availability of frozen cell vials due to the number of frozen stocks available.

### Data and code availability

- All high-throughput sequencing data have been deposited at GEO and are publicly available as of the date of publication. Accession numbers are listed in the [key resources table](#).
- This paper analyzes existing, publicly available data. These accession numbers for the datasets are listed in the [key resources table](#).
- This paper does not report any original code.
- All software packages and their accessibility are described in the [STAR Methods](#) sections.
- Any additional information required to reanalyze the data reported in this paper (including the BLAST results related to [Figures S5–S7](#)) is available from the [lead contact](#) upon request.

## EXPERIMENTAL MODEL AND SUBJECT DETAILS

### Bats

#### *Bat embryonic fibroblast isolation*

A pregnant female bat of the species *Rhinolophus ferrumequinum* was captured with a hand-net in a roost near Jerez de la Frontera, Cádiz, Southern Spain in May 2020. Following the guidelines of the American Society of Mammalogists (2016) and with the approval of the Spanish bio-ethical authority and Andalusian regional government, the bat was euthanized by cervical dislocation and different tissues and the fetus were preserved in RPMI medium at 4°C till the processing of the samples 25 h later. In the lab, the female embryo (approximately developmental stage 20) acquired from a Spanish *Rhinolophus ferrumequinum* (RFe) was cut into several pieces while removing the head and as much of the inner organ tissue as possible. The pieces were then flushed with DPBS (Life Technologies, 14190144), and processed separately. The tissue was covered with 0.05% trypsin-EDTA (Life Technologies, 25300-120), minced with a scalpel, and incubated in a cell culture incubator at 37°C and 5% CO<sub>2</sub> for 45 minutes. The trypsin was deactivated with fibroblast medium consisting of DMEM (Life Technologies, 10569-010), 10% fetal bovine serum (Sigma, F4135), 0.1 mM MEM Non-essential amino acids (Life Technologies, 11140-050), 2 mM GlutaMax supplement (Life Technologies, 35050061) and Penicillin-Streptomycin (10 U/ml and 10 µg/ml, respectively: Life Technologies, 15140122). The RFe cells were broken up by pipetting up and down 20 times, collected by centrifugation, transferred to a gelatin-coated (Sigma-Aldrich, G1890) T75 cell culture-treated flasks (Falcon, 353136) in 15 ml of fibroblast medium, and cultured at 37°C and 5% CO<sub>2</sub>. After 3 days, when reaching ~80% confluency, the attached RFe cells were washed with DPBS (Life Technologies, 14190144), treated with 0.05% trypsin-EDTA (Life Technologies, 25300120) to obtain a single cell solution and either split at a ratio of 1:4 or used directly in a reprogramming experiment.

#### *Myotis myotis sampling and isolation of fibroblasts from tail biopsies*

*M. myotis* (MMy) were sampled in Morbihan, Brittany in North-West France, July 2021 in accordance with the permits and ethical guidelines issued by 'Arrêté' by the Préfet du Morbihan and the University College Dublin ethics committee. This population has been transponded and followed since 2010 as part of on-going mark-recapture studies by Bretagne Vivante and the Teeling laboratory.<sup>119</sup> Once captured, all bats were placed in individual cloth bags before processing. A single 3 mm biopsy was taken from the outstretched uropatagium of each bat using a sterile biopsy punch and immediately submerged in a cryotube (Sarstedt, 72.379) with 2 ml of DMEM cell culture medium (Gibco, 11995-065) supplemented with 20% FBS (Gibco, 10500064), 1% NEAA (Gibco, 11140050) and 1% Antibiotic-Antimycotic containing Streptomycin, Amphotericin B and Penicillin (Gibco, 15240096), maintaining as sterile conditions as possible. All bats were offered food and water and rapidly released after processing. Biopsies were then stored at 4°C and transported to the laboratory for processing within 6 days. Samples were further processed through a cell extraction methodology similar to a previously established protocol<sup>35</sup> with a few modifications. The samples were rinsed with DPBS (Biowest, L0615-500) and cut finely within a minimal amount of cell culture medium using sterile blades (Swann-Morton, 0208) to result in six 0.5 mm pieces. These pieces were then transferred aseptically to a cryotube containing cell culture medium and incubated for 18 hours with collagenase type II (Life Technologies, 17101-015) at 37°C with 5% CO<sub>2</sub> to allow for digestion. The pieces were collected by centrifugation for 5 minutes at 300 rcf, resuspended in 2 ml of fresh cell culture medium and transferred to a 35 mm cell culture treated plate (Corning, CLS430165) for initial P1 expansion. MMy cells were then fed every 2–3 days with cell culture medium as stated but a reduced 0.2% concentration of Antibiotic-Antimycotic. For the first feeding a <sup>2</sup>/<sub>3</sub> media change is performed to avoid sudden changes in antibiotic-antimycotic concentration from 1% to 0.2%. When the MMy cells reached 70% confluency, they were transferred to a T25

(Cellstar, 690175) in cell culture medium after treatment with 0.05% Trypsin (Gibco, 25300054) and were fed every 2-3 days as necessary. At 85% confluency, the MMy cells were trypsinized as before and  $1 \times 10^6$  cells were frozen in 1 ml cell culture medium containing 10% DMSO (Sigma, D8418-100ML) within a cryotube through the use of a cell freezer (Thermo Scientific, 5100-0036) placed overnight in a  $-80^\circ\text{C}$  freezer with subsequent transfer to long term storage in liquid nitrogen at  $-150^\circ\text{C}$ . The particular MMy fibroblasts used in this study were isolated from one female bat.

### Cell lines

293FT cells (Invitrogen, R700-07) embryonal kidney cells were cultured in DMEM (Gibco, 10569010) supplemented with 10% FBS (Sigma, F4135), 0.1 mM MEM Non-essential amino acids (Gibco, 11140-050), 2 mM GlutaMax supplement (Gibco, 35050-061), 1 mM Sodium Pyruvate (Gibco, 11360070) and Penicillin-Streptomycin (10 U/ml and 10  $\mu\text{g}/\text{ml}$ , respectively; Gibco, 15140122). NIH/3T3 cells (ATCC, CRL-1658) cells were cultured in DMEM (Gibco, 10569010) supplemented with 10% FBS (Sigma, F4135). R1 mouse ES cells were cultured in DMEM (Gibco, 10569010) supplemented with 10% FBS (Sigma, F4135), 0.1 mM MEM Non-essential amino acids (Gibco, 11140-050), 2 mM GlutaMax supplement (Gibco, 35050-061), Penicillin-Streptomycin (10 U/ml and 10  $\mu\text{g}/\text{ml}$ , respectively; Gibco, 15140122), 100  $\mu\text{M}$  2-mercaptoethanol (Fluka, 63689) and 104 U/ml Leukemia inhibitory factor (Millipore, ESG1107) on cell-culture dishes that were pretreated with 0.01% gelatin (Millipore, ES006B). Cell lines were split with 0.05% Trypsin-EDTA (Gibco) if not indicated otherwise. Bat induced pluripotent stem cells were cultured in DMEM/F-12 (Gibco, 11330-057) supplemented with 20% knockout serum replacement (Gibco, 10828-028), 0.1 mM MEM Non-essential amino acids (Gibco, 11140-050), 2 mM GlutaMax supplement (Gibco, 35050-061), Penicillin-Streptomycin (10 U/ml and 10  $\mu\text{g}/\text{ml}$ , respectively; Gibco, 15140122), 100  $\mu\text{M}$  2-mercaptoethanol (Fluka, 63689), 100 ng/ml FGF2 (R&D Systems, 233-FB), 104 U/ml Leukemia inhibitory factor (Millipore, ESG1107), 100 ng/ml SCF (R&D Systems, PHC2111) and 20 nM Forskolin (Sigma, F6886). RFe and MMy iPSCs were cultured on a feeder layer of irradiated mouse embryonic fibroblasts (CF1, Gibco) and passaged with Gentle Cell Dissociation Reagent (GCDR, StemCell Technologies, 07174). After that, cells were passaged approximately every 5 days, or when they were confluent at a ratio of 1:6 to 1:12 on irradiated MEFs. H9 human embryonic stem cells were cultured in mTeSR medium (StemCell Technologies, 85850) on Vitronectin-coated (StemCell Technologies, 07180) cell culture dishes. H9 cells were split with Versene (Gibco, 15040066) at a ratio of 1:16.

### SCID Beige Mice

8-week-old male Fox Chase SCID Beige mice (250) were retrieved from Charles River. All procedures were performed in accordance with protocol IACUC-2013-1433.

## METHOD DETAILS

### Reprogramming of bat fibroblasts

150,000 embryonic *Rhinolophus ferrumequinum* fibroblasts at passage 2, adult *Myotis myotis* at passage 3 were resuspended in 1 ml of fibroblast medium and mixed with Sendai-virus particles containing the reprogramming factors Oct4, Sox2, cMyc and Klf4 (CytoTune iPS 2.0, Invitrogen, A16517) with a final multiplicity of infection (MOI) of 10, 10, 10, 20, respectively. The RFe and MMy cells were plated on one gelatin-coated well of a 6-well plate (10  $\text{cm}^2$ , Corning, 353046) and cultured at  $37^\circ\text{C}$  with 5%  $\text{CO}_2$ . The medium was replaced every 24 hours. 6 days after transduction, the RFe and MMy cells of each well were collected by treatment with 0.05% trypsin-EDTA, seeded at a density of 50,000 cells per 60  $\text{cm}^2$  on irradiated CF1 mouse embryonic fibroblasts (MEFs; Gibco, A34180) in fibroblast medium. After 24 hours, the medium was switched to 50 % fibroblast medium and 50% pluripotent stem cell (PSC) medium consisting of DMEM/F-12 (Life Technologies, 11330-057), 20% knockout serum replacement (Life Technologies, 10828-028), 0.1 mM MEM Non-essential amino acids (Life Technologies, 11140-050), 2 mM GlutaMax supplement (Life Technologies, 35050-061), Penicillin-Streptomycin (10 U/ml and 10  $\mu\text{g}/\text{ml}$ , respectively; Life Technologies, 15140122), 100  $\mu\text{M}$  2-mercaptoethanol (Fluka, 63689), and 40 ng/ml FGF2 (R&D Systems, 233-FB). From then on, the medium was replaced every day with PSC medium until day 14 when the FGF concentration was increased to 100 ng/ml and the medium was supplemented with  $10^4$  U/ml Leukemia inhibitory factor (Millipore, ESG1107), 100 ng/ml SCF (R&D Systems, PHC2111) and 20 nM Forskolin (Sigma, F6886). Colonies appeared 14 to 16 days after transduction, were picked on day 20 and expanded on irradiated MEFs with Gentle Cell Dissociation Reagent (GCDR, StemCell Technologies, 07174). After that, the RFe and MMy cells were passaged approximately every 5 days, or when they were confluent at a ratio of 1:6 to 1:12 on irradiated MEFs. Cell and colony morphology were recorded with an EVOS digital inverted microscope (Invitrogen).

### Karyotyping

RFe iPSCs were treated with 100 ng/ml Colcemid solution (Life Technologies, 15210040) for 16 hours, then treated with 0.05% trypsin-EDTA for 15 minutes and filtered through a 40  $\mu\text{m}$  cell strainer to remove clumps. RFe cells were collected by centrifugation, resuspended in 1 ml 0.075 M potassium chloride (Sigma-Aldrich, P9327) and incubated for 20 minutes at room temperature. 0.5 ml fixative [1 part glacial acetic (Fisher Scientific, A38-212) mixed with 3 parts methanol (Sigma-Aldrich, A412-4)] were added, RFe cells were collected as before, resuspended in 4 ml fixative, and incubated for 20 minutes at room temperature. The fixation step was repeated, the RFe cells collected as before and all but about 200  $\mu\text{l}$  of the fixative was removed. The cells were resuspended in the remaining fixative and dropped onto slides that were precooled at  $-20^\circ\text{C}$ . The slides were airdried and the RFe cells stained for 10 minutes with Giemsa Staining solution consisting of 1 part Giemsa solution (Life Technologies, 10092013), and 3 parts Gurr

buffer (Invitrogen, 10582013). The slides were washed with water, dried, and mounted in Cytoseal 60 (Thermo Scientific, 23-244257). High-resolution pictures of chromosome spreads were acquired with an AxioObserver microscope (Zeiss) using the 100x oil objective.

### RT-PCR

mRNA was extracted with the RNeasy Mini Kit (Qiagen, 74104). 500 ng of each sample were used to generate cDNA by reverse transcription using the SuperScript™ IV VIL0™ Master Mix (Invitrogen, 11756050). 2 μl of the cDNA were used to detect the presence of Sendai virus transcripts using GoTaq Green Polymerase (Promega, M7123), and the oligos as recommended in the CytoTune iPS 2.0 kit (Invitrogen, A16517). Gapdh was amplified as loading control using oligos with the following sequence: Z25-132:GAPDH\_F1\_GHB: TGGTGAAGGTCGGAGTGAAC and Z25-133:GAPDH\_R1\_GHB: GAAGGGGTCA TTGATGGCGA). The PCR products were analyzed on a 2% agarose gel containing ethidium bromide.

### Immunofluorescence staining

RFe and MMy cells were plated on μ-slides (Ibidi, 80286). After 4 days, cells were washed once with DPBS and fixed with Cytofix/Cytoperm solution (Becton Dickinson, BDB554714) for 20 minutes at 4°C. Cells were rinsed with Perm/Wash buffer (Becton Dickinson, BDB554714) and then incubated overnight at 4°C in Perm/Wash buffer containing primary anti-Afp (R&D Systems, AF1369), anti-Pax6 (BioLegend, 901301), J2 anti-dsRNA (Scicons, 10010200), anti-(gag/pol)HERVK (Austrial Biological, HERM18315), FIPV3-70 anti-Pan Corona (Life Technologies, MA1-82189) or directly conjugated anti-Oct3/4-AF488 (Santa Cruz, sc-5279-AF488), anti-Brachyury (R&D Systems, IC2085G), anti-Otx2 (R&D Systems, AF1979), anti-Zic2 (Abcam, ab150404), anti-Tfe3 (Sigma Aldrich, HPA023881), anti-Tfcp2l1 (R&D Systems, AF5726) or anti-Cdx2 (Life Technologies, PA5-20891) in a 1:50 (anti-Oct3/4) or 1:100 dilution (all others). RFe and MMy cells were rinsed and washed 3 times for 2 minutes with Perm/Wash solution at room temperature followed by a 1-hour incubation with a 1:200 dilution of the corresponding secondary antibodies (Donkey anti-chicken-Cy3, Millipore, AP194C; Goat anti-chicken-AF488, Life Technologies, A-11039; Donkey anti-rabbit-AF647, Life Technologies, A-31573; Goat anti-rabbit-AF488, Life Technologies, A-10034; Goat anti-mouse-AF488, Life Technologies, A-11029) in Perm/Wash buffer. RFe and MMy cells were rinsed, washed twice for 2 minutes with Perm/Wash Buffer and then incubated for 5 minutes with Perm/Wash buffer containing 2 drops per ml NucBlue Dapi stain (Invitrogen, R37606). The buffer was removed, and the cells were cover-slipped in Prolong Dimond antifade mounting medium (Invitrogen, P36965). Images were acquired with an AxioObserver fluorescence microscope with Apotome (Zeiss). For the simulated emission depletion (STED) microscopy (super-resolution), the RFe cells were plated on coverslips that were placed in wells of 6-well plates. The staining was performed as described above but with a 1:200 dilution of the Abberior Star 635P (Abberior, ST635P) secondary antibody in Perm/Wash buffer. The RFe cells were rinsed, washed twice for 2 minutes with Perm/Wash Buffer and then incubated for 5 minutes with Perm/Wash buffer containing 2 drops per ml DyeCycle Violet stain (Invitrogen, V35003). The coverslips were mounted face down on glass slides with Prolong Dimond antifade mounting medium (Invitrogen, P36965). Images were acquired with a TCS SP8 confocal microscope with STED 3x and White Light Laser (Leica) with a 100x oil objective. 405 nm and 594 nm lasers were used for excitation and 775 nm laser for depletion. Image resolution obtained was 19.8 μm by 19.8 μm using a zoom factor of 6x.

### RNA-seq, differential expression analyses and visualization

For RNA-seq, RNA was extracted from RFe iPSCs cells at passage 22, RFe BEFs at passage 3, MMy iPSCs at passage 7 and MMy fibroblasts at passage 4. Total RNA was extracted with the RNeasy kit (Qiagen, 74104) following the manufacturer's recommendations including the DNase (Qiagen, 79254) digest, and eluted in 50 μl RNase/DNase free H<sub>2</sub>O. RNA-seq libraries were prepared with the SMART-Seq v4 Ultra Low Input kit (Takara Bio, undifferentiated cells) or the Stranded Total RNA with Ribo-Zero Plus kit (Illumina, differentiated cells) and 100 bp paired-end sequencing reads (PE100) were generated by Illumina sequencing (NovaSeq 6000 S1) to a depth of at least 50 million reads (100 million total reads). The quality of the reads from the RNA sequencing was analysed with FastQC v0.11.9,<sup>99</sup> and visualized using MultiQC v1.9.<sup>120</sup> The mean phred score was around Q35 across each base position in the RFe and BEF and BiPS samples and no filtering or processing was necessary. In the differentiated samples (EB, endoderm, mesoderm, ectoderm differentiation), the quality of the first nucleotide was less than Q20 in many cases and the reads were processed with Trimmomatic v0.39.<sup>100</sup> To carry out the differential expression analysis, the genome of *Rhinolophus ferrumequinum* was used as reference genome (RefSeq accession GCF\_004115265.1 assembled and annotated by the Vertebrate Genomes Project (<https://vertebrategenomesproject.org>) or GenBank accession GCA\_014108255.1 assembled and annotated by the Bat1K project (<https://bat1k.com>) as indicated. The reads were mapped with HISAT2 v2.2.1,<sup>101</sup> the .sam files resulting from each mapping were converted into .bam files and indexed using SAMtools v1.10<sup>102</sup> and the reads mapped against each gene were counted using featureCounts v2.0.1.<sup>103</sup> The differential expression analysis was performed with DESeq2 v1.10.1.<sup>105</sup> To visualize the RNA-seq data in the UCSC genome browser, bigwig files were generated using the bamCoverage command from deepTools (<https://deeptools.readthedocs.io/en/develop/content/tools/bamCoverage.html>).<sup>104</sup>

### MA plot

The MA plots were generated based on the DESeq2 (see above) results with the ggmaplot function (<https://rpkgs.datanovia.com/ggpubr/reference/ggmaplot.html>) from the R package ggpubr (<https://rpkgs.datanovia.com/ggpubr/>).<sup>107</sup> Genes are indicated by

dots, plotted by their  $\log_2$  fold change between RFe bat fibroblast and RFe pluripotent stem cells and the  $\log_2$  mean of normalized counts (ratio of means). Blue dots indicate genes with an adjusted p value of (or FDR) of  $<0.05$  and a fold change of 2 ( $\log_2$  fold change of 1), red dots indicate genes with an adjusted p value (or FDR) of  $<0.05$  and fold change of -2 ( $\log_2$  fold change of -1). Dotted lines are drawn at fold change of 2/-2 ( $\log_2$  fold change of 1/-1).

### Heatmap

The heatmap of pluritest genes, with ClustVis (Beta), a web tool for visualizing clustering of multivariate data (<https://biit.cs.ut.ee/clustvis/>).<sup>106</sup> Rows are centered; unit variance scaling is applied to rows. Both rows and columns are clustered using correlation distance and average linkage.

### ATAC-seq

ATAC-seq and bioinformatics analysis to detect open chromatin in RFe bat fibroblasts and RFe bat pluripotent stem cells was performed by Active Motif from 100,000 cryopreserved cells (ATAC-seq service, 25079). In brief, nuclei were isolated, and libraries of open chromatin were prepared with the Nextera Library Prep Kit (Illumina) by Tn5 tagmentation. The tagmented DNA was purified using the MinElute PCR purification kit (Qiagen), amplified with 10 cycles of PCR, and purified using Agencourt AMPure SPRI beads (Beckman Coulter). 42 bp paired-end sequencing reads (PE42) were generated by Illumina sequencing (using NextSeq 500) to a depth of at least 83 million total reads and mapped to the GCA\_004115265.2 genome (Ensembl, annotation version 102) using the BWA algorithm with default settings (“bwa mem”). Alignment information for each read was stored as BAM file. Only reads that passed the Illumina’s purity filter, aligned with no more than 2 mismatches, and mapped uniquely to the genome were used in the subsequent analysis. Duplicate reads (“PCR duplicates”) are removed. Genomic regions with high levels of transposition/tagging events were then determined using the MACS2 peak calling algorithm.<sup>121</sup> To identify the density of transposition events along the genome, the genome was divided into 32 bp bins and the number of fragments in each bin was determined. The data were then normalized by reducing the tag number of all samples by random sampling to the number of tags present in the smallest sample. Peak metrics between samples were compared by grouping overlapping Intervals into “Merged Regions”, which are defined by the start coordinate of the most upstream Interval and the end coordinate of the most downstream Interval (= union of overlapping Intervals; “merged peaks”). In locations where only one sample has an Interval, this Interval defines the Merged Region. Intervals and Merged Regions, their genomic locations along with their proximities to gene annotations and other genomic features were determined and average and peak (i.e., at “summit”) fragment densities were compiled. The sequencing tracks (number of fragments in each 32 bp bin stored as “.bigWig” file) were visualized with the UCSC genome browser.

### Reduced representation bisulfite sequencing (RRBS)

Reduced representation bisulfite sequencing of RFe bat fibroblasts and pluripotent stem cells was performed by Active Motif (RRBS Service, Active Motif, 25069). Briefly, 500,000 cells were provided as a frozen pellet. Genomic DNA was isolated, and 100 ng were digested with TaqI (NEB R0149) at 65°C for 2 hours followed by MspI (NEB R0106) at 37°C overnight. Following enzymatic digestion, samples were used for library generation with the Ovation RRBS Methyl-Seq System (Tecan, 0353-32) following the manufacturer’s instructions. In brief, digested DNA was randomly ligated, and, following fragment end repair, bisulfite converted using the EpiTect Fast DNA Bisulfite Kit (Qiagen, 59824) following the Qiagen protocol. After conversion and clean-up, samples were amplified resuming the Ovation RRBS Methyl-Seq System protocol for library amplification and purification. 75 bp single-end sequencing reads (SE75) were generated by Illumina sequencing (using NextSeq 500) to a depth of at least 27 million reads (total of 54 million reads), with at least 2.9 million covered CpGs. The reads were mapped to the GCA\_004115265.2 genome (Ensembl, annotation version 102) and the percentage of methylation at CpG sites across the genome was calculated. To visualize the methylation ratios aligned to the genome with the UCSC genome browser, the methylation ratio files containing the methylation ratio for each chromosomal position were first converted to bed files, that were then used to generate bigwig files with the “bedGraphToBigWig v4 tool” (<https://www.encodeproject.org/software/bedgraph/tobigwig/>).<sup>109</sup> Correlation scatter plots were generated to show the level of methylation at common CpG sites.

### Chromatin immunoprecipitation sequencing (ChIP-seq)

5 million RFe iPS cells were fixed cells in 1% formaldehyde by adding 1/10 volume of freshly prepared formaldehyde solution (11% formaldehyde, 0.1 M NaCl, 1 mM EDTA, pH 8.0, 50 mM HEPES, pH 7.9) to the existing medium. The RFe cells were agitated for 15 minutes at room temperature and the fixation was stopped by addition of 1/20 volume of 2.5 M glycine solution (final concentration of 0.125 M) to the existing medium and incubation at room temperature for 5 minutes. The RFe cells were scraped off the wells, collected by centrifugation at 800 g and washed with 10 ml chilled 0.5% Igepal in PBS per tube by pipetting up and down. RFe cells were pelleted by centrifugation as before and resuspended in 10 ml chilled PBS-Igepal containing 1 mM PMSF. RFe cells were collected as before, and the cell pellet was snap-frozen in liquid nitrogen. Further processing, chromatin immunoprecipitation and bioinformatics analysis to detect H3K4me3 and H3K27me3 was performed by Active Motif (HistoPath ChIP-seq service, 25001). In brief, chromatin was isolated by adding lysis buffer, followed by disruption with a dounce homogenizer. Lysates were sonicated and the DNA sheared to an average length of 300-500 bp with an EpiShear probe sonicator (Active Motif, 53051). Genomic DNA (Input) was prepared by treating aliquots of chromatin with RNase, proteinase K and heat for de-crosslinking, followed by SPRI beads

clean up (Beckman Coulter) and quantitation with Clariostar (BMG Labtech). An aliquot of chromatin (20  $\mu$ g) was precleared with pro-tein A agarose beads (Life Technologies). Genomic DNA regions of interest were isolated using 4  $\mu$ g of antibody against H3K4me3 (Active Motif, 39159) or H3K27me3 (Active Motif, 39155). Complexes were washed, eluted from the beads with SDS buffer, and sub-jected to RNase and proteinase K treatment. Crosslinks were reversed by incubation overnight at 65°C, and ChIP DNA was purified by phenol-chloroform extraction and ethanol precipitation. Illumina sequencing libraries were generated from the ChIP and Input DNAs with the standard consecutive enzymatic steps of end-polishing, dA-addition, and adaptor ligation. After a final PCR ampli-fication step, 75-nt single-end (SE75) sequence reads were generated by Illumina sequencing (using NextSeq 500) to a depth of at least 36 million reads per sample and mapped to the GCA\_004115265.2 genome (Ensembl, annotation version 102) using the BWA algorithm with default settings. Duplicate reads were removed, and only uniquely mapped reads (mapping quality  $\geq$  25) were used for further analysis. Alignments were extended in silico at their 3'-ends to a length of 200 bp, which is the average genomic fragment length in the size-selected library and assigned to 32-nt bins along the genome. The resulting histograms (genomic "signal maps") were stored in "bigwig" files. To find peaks, the generic term "Interval" was used to describe genomic regions with local enrichments in tag numbers. Intervals were defined by the chromosome number and a start and end coordinate. Peak locations were determined using the MACS algorithm (v2.1.0) with a cutoff of p-value =  $1e^{-7^{34}}$ . Signal maps and peak locations were used as input data to Active Motifs proprietary analysis program, which creates Excel tables containing detailed information on sample comparison, peak metrics, peak locations and gene annotations. No normalization was performed on the H3K27me3 data, while standard normalization was applied to the H3K4me3 data. The tag number of all samples (within a comparison group) was reduced by random sampling to the number of tags present in the smallest sample. To compare peak metrics between 2 or more samples, overlapping Intervals were grouped into "Merged Regions", which are defined by the start coordinate of the most upstream Interval and the end coordinate of the most downstream Interval (= union of overlapping Intervals; "merged peaks"). In locations where only one sample has an Interval, this Interval defines the Merged Region. The sequencing tracks (number of fragments in each 32 bp bin stored as a "bigwig" file) were visualized with the UCSC genome browser.

### Three germ layer differentiation

The differentiation of RFe and MMy bat pluripotent stem cells was carried out with the STEMdiff Trilineage differentiation kit (StemCell Technologies, 05230) following the manufacturer's protocol. RFe and MMy cells were plated at the desired densities in mTeSR medium (StemCell Technologies, 85850), and plated on Vitronectin-coated (StemCell Technologies, 07180) cell culture plates. After 5 days (endoderm or mesoderm) or 7 days (ectoderm) in culture as directed by the manufacturer. For the ectoderm differentiation, the floating three-dimensional structures were then replated and grown for 4 additional days in fibroblast medium. The RFe and MMy cells were stained with antibodies detecting the appropriate lineage markers as described above or cells were collected (surface area of 10 cm<sup>2</sup> per replicate) for RNA isolation and RNA-seq after addition of 600  $\mu$ l lysis buffer RTL (part of the RNeasy kit; Qiagen, 74104).

### Embryonic body differentiation

RFe bat pluripotent stem cells grown on irradiated mouse embryonic fibroblasts from a total area of 60 cm<sup>2</sup> were washed with PBS, treated for 10 minutes with Gentle Cell Dissociation Reagent (StemCell Technologies, 07174), collected by centrifugation and resuspended in 12 ml differentiation medium consisting of DMEM/F-12 (Life Technologies, 11330-057), 10% fetal bovine serum (Sigma, F4135), 0.1 mM MEM Non-essential amino acids (Life Technologies, 11140-050), 2 mM GlutaMax supplement (Life Technol-ogies, 35050-061), Penicillin-Streptomycin (10 U/ml and 10  $\mu$ g/ml, respectively; Life Technologies, 15140122) and 100  $\mu$ M 2-mercaptoethanol (Fluka, 63689). The RFe cells were then transferred to one uncoated 60 cm<sup>2</sup> petri dish (Corning, 351029). After 3 days in culture, as much as possible of the medium (about 2/3) was carefully exchanged without disturbing and removing the floating EBs that had formed. The floating EBs were collected after 3 more days (total of 6 days) in culture, fixed in Cytifix/Cytoperm fixation buffer (Becton Dickinson, BDB554714) overnight, and then stained with antibodies against as described above to detect differentiation markers of all three germ-layers by immunofluorescence. For RNA isolation and RNA-seq, EBs were formed as described, collected, resuspended in 6 ml differentiation medium, and distributed into three wells of cell-culture treated 6-well plates (10 cm<sup>2</sup> each). After 2 more days in culture, the cells were washed with PBS, lysed with 600  $\mu$ l buffer RTL (part of the RNeasy kit; Qiagen, 74104) and RNA was isolated as described above.

### Blastoid differentiation

RFe iPSCs were harvested and plated as described for the embryonic body formation above. After 3 days in culture, 100 ng/ml BMP4 (R&D Systems, 314-BP-010) were added to the medium. 24 hours later the supernatant was diluted with 2/3 of fresh medium and transferred to two fresh uncoated petri dishes. The medium was exchanged after 3 more days in culture and floating blastoids were harvested 4 days later (total of 12 days of differentiation). The blastoids were fixed in Cytifix/Cytoperm fixation buffer (Becton Dickinson, BDB554714) overnight, and stained as described above to detect the expression of Oct4 and Cdx2 by immunofluores-ence microscopy.

### Teratoma formation

Two 6-well plates (12 wells) of RFe pluripotent stem cells grown on irradiated mouse embryonic fibroblasts were scraped off in 2 ml DMEM/F-12 medium (Life Technologies, 11330-057), collected by centrifugation and resuspended in 500  $\mu$ l DMEM/F-12 medium.

100  $\mu$ l of the cell suspension were injected into the hindleg muscle of 8-week-old male Fox Chase SCID Beige Mice (Charles River, 250). Tumor tissue that had formed after 16 weeks was harvested, fixed in 10% Formalin (Fisher Scientific, SF1004) overnight and then transferred to 70% ethanol. The tissue was submitted to the Pathology Core at the Icahn School of Medicine at Mount Sinai for paraffin embedding and hematoxylin and eosin staining of 5  $\mu$ m sections. Images were acquired with an AxioObserver microscope (Zeiss).

### Western blot analyses

RFe iPSCs were lysed with RIPA lysis and extraction buffer (Fisher Scientific, 89900) containing Proteinase Inhibitor (Roche, 45582400) for 30 minutes on ice, debris was removed by centrifugation and the supernatant was transferred to a new tube. Protein concentration was determined using the BCA Protein assay kit (Pierce, 23252) following the manufacturers recommendation in 96 well format. 20  $\mu$ g of protein isolated from each cell line were separated on a 12% TGX Precast gel (Bio-Rad, 4561044) for 70 minutes at 200 V in TGS buffer (Bio-Rad, 1610772), the Precision Plus Kaleidoscope Protein standard (Bio-Rad, 161-3075) was used as size marker. The protein was transferred to a PVDF membrane (activated with methanol) with 1x TGS Buffer (Bio-Rad, 161-0374) supplemented with 20% methanol using the Turbo blot system (Bio-Rad, 1704150) for 30 minutes at 25 V (1 mA). The membrane was blocked with EveryBlot blocking buffer (Bio-Rad, 12010020) for 30 minutes, and then incubated with the anti-Pan Corona (Invitrogen, MA1-82189) or anti-HERVK(cap)(Austral Biologicals, HERM18315) antibodies in a 1:1000 dilution in EveryBlot blocking buffer for 1-hour. The membrane was washed four times with Tris-buffered saline (Fisher Scientific, BP2471500) supplemented with 0.05% Tween 20 (Bio-Rad, 161-0781) for 5 minutes, incubated with the secondary anti-mouse-HRP antibody in a 1:1000 dilution (Promega, PR-W4021) for 1 hour, and then washed as before. Signals were developed with the Clarity Western ECL Substrate (Bio-Rad, 170-5060) and detected with the ChemiDoc MP Imaging System (Bio-Rad, 170-01402).

### Principal component analysis (PCA)

The DESeq2 output files of the RNA-seq analyses described above were subjected to a Variance Stabilizing Transformation (VST) using within-group-variability<sup>122</sup> to compare the RFe bat pluripotent stem cell transcriptional profile with that of other species. The first two principal components of this result were plotted using the ggscatter function (<https://rpkgs.datanovia.com/ggpubr/reference/ggscatter.html>) from the R package ggpubr (<https://cran.r-project.org/web/packages/ggpubr/index.html>),<sup>107</sup> and the weight of each gene's contribution to the principal components were extracted for PC1 and PC2. The datasets used in the PCA were: GSM4616525, GSM4616526, GSM4616527 (dog iPS), GSM4617887, GSM4617889, GSM4617890, GSM4617891, GSM4617895, GSM4617900, GSM4617901 (marmoset iPS), GSM4616532 (human iPS), GSM4616535, GSM4616536 (pigiPS) from study GSE152493,<sup>95</sup> GSM1287734, GSM1287735, GSM1287745, GSM1287746 (mouse ESC), GSM1287736, GSM1287747, GSM1287748 (mouse iPS), GSM1287749, GSM1287750 (mouse fibroblasts, MEF) from GSE53212,<sup>96</sup> and GSM4303994, GSM4303995 (human naïve ES), GSM4304018, GSM4304019 (human primed ES) from GSE144994.<sup>97</sup> Note, that each analysis only induced genes that were annotated in all of the respective species.

### Evolutionary selection analysis

To explore evidence of positive selection in *R. ferrumequinum* for the 674 genes identified as part of the “leading” edge in the PCA analysis described above, we extracted all gene alignments that were available for these transcripts ( $n = 491$ ) and had previously been annotated,<sup>25</sup> in addition to annotating 169 alignments that had been made available as part of BAT1K but were currently unannotated. These alignments contained a maximum of 48 species from all eutherian mammalian superorders, with the species tree published by Jebb et al.<sup>25</sup> used for all selection analyses. A total of 660 of these alignments contained representative genes for *R. ferrumequinum* and were analysed for positive selection using the branch-site models in the codeml package of the PAML suite software.<sup>108</sup> Positive selection was inferred using likelihood-derived dN/dS ( $\omega$ ) values under both a null (foreground and background  $\omega$  constrained to be less than 1) and alternative (foreground  $\omega$  can vary) model. The *R. ferrumequinum* lineage was designated as foreground branch to detect unique instances of taxon-specific positive selection. A likelihood ratio test (LRT,  $2 \cdot \ln L_{\text{alt}} - \ln L_{\text{null}}$ ) was used to compare the fit of both models, with a p-value calculated assuming chi-squared distributed LRTs. P-values were corrected for multiple testing using the Benjamin-Hochberg False Discovery Rate (FDR) method via ‘*padjust*’ implemented in R. Any significant gene showing a p-value greater than 0.05 with  $\omega > 1$  was explored further. Significant sites showing positive selection were identified using Bayes Empirical Bayes (BEB) scores with a probability  $> 0.95$ . All significant genes were subject to a visual inspection of the alignment, to rule out potential false positive results having occurred due to misaligned sequences. In addition to *R. ferrumequinum*, the *M. myotis* ( $n=637$  representative genes), *Homo sapiens* ( $n=652$ ), *Mus musculus* ( $n=628$ ), *Canis lupus* ( $n=593$ ) and *Felis catus* ( $n=603$ ) lineages were also independently designated as foreground branches for all genes containing a representative sequence shared with *R. ferrumequinum*. This served as a means of determining whether positive selection identified in *R. ferrumequinum* was truly unique to the species lineage or a consequence of bat-specific, Laurasiatherian-specific, or eutherian mammal-specific instances of sequence evolution.

### Gene ontology and KEGG pathway analyses

Gene ontology and KEGG pathways that are enriched within a group of genes were identified with the Enrichr tool ([maayanlab.cloud/Enrichr/](https://maayanlab.cloud/Enrichr/)).<sup>110</sup> The odd ratios were then plotted with ggplot2 ([cran.r-project.org/web/packages/ggplot2/index.html](https://cran.r-project.org/web/packages/ggplot2/index.html))<sup>107</sup> with the odds

ratio displayed on the x-axis, the dot size reflecting the gene count (number of genes present in the top 5% of PC1 contributing genes) and the dot color reflecting the p-value.

### Protein interaction network analysis

The genes of the Corona virus disease related KEGG pathway were retrieved from the PathCards database (<https://pathcards.genecards.org>). The differential expression analysis was performed between RFe bat (this study) and mouse iPSC cells (GSM1287736, GSM1287747 and GSM1287748 from Study GSE53212<sup>95</sup> using DESeq2.<sup>105</sup> The Corona virus disease-related genes were then illustrated with Cytoscape (Version 3.8.2)<sup>111</sup> using the STRING protein query with a 0.8 confidence score cutoff. The nodes were colored based on the  $\log_2$  Fold-change with a negative (blue) fold change indicating down-regulation and a positive (red) fold change indicating upregulation in bat pluripotent stem cells. Bold borders indicate proteins that were present in the top 5% of PC1 in the PCA analysis described above.

### Electron microscopy

RFe iPSCs were grown in chambered Permax slides (LabTek, 70390) on irradiated mouse embryonic fibroblasts as described above for 5 days and then further processed by the Biorepository and Pathology core at the Icahn School of Medicine at Mount Sinai. Briefly, the RFe iPSCs were rinsed once with DPBS and fixed overnight with 2% paraformaldehyde and 2% glutaraldehyde in 0.01 M sodium cacodylate buffer at 4°C. Sections were rinsed in 0.1 M sodium cacodylate buffer, followed by a quick rinse with ddH<sub>2</sub>O. RFe iPSCs were post fixed with 1% aqueous osmium tetroxide for 1 hour, followed with an En bloc stain of 2% aqueous uranyl acetate for 1 hour. Sections were washed again in ddH<sub>2</sub>O, dehydrated through graduated ethanol (25-100%), infiltrated through an ascending ethanol/epoxy resin mixture (Embed 812, Electron Microscopy Sciences), and then covered with pure resin overnight. Chambers were separated from the slides, and a modified #3 BEEM embedding capsule (Electron Microscopy Sciences) was placed over defined areas containing cells. Capsules were filled with pure resin and placed in vacuum oven to polymerize at 60°C for 72 hours. Immediately after polymerization, the capsules were snapped from the substrate to dislodge the cells from the slide. Semi-thin sections (0.5 - 1  $\mu$ m) were obtained using a Leica UC7 ultramicrotome (Leica, Buffalo Grove, IL), counterstained with 1% Toluidine Blue, cover slipped and viewed under a light microscope to identify successful dislodging of cells. Ultra-thin sections (85 nm) were collected on 300 hexagonal mesh copper grids (Electron Microscopy Sciences) using a Coat-Quick adhesive pen (EMS). Sections were counter-stained with uranyl acetate and lead citrate and imaged with a Hitachi 7700 Electron Microscope (Hitachi High-Technologies) using an advantage CCD camera (Advanced Microscopy Techniques). Images were adjusted for brightness, contrast, and size using Adobe Photoshop CS4 11.0.1.

### Image-based flow cytometry (ImageStream)

RFe iPSCs were seeded onto 6-well plates and separated from irradiated MEFs via two-stage trypsinization after four days. Wells were dosed and incubated with 0.25ml prewarmed (37°C) trypsin which was removed and discarded at 4 minutes. An additional 0.25ml trypsin was added and the plate was again incubated. After eight minutes cells were removed and pelleted via centrifugation. The cells were washed twice in PBS containing 0.5% BSA (Sigma), fixed and permeabilized with Cytotfix/Cytoperm (Invitrogen, C10337). The Primary antibody was added at a dilution of 1:200 in wash buffer incubated overnight at 4°C. The RFe cells were washed twice with 0.5% BSA/PBS, resuspended in wash buffer containing the secondary goat anti-mouse AF568 antibody (Life Technologies, A-11029) in a 1:200 dilution and incubated for 1 hour at 4°C. The RFe cells were washed as before resuspended in 0.5% BSA/PBS containing two drops/ml DyeCycle Violet to stain the nuclei. Imaging was conducted with the ImageStream MkII, at 60x magnification with the extended depth of field mode for probe resolution. Images were acquired using the INSPIRE 2.0 software at the lowest flow speed. Fluorophores were excited by the 405 nm and 568 nm lasers at 60 mW and 100 mW, respectively. RFe cells in focus were gated via histogram of brightfield gradient R.M.S. values and an aspect ratio vs. area plot was used to select the population of single cells. 5000 individual images of focused single cells were taken. Gating was refined further post-acquisition via the IDEAS 6.2 software suite by the same methods and plots, yielding n=1846 (BiPS). This software was used also for image processing, in which a set of custom masks defined by logical operators were used to denote vesicles and sensitively assess probes. For vesicles, it was observed that they may be selected from other cell component by contrast (bright and dark) and also by aspect ratio, and therefore are defined here by "Dilate(Range(Dilate(Range(System(Peak. (Threshold(M01, BF, 70), BF, Bright, 1), BF, 20), 0-5000, 0.4-1), 1), 0-5000, 0.4-1), 1) Or Range (AdaptiveErode(Level Set(M01, BF, Dim, 5), BF, 75), 0-5000, 0.5-1)." BF and BF2 represent each brightfield image taken of a single cell from each of the two cameras, M01 and M09 represent the corresponding channel masks for each channel and the remaining terms represent mask modifiers and their associated values in the IDEAS software. For resolving immunofluorescence, "Peak(System(M05, Ch05, 3), Ch05, Bright, 1)" where Ch05 represents the staining of interest and M05 represents the corresponding channel mask. Modification was necessary to sensitively include all representative fluorescence, and to distinguish individual foci. The nuclear mask corresponding to DyeCycle Violet staining was defined "Object(M07, Ch07, Tight)" and the cytoplasm was defined through subtraction of the nuclear and vesicle masks from the cell mask through the logical operator available in the software ("Not"). Vesicle-nucleus overlap was determined in favor of vesicles by excluding them from the nuclear mask ("Not"). Probe localization was then defined according to these entities using the respective definitions and the operator "And." Statistics for foci were generated using the Spot Count feature with a connectedness of 4. Prism 9 was used for graphs and statistics.

### Retrovirus assay

2 ml of tissue culture medium were collected, and retroviral particle concentrations were determined using the QuickTiter Retrovirus Quantitation Kit (Cell Biolabs, VPK-120) according to the manufacturer's instructions.

### Reverse transcriptase assay

Reverse transcriptase enzyme levels were determined with the colorimetric reverse transcriptase kit (Roche) per the manufacturer protocol. Cells lines represented were lysed in RIPA buffer, frozen at  $-80^{\circ}\text{C}$ , thawed on ice, collected, and resuspended in the kit lysis buffer (10  $\mu\text{L}$  pellet in 40  $\mu\text{L}$  lysis buffer per colorimetric well). Incubation duration (15 h at  $37^{\circ}\text{C}$ ) was selected for maximal sensitivity to the limit of the kit (1–5 pg RT). Absorbance at 405 nm was measured by microtiter ELISA plate reader. Sample absorbance measurements were fitted to a linear regression of the measured HIV-1 RT standards ( $Y=2.549X$ ) to obtain RT concentrations in units of ng/well.

### Plaque assay

Supernatants were centrifuged at 10000 rpm for 5 min to remove cellular debris, and the cleared lysates transferred to new tubes. Lysates were then diluted in 10-fold dilutions 6 times. Quantification of infectious titer was then performed by plaque assays in comparison to SARS-CoV-2 infection as positive control. Briefly, Vero-E6 cells were plated as confluent monolayers in 12 well dishes. Media was removed, and wells washed in 1 ml of PBS. 200  $\mu\text{L}$  of diluted lysates were then added per well and allowed to incubate for 1 hour at  $37^{\circ}\text{C}$ . After viral adsorption, lysates were removed from the well and cells were overlaid with Minimum Essential Media supplemented with 2% FBS, 4 mM L-glutamine, 0.2% BSA, 10 mM HEPES and 0.12%  $\text{NaHCO}_3$  and 0.7% agar. 72h post infection, agar plugs were fixed in 10% formalin for 24h before being removed. Plaques were visualized by staining with TrueBlue substrate (KPL-Seracare) and viral titers calculated and expressed as PFU/ml.

### Metapneumovirus (MPV) infection of BiPS and mES cells

50,000 mouse ES cells (R1) or RFe iPSCs were plated per well of a 12-well plate on irradiated CF1 mouse embryonic fibroblasts using mouse and bat culture medium respectively. After 24 hours, culture medium containing human Metapneumovirus with GFP (MPV-GFP) (ViraTree, M121) with a final multiplicity of infection (MOI) of 3. Medium was changed daily, and samples were dissociated at 3 and 5 dpi using 0.05% Trypsin-EDTA and the infection rate was determined by fluorescence activated cell sorting (FACS).

### Iso-Seq library preparation and sequencing

RFe iPSCs and BEFs at passage 27 and passage 2–4 were lysed in 400  $\mu\text{L}$  Trizol reagent (Life Technologies, 15596-018) and total RNA was extracted using the AllPrep DNA/RNA Mini Kit (Qiagen, #80204) including a DNase digest to remove any potential contamination from carryover of genomic DNA using RNase-free DNase (Qiagen, 79254) according to the manufacturer's instructions. The extracted RNA was then purified using 1.8X RNAClean XP beads (Beckman Coulter) to remove any molecular impurities. Iso-Seq SMRTbell libraries were prepared as recommended by the manufacturer (Pacific Biosciences). Briefly, 300 nanograms of total RNA ( $\text{RIN} > 8$ ) from each sample was used as input for cDNA synthesis using the NEBNext Single Cell/Low Input cDNA Synthesis & Amplification Module (NEB, E6421L), which employs a modified oligodT primer and template switching technology to reverse-transcribe full-length polyadenylated transcripts. Following double-stranded cDNA amplification and purification, the full-length cDNA was used as input into SMRTbell library preparation, using SMRTbell Express Template Preparation Kit v2.0. Briefly, a minimum of 100 ng of cDNA from each sample were treated with a DNA Damage Repair enzyme mix to repair nicked DNA, followed by an End Repair and A-tailing reaction to repair blunt ends and polyadenylate each template. Next, overhang SMRTbell adapters were ligated onto each template and purified using 0.6X AMPure PB beads to remove small fragments and excess reagents (Pacific Biosciences). The completed SMRTbell libraries were further treated with the SMRTbell Enzyme Clean Up Kit to remove unligated templates. The final libraries were then annealed to sequencing primer v4 and bound to sequencing polymerase 2.0 before being sequenced on one SMRTcell 8M on the Sequel II system with a 24-hour movie each. After data collection, the raw sequencing subreads were imported to the SMRTLink analysis suite, version 10.1 for processing. Intramolecular error correcting was performed using the circular consensus sequencing (CCS) algorithm to produce highly accurate ( $>Q10$ ) CCS reads, each requiring a minimum of 3 polymerase passes. The polished CCS reads were then passed to the *lima* tool to remove Iso-Seq and template-switching oligo sequences and orient the isoforms into the correct 5' to 3' direction. The *refine* tool was then used to remove polyA tails and concatemers from the full-length reads to generate final full-length, non-concatamer (FLNC) isoforms. The FLNC isoforms were then clustered together using the *cluster* tool to generate final, polished consensus isoforms per sample.

### Identification and illustration of viral sequences in the bat pluripotent stem cell transcriptome

The existence of viruses in the *Rhinolophus ferrumequinum* transcriptome was explored by analysing the RNA-seq and Iso-seq data based on a metagenomic approach using Kraken2 v2.1.2<sup>112</sup> First, the adaptors in the RNA-seq data were removed with TrimGalore v0.6.7<sup>114</sup> and all replicates for corresponding datasets were joined in one file. The reference library "RefSeq complete viral genomes / proteins" was downloaded and a custom database was built to identify matches within the processed RNA-seq or Iso-seq. To eliminate false positive hits that could be due to matches with any cellular transcript such as oncogenes that are carried by some viruses, a second analysis was performed after eliminating all reads from the RNA-seq and Iso-seq datasets that matched any annotated

*Rhinolophus ferrumequinum* transcript. To do this, the Iso-Seq FLNC isoforms or RNA-seq trimmed fastq sequences were first mapped to the “*Rhinolophus ferrumequinum* genomic rna exons RefSeq” file “GCF\_004115265.1\_mRhiFer1\_v1.p\_ma\_from\_genomic.fna” using gmap/gsnap.<sup>113</sup> The sequences with no mappings were then used to identify viral sequences using Kraken2 as before.

In a first approximation, we mapped the sequencing reads against a virus database, using a metagenomic classification tool (Kraken2). The results revealed a taxonomically highly diverse “zoo” of assigned viruses belonging to several major viral families. We also classified viral sequences using RNA-seq data from BEFs (Table S5B) and from human ES cells (Table S5C) notably yielding some viral sequences albeit to a lesser degree (Figure S11A). This observation in BEFs was surprising as post-implantation tissues typically do not exhibit endogenous viral activity,<sup>50</sup> underscoring the notion that bat cells harbor pro-viral environments. Further, the results support our hypothesis that the epigenetic reprogramming of bat fibroblasts reactivates a considerable number of additional dormant viral sequences.

Further, we investigated potential confounding effects that might impact interpretation of the metagenomic data. Three potential sources for distortion are (i) statistical stringency, (ii) cellular genes containing viral-like sequences (e.g., oncogenes), and (iii) potential *xeno* sequence pollution originating from the feeder cells. To address the first point, we utilized progressively higher statistical stringency, yielding an expected decrease in matches in our *R. ferrumequinum* RNA-seq data. However, even with the most stringent parameters tested, there remained a sizable number of hits. To exclude potential cellular genes misinterpreted by the classification algorithm as viruses, we depleted the RNA-seq and Iso-seq from all sequences that match exons, which only marginally affected the number of hits. When the Kraken2 database was expanded to include bacteria, archaea, and the whole human genome, the yield was only 0.65 percent, compared to 2.53 percent when the viral database was probed (Figure S11B). Finally, we checked if some of the classified sequences were of murine origin and found that this was the case for several retroviruses, and for example, the sequences classified as Diatom colony associated ssRNA virus 1. The latter matched a genomic region on mouse chromosome chr9: 65,969,137-65,969,198 (GRCmm39/mm39).

In addition to Kraken2, we also processed sequences through the Microsoft Premonition metagenomics pipeline (<http://microsoft.com/premonition>), which uses an alignment-based approach (cf Kraken2’s k-mer based method) to identify matches, in addition to employing a larger reference database, factors which can increase sensitivity/reduce false negatives. The Premonition pipeline also uses a statistical model to probabilistically assign reads to taxonomic levels, favoring matches with better coverage of the reference genome, increasing specificity/reducing false positives.

### Mapping of RNA-seq reads to bat genomes and quantifying expression of ERVs

To trim adapters and generate quality metrics of the fastq files, we used Trimmalore v.0.6.6 (<https://github.com/FelixKrueger/Trimmalore>), a wrapper for Cutadapt (<https://github.com/marcelm/cutadapt>) and FastQC (<https://www.bioinformatics.babraham.ac.uk/projects/fastqc/>). Then, reads were mapped to the genome of *R. ferrumequinum* and *M. myotis* (Bat1K assembly HLrhiFer5) using HISAT2 v.2.2<sup>101</sup> suppressing unpaired alignments for paired reads (–no-mixed), suppressing discordant alignments for paired reads (–no-discordant), and setting a function for the maximum number of ambiguous characters per read (–n-ceil L,0,0.05). Output files were then filtered to remove any unmapped reads (–F 4), sorted and indexed using samtools.<sup>102</sup> Aligned reads were then assembled into transcripts using stringTie v2.2.1<sup>115</sup> in stranded mode (–rf). To generate a Ballgown readable expression output with normalized expression units of fragments per kilobase of transcript per million mapped fragments (FPKMs), we also used as input in stringTie the Bat1K annotation of known endogenous retroviruses (ERVs) for *R. ferrumequinum* and *M. myotis* (<https://genome.senckenberg.de/>).<sup>25</sup> Output counts were post-process and plotted with a custom R script.

### De novo assembly of potential virus-derived RNA-seq

The trimmed reads that were identified by Kraken2 v2.1.2 to map to viral sequences with a confidence score of 0 as described above were first grouped together based on their taxonomic ID assigned by Kraken and then classified as either mammalian or non-mammalian using the VIRION database.<sup>123</sup> The data were converted to FASTA format using the Seqtk v1.3 program and the reads were assembled using the Trinity v2.12 software.<sup>116</sup> To check and gather successful assemblies that had produced at least one contig, a custom BASH script was applied for both groups of mammalian and non-mammalian viruses.

### Mapping transcripts to viral and mammalian databases

To determine if the assembled transcripts represented an expressed viral sequence, all transcripts were mapped to a database of viral genomes using BLAST.<sup>117,118</sup> The viral database consisted of genomes whose host species contained either ‘human’ or ‘vertebrate’ as specified in the NCBI database. Initially this list contained over 17,000 genomes. However, this was reduced to 3,922 genomes by taking only unique virus/strain names. An additional non-mammalian virus database was generated by combining all genomic sequences of viruses identified by Kraken2 and classified as non-mammalian via VIRION. Transcripts were also mapped to a combined database of RFe bat, human and mouse genomes to both confirm their presence in the bat and to exclude the possibility of false positives through contamination. For each of these transcripts, expected values for both bat and viral genome BLAST results were combined into a single metric via the following formula:  $\text{Log}(\text{bat-expected value}+1 \times \text{virus-expected value}+1)$ . A threshold of less than 0.3, representing a combined e-value of less than  $1e^{-50}$  for both viral and bat hits, was used to rule out potential false positives. In addition, we used SQUID (<http://eddylab.org/software.html>) to shuffle the 63 (bottom-up) and 82 (top-down)

sequences while preserving the dinucleotide distribution (parameter -d) to obtain a conservative threshold to distinguish bona fide viral homology from matches by random chance. Shuffled sequences were mapped to both the bat genome and viral genome databases, with the same BLAST threshold applied. All transcripts passing this threshold were extended by 5000 bp flanks within the bat genome and these regions were subsequently mapped to the viral database to confirm their presence in a viral genome.

### **QUANTIFICATION AND STATISTICAL ANALYSIS**

Statistical details of experiments are described in the figures, figure legends, and methods. In general, statistical analyses are presented as mean  $\pm$  SEM or SDEV. Comparisons between two groups were determined by Student's t-test. Multiple comparisons were determined by one- or two-way ANOVA followed by post-hoc testing as indicated in the figure legends. Significance criterion was set at a P-value of  $\geq 0.05$ .

# Supplemental figures

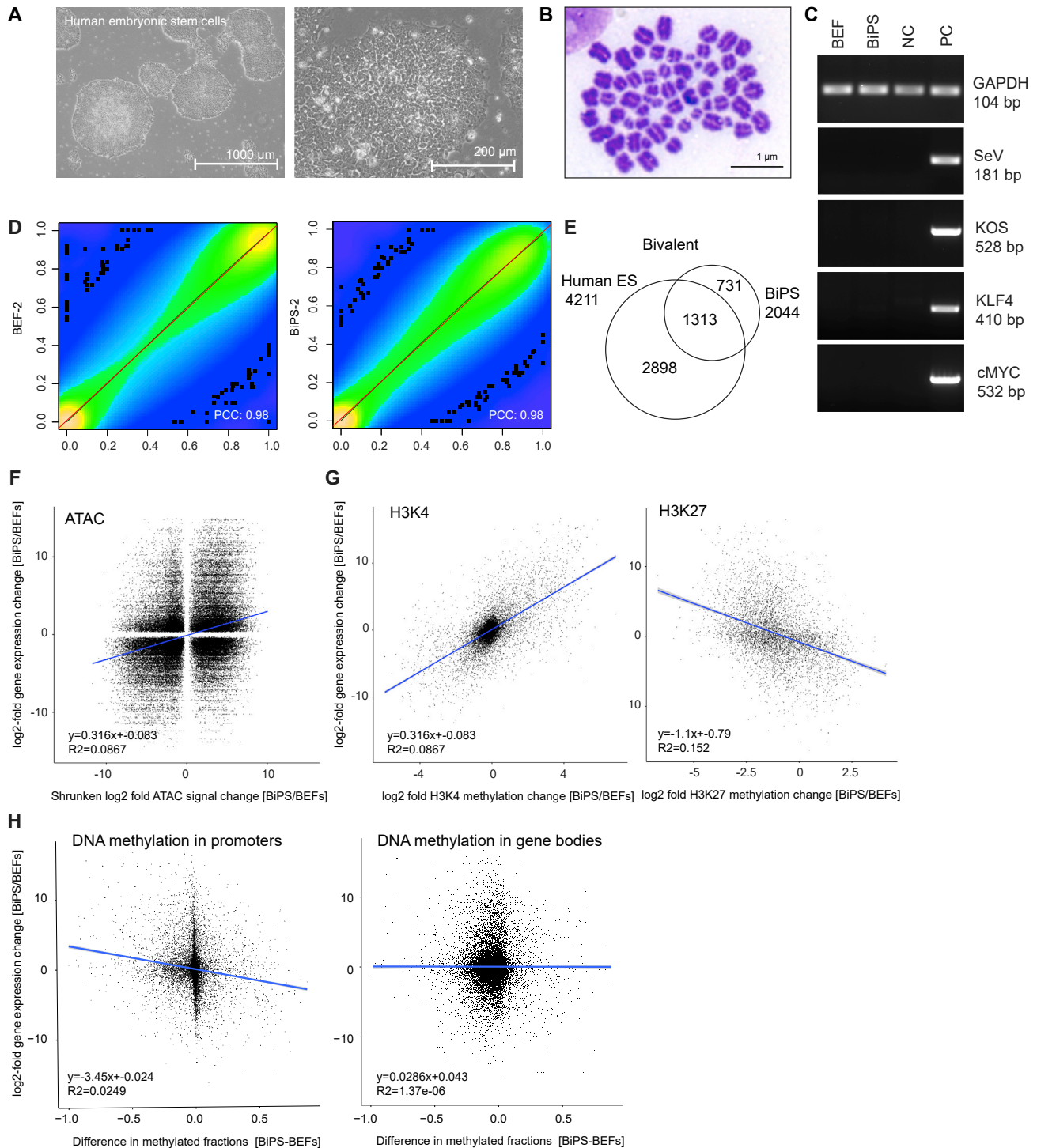


**Figure S1. Characteristics of pluripotent stem cells generated from *Rhinolophus ferrumequinum* fibroblasts, related to Figure 1 and Table S1**

(A) Microscopic images of human embryonic stem cells (H9) and bat pluripotent stem cells at different magnifications.

(B) Karyotype analysis of BiPS cells at passage 17. Shown is a representative image after Giemsa staining of metaphase spreads with 58 chromosomes.

(legend continued on next page)

---

(C) PCR verification of reprogramming-associated virus clearing. Bat iPS cells (BiPS) at passage 92 were tested for Sendai virus clearance in comparison to the embryonic fibroblasts used as starting material (BEF), adult fibroblasts as negative control (NC), and freshly transduced cells at passage 3 as a positive control (PC). bp, base pairs; SeV, Sendai virus; KOS, KLF4-OCT4-SOX2.

(D) Correlation scatter plot of methylation level at common CpG sites in BEF or BiPS cells. Shown is the representative result of one of two replicates per cell type. BEF, bat embryonic fibroblast cells; BiPS, bat pluripotent stem cells; PCC, Pearson correlation coefficient.

(E) Venn diagram illustrating the overlap of bivalent genes in bat iPS cells and human ES cells.

(F) Correlation plot of shrunken  $\log_2$ -fold changes in ATAC-seq signal with  $\log_2$ -fold expression changes. Shown are the average values with  $p < 0.05$  of two replicates per cell type.

(G) Correlation of  $\log_2$ -fold changes in H3K4 trimethylation (H3K4me3, left) or H3K27 trimethylation (H3K27me3, right) with  $\log_2$ -fold changes in gene expression. Shown are the results of one sample for each chromatin mark.

(H) Correlation of  $\log_2$ -fold gene expression changes with the difference in the methylated fraction of promoters (left) or gene bodies (right) fractions. Shown are the average expression changes from three replicates per condition and methylated fractions from two replicates.

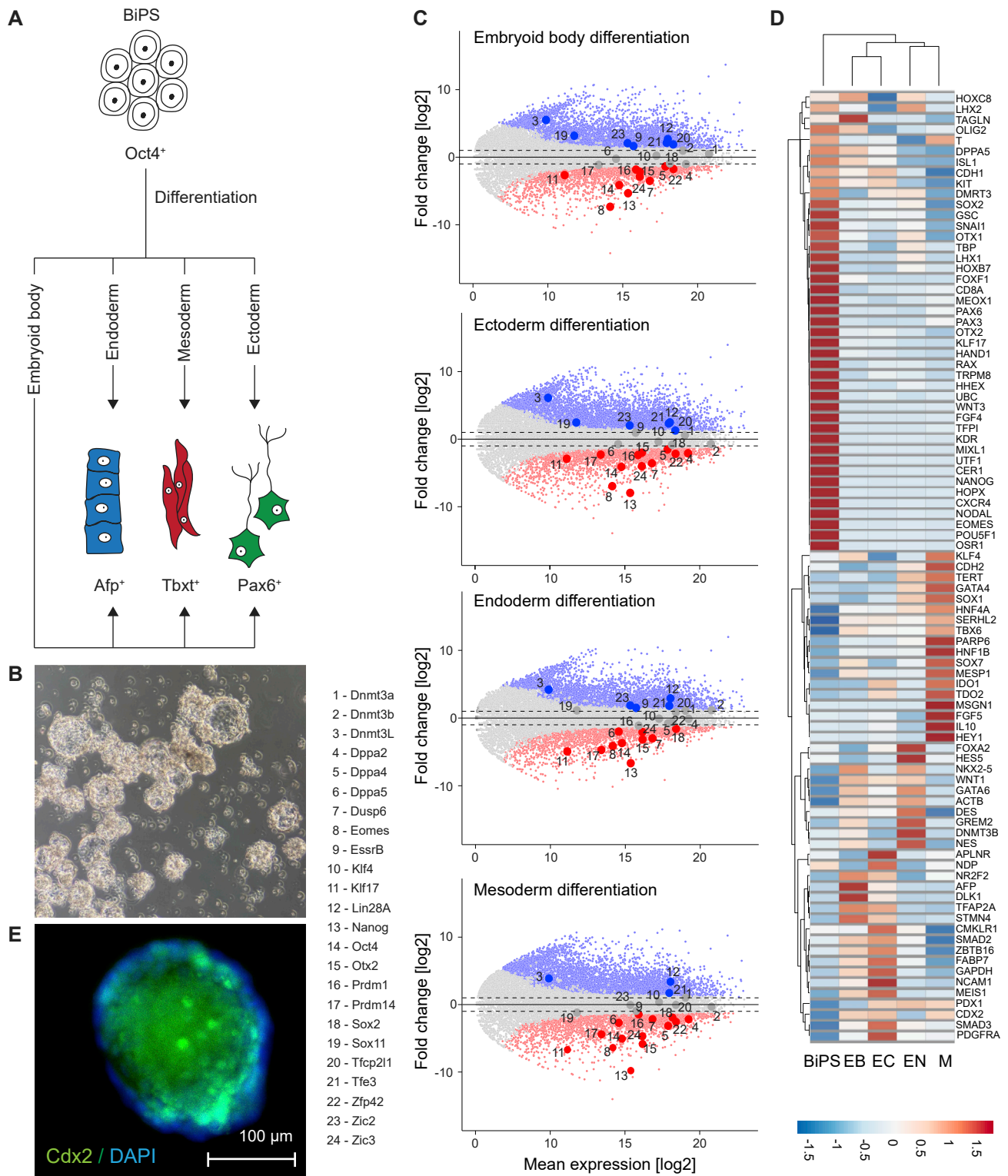


**Figure S2. Differentiation potential of bat pluripotent stem cells, related to Figure 2 and Table S2**

(A) Schematic of differentiation strategies.

(B) Phase contrast image of BiPS2-derived embryoid bodies after 7 days of differentiation.

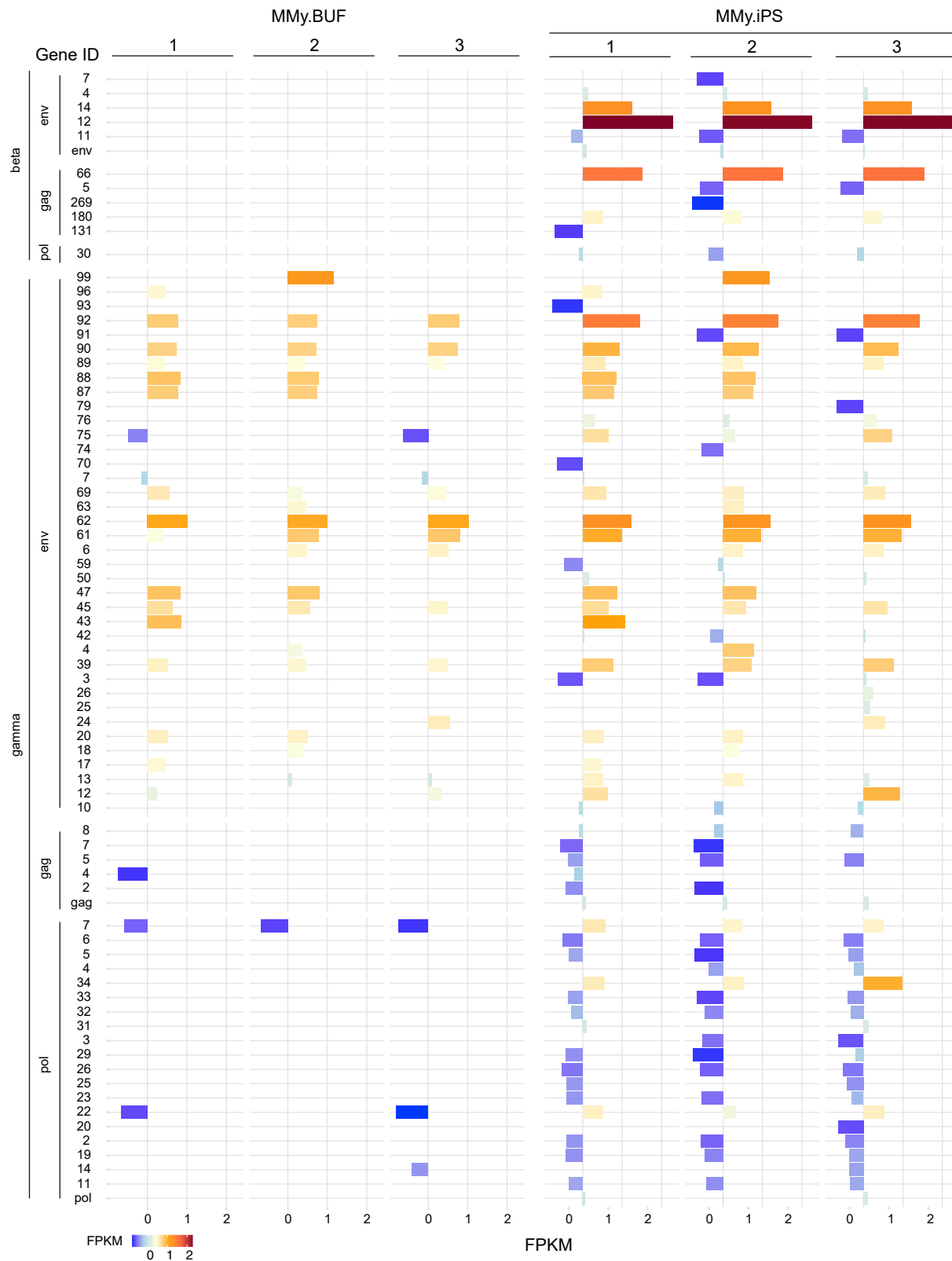
(legend continued on next page)

---

(C) MA plots depicting the  $\log_2$  mean expression and  $\log_2$ -fold expression changes of all genes in bat induced pluripotent stem cells (BiPS) after exposure to the noted differentiation conditions illustrated in (A). Shown is the mean average of each gene from three replicates per differentiation condition ( $n = 3$ ). EB, Embryoid body differentiation; EC, human ectoderm differentiation conditions; EN, human endoderm differentiation conditions; M, human mesoderm differentiation conditions.

(D) Heatmap depicting expression changes of genes that are known as markers for human ectoderm, mesoderm, or endoderm during the differentiation of BiPS under the conditions described in (A). Shown is the average expression of 3 replicates per condition.

(E) Representative microscopic image of a bat blastoid after immunostaining using a Cdx2-specific antibody.



(legend on next page)

---

**Figure S3. Reactivation of endogenized viral elements in *Myotis myotis* induced pluripotent stem cells, related to [Figure 6](#) and [Table S4](#)**  
Expression of indicated ERV elements in *Myotis myotis* bat uropatagium fibroblasts (MMy.BUF) and induced pluripotent stem cells (MMy.iPS) as determined by extracting the overlap between RNA-seq reads mapped to the *Myotis myotis* genome and known mapped ERV elements. Shown are the elements with the most evident differences from three replicates.

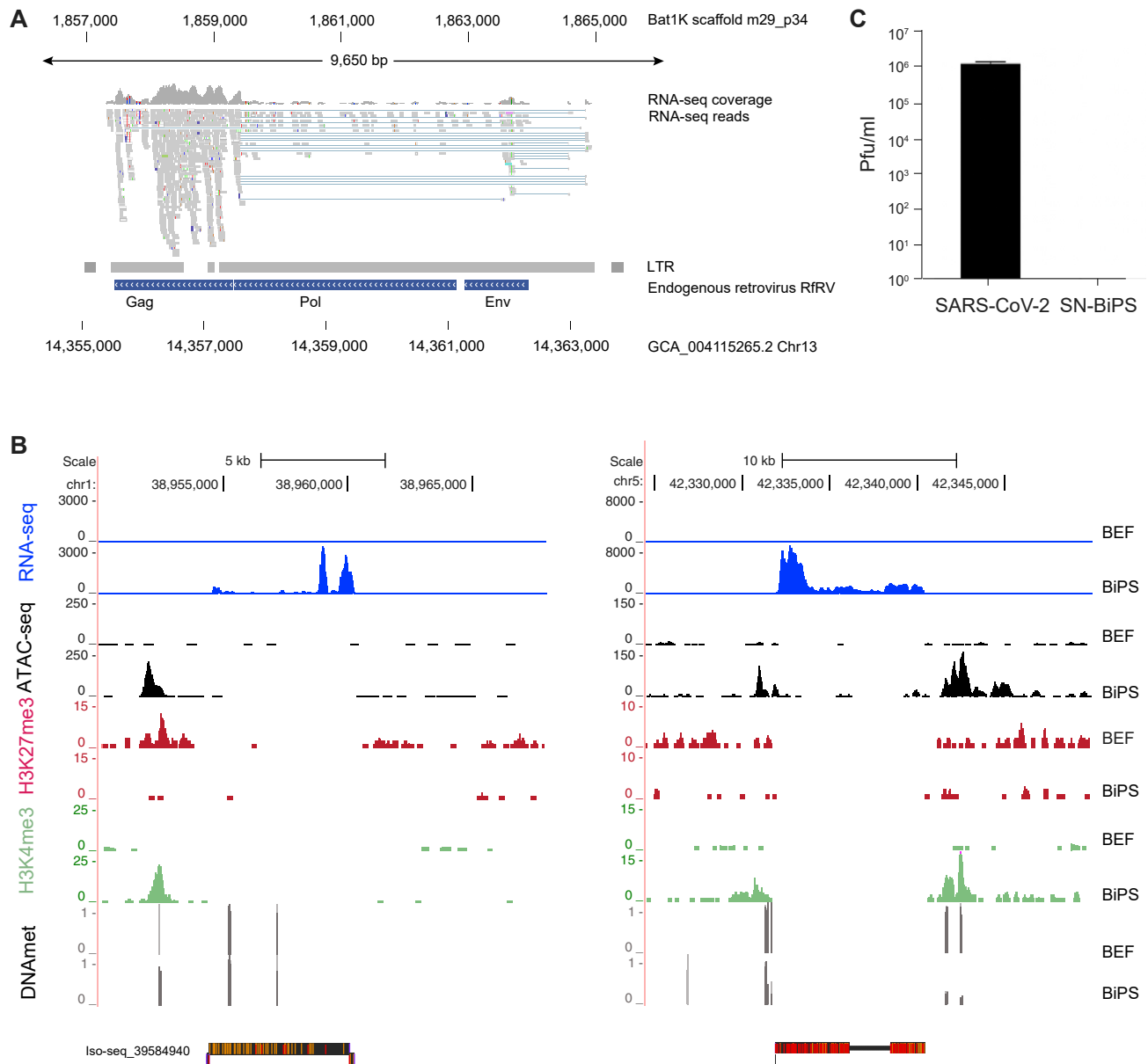


**Figure S4. Viral activity in BiPS cells, related to Figure 6 and Table S4**

(A) RNA-seq tracks aligning with the genomic *R. ferrumequinum* region (Bat1K annotated scaffold, *top*, and GCA assembly, *bottom*) containing the previously identified endogenous retrovirus RfRV. LTR, long terminal repeat.

(B) Sequencing tracks showing expression, ATAC-seq signal, histone H3K27 trimethylation (H3K27me3), histone H3K4 trimethylation (H3K4me3) as well as DNA methylation (DNAmeth) status in the genomic region on chromosome 1 surrounding RFe-V-MD1 shown in Figure 6 (left) and a genomic region on chromosome 5 that contains a sequence highly similar to RFe-V-MD1 (right). Note that the 6088 bp-long Iso-seq fragment aligns with the (-) strand on chromosome 1 and the (+) strand on chromosome 5.

(C) Plaque assay with supernatant of *R. ferrumequinum* induced pluripotent stem cells compared to active SARS-CoV-2 viral particles in Vero cells. BEF, bat embryonic fibroblasts; BiPS, bat induced pluripotent stem cells; SN, supernatant.

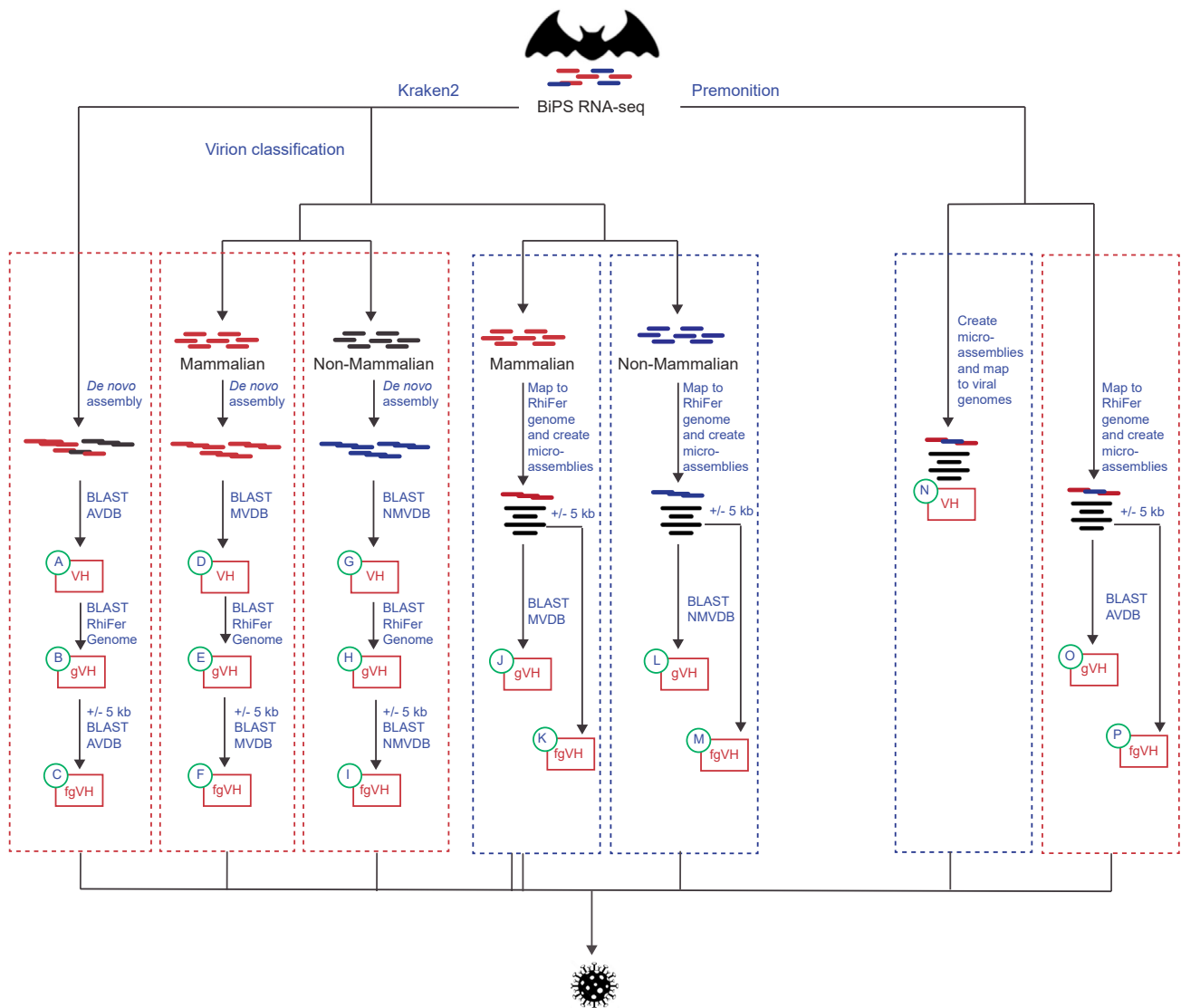


**Figure S5. Virome mining approaches, related to Figure 7 and Tables S5 and S6**

RNA-seq reads were first classified using Kraken2 (left). The classified reads were then either analyzed directly or separated by their homology to a mammalian or a non-mammalian virus using virion. In a 'bottom-up' approach (red boxes), the reads that were classified to belong to the same virus were assembled *de novo* and blasted against databases containing all viruses (AVDB), mammalian viruses (MVDB) or non-mammalian viruses (NMVDB). The identified sequences with viral hits were then further mapped to the *R. ferrumequinum* (RhiFer) genome (gVH) and in a final step, reads/assemblies that did map to the genome were extended by 5 kb on both sides and the sequences again blasted against the databases as before to extend the search for viral hits in flanking genomic regions (fgVH). In a parallel 'top-down' approach (blue boxes), the Kraken2 reads were mapped directly to the *R. ferrumequinum* genome, micro-assemblies were generated based on the mapped reads, and blasted directly against the different databases as before or first extended by 5 kb on both sides. In an orthogonal approach, the reads were similarly assigned to viruses using the Microsoft Premonition metagenomics pipeline (right). First all reads were classified as aligning to a virus or as being unaligned, micro-assemblies were generated and mapped to viral genomes (red box). Consensus sequences were extracted and blasted against the *R. ferrumequinum* genome, extended by 5 kb and blasted against a database containing all viruses as before. In another 'top-down' approach (blue box), the Premonition classified reads were mapped to the *R. ferrumequinum* genome first, and micro-assemblies generated that were blasted against the 'All virus' database either directly or after being extended by 5 kb on both sides. AVDB, all viruses database; MVDB, mammalian virus database; NMVDB, non-mammalian virus database; VH, viral hits; gVH, viral hits with homology to the bat genome; fgVH, viral hits using flanked genomic regions; RhiFer, *Rhinolophus ferrumequinum*; kb, kilobase pairs.

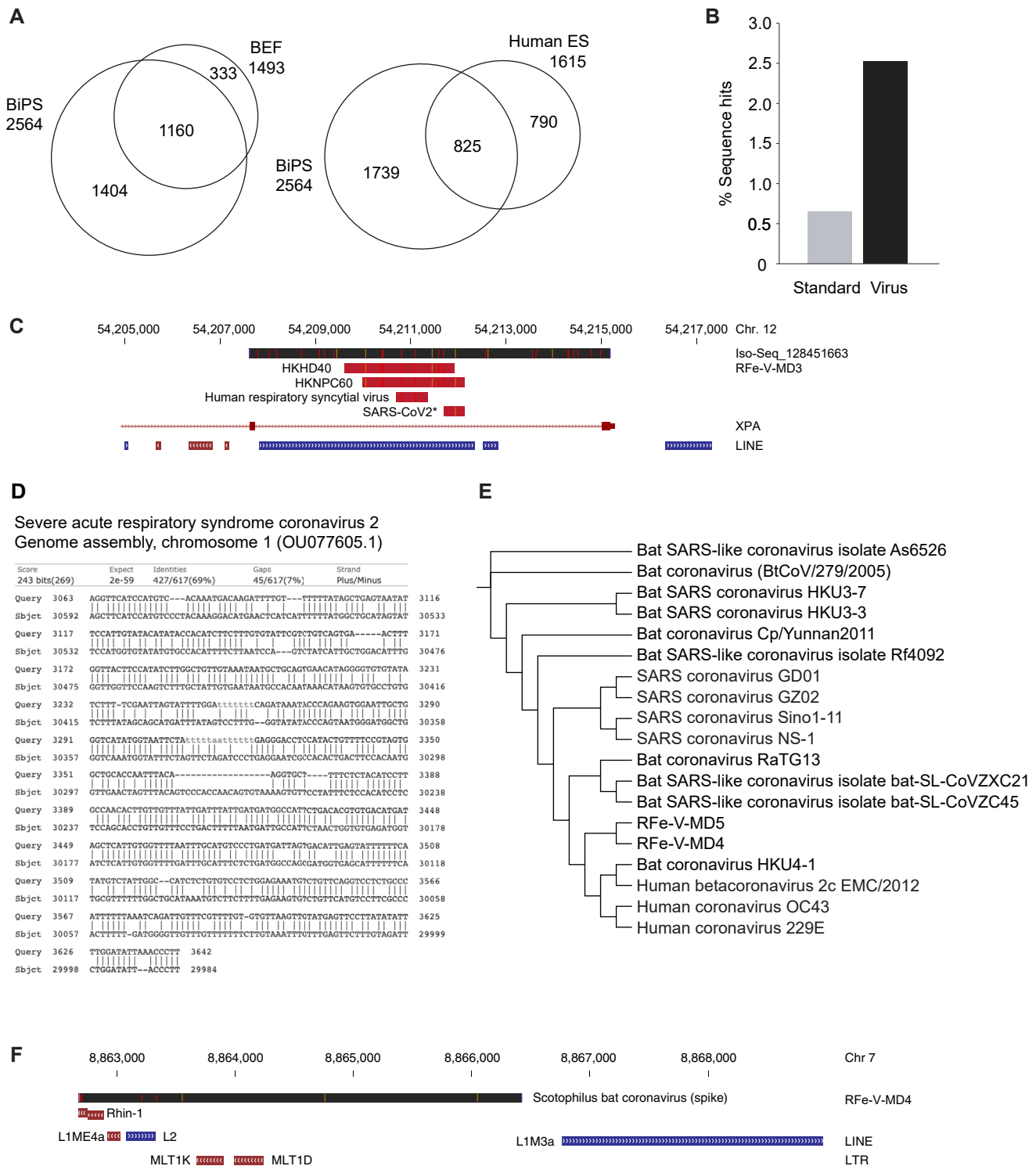


**Figure S6. Virome mining in *Rhinolophus ferrumequinum* BiPS cells, related to Figure 7 and Tables S6 and S7**

(A) Venn diagram showing the overlap of viral species as classified by Kraken2 in RNA-seq reads of BiPS and BEF cells (this study; *left*) and human ES cells (GSM4192140 and GSM4192141)<sup>98</sup> and *R. ferrumequinum* BiPS cells (*right*).

(B) Comparison of sequence hits using the Standard or a virus-specific database as reference in Kraken2 analysis with BiPS RNA-seq reads.

- 
- (C) Illustration of a short viral integration with homology to two *human herpesvirus 4* isolates (*HKD40* and *HKNPC60*), *human respiratory syncytial virus* (Kilifi isolate), and a ~500 bp fragment that was identified at the end of a *SARS-CoV2* isolate from an infected patient (NCBI ref. sequence OU077605.1). Shown is the alignment of the 7955 bp-long fragment to the *R. ferrumequinum* genomic sequence.
- (D) Sequence alignment of the Iso-seq read from BiPS (RFe-V-MD3) and the ~500 bp SARS-CoV2 fragment described in (C).
- (E) Phylogenetic relationship of the identified sequences RFe-V-MD4 and RFe-V-MD5 to a selection of corona viruses.
- (F) Genome track of the 6404 bp-long sequence (RFe-V-MD4) with homology to the *Scotophilus bat coronavirus 512* containing the spike coding region.

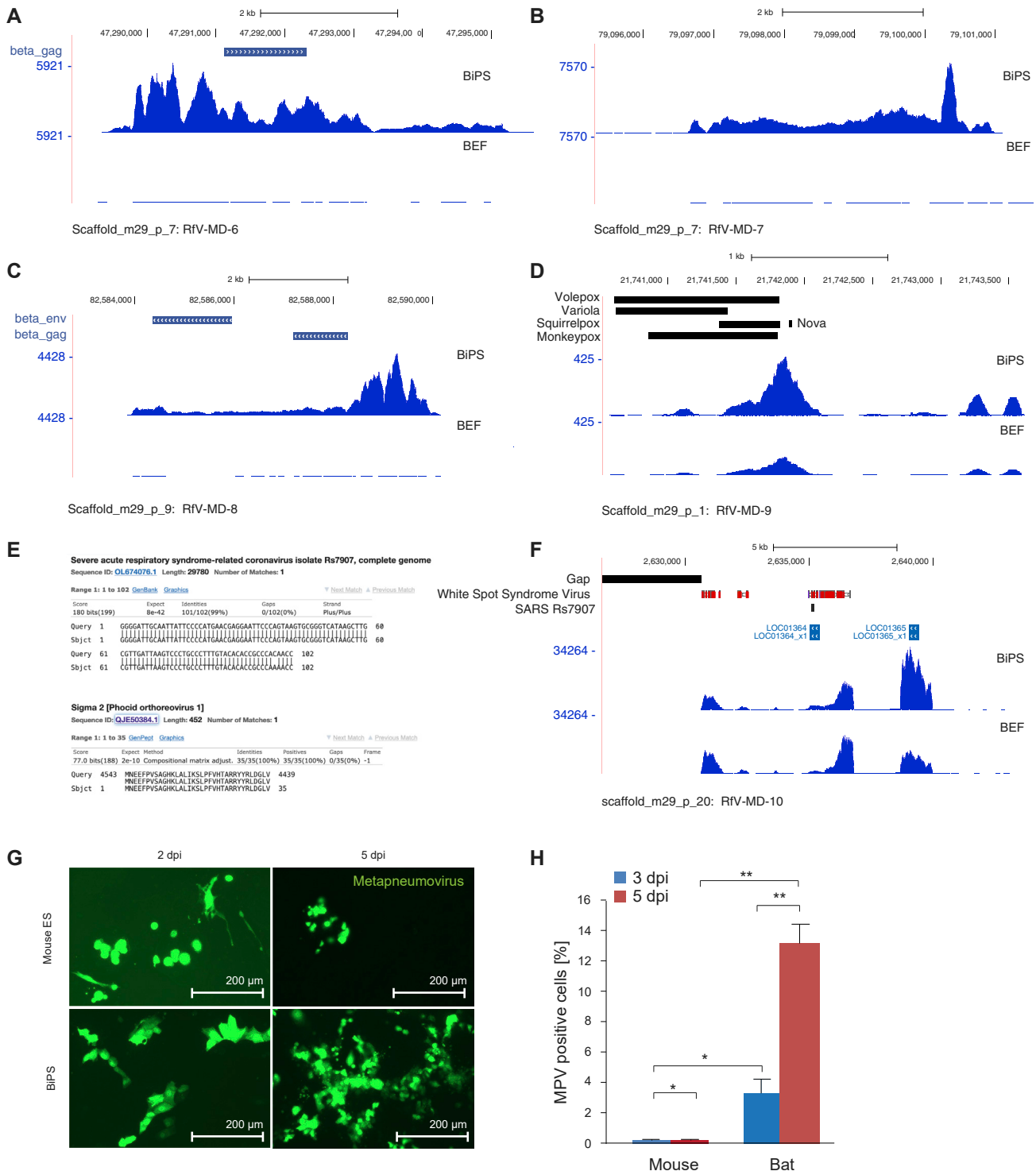


**Figure S7. Virome mining in *Rhinolophus ferrumequinum* BiPS cells, related to Figure 7 and Tables S6 and S7**

Chromosomal regions within indicated *R. ferrumequinum* scaffolds detected to contain homologies to the (A) *Mason-Pfizer monkey virus*, the (B) *Jaagsiekte sheep retrovirus*, or the (C) Simian endogenous retrovirus. Shown is the surrounding region covered by mapped RNA-seq reads that show further homologies to known viruses on DNA and protein levels as outlined in Table S7.

(D) Chromosomal region in the vicinity of DNA sequences with homology to several DNA viruses covered by RNA-seq reads that show homologies to *cowpox* and *monkeypox virus* proteins after translation using BLASTx.

(legend continued on next page)

---

(E) Short homology of expressed sequence reads with the *severe acute respiratory syndrome-related coronavirus isolate Rs7907* on DNA level (top) which translates into an N-terminal fragment of a dsRNA-binding protein (bottom).

(F) The chromosomal region surrounding the fragment shown in (E) that is covered by mapped sequence reads with further homologies to the White spot syndrome virus.

(G) Microscopic images of R1 mouse embryonic stem (ES) cells and *R. ferrumequinum* induced pluripotent stem cells (BIPS) at 2- and 5-days post-infection (dpi) with GFP-labeled Metapneumovirus (MPV) particles.

(H) Quantification of experiment shown in (A) at 3- and 5-days post-infection (dpi) by FACS. Data are shown as mean +/- SD; \*p < 0.05, \*\*p < 0.001.